Quantum Jump Spectroscopy of a Single Electron in a New and Improved Apparatus

A thesis presented

by

Joshua Charles Dorr

to

The Department of Physics

in partial fulfillment of the requirements

for the degree of

Doctor of Philosophy

in the subject of

Physics

Harvard University

Cambridge, Massachusetts

September 2013

Thesis advisor

Gerald Gabrielse

Author

Joshua Charles Dorr

Quantum Jump Spectroscopy of a Single Electron in a New and Improved Apparatus

Abstract

The 2008 measurement of the electron magnetic moment is the most precisely measured property of an elementary particle, with an astonishing precision of 0.28 parts per trillion. It makes possible the most precise determination of the fine structure constant and the most precise test of quantum electrodynamics and the Standard Model of particle physics. This thesis describes the installation of a new apparatus designed to have improved stability, more optimal control over the radiation field and inhibited spontaneous emission, and narrower resonance lines.

A gaseous ^{3}He NMR probe was developed to shim the magnetic field. Quantum jump spectroscopy with a single trapped electron produced the narrower resonance lines needed for a higher precision measurement of the electron magnetic moment. Positrons have been accumulated in the new apparatus, as an important step toward a greatly improved lepton CPT test.

Contents

List of Figures

List of Tables

Acknowledgments

The electron g-2 experiment in its current iteration has a long history, and I am indebted to each of the hardworking scientists who contributed to the project before me, including Joseph Tan (thesis in 1992), Ching-hua Tseng (1995), Daphna Enzer (1996), Steve Peil (1999), Kamal Abdullah (postdoc), Brian D'Urso (2003), Brian Odom (2004), and David Hanneke (2008). Their ideas and techniques are evident throughout this work.

None of this work would have been possible without the support and encouragement of my adviser, Gerald Gabrielse, whose vision and stamina have advanced this project to where it is today. I would also like to thank the National Science Foundation for supporting this work.

Shannon Fogwell Hoogerheide and I worked closely to build up this new apparatus. As we smoothed out its kinks and worked through its many growing pains, Shannon's unflappable nature helped me weather many temporary setbacks. I would also like to thank her for welcoming me onto the experiment and answering my numerous questions as I came up to speed. Josh Goldman (whose planar Penning trap experiment merged into our apparatus) taught me much of what I know about the physics behind Penning traps, as well as many tricks in Mathematica. He and I spent several late nights in lab wiring up the apparatus, taking data, and generally being silly when common sense had left us due to tiredness. I am leaving the experiment under the capable watch of Elise Novistksi, whom I would like to thank for her support as I shifted from working on the experiment to writing my thesis. I am confident the experiment will flourish under her guidance.

I would also like to thank the remainder of the Gabrielse lab members: David

LeSage, Nicholas Guise, Phil Larochelle, Steve Kolthammer, Phil Richerme, Robert McConnell, Yulia Gurevich, Jack DiSciacca, Ben Spaun, Paul Hess, Rita Kalra, Mason Marshal, Kathryn Marable, Nathan Jones, Chris Panda, Eric Tardiff, Stephan Ettenauer, Ronald Alexander and Maryrose Barrios. Over the years, we have all had many useful and informative conversations (not always about science) and they have made the lab feel like a home.

I have been lucky to work directly with 5 undergraduate students—Max Swiatlowski, Tova Holmes, Carl Hoffman, Shayna Skal and Armin Pourshafeie—and one visiting student from Germany—David Lindenfels. Each one has added something unique to the experiment.

Jan Ragusa keeps the Gabrielse lab running smoothly and always knew which forms I needed to sign and when. Stan Cotreau taught me to machine metal, to torch braze, to weld, and many other invaluable fabrication techniques that were intrumental in building the apparatus in this thesis. I will miss walking into the machine shop ready to turn an idea into something real, but more so, I will miss the conversations we had there. Jim MacArthur continually impresses me with his skill. He taught me to solder surface mount electronics, consulted on several electronics projects and also helped me to identify many miscellaneous electronics that I found in dark corners in the lab. I would like to thank him for his sense of humor and for always making time for me, despite his intensely busy schedule.

I would like to thank my friends and family for all of their support and encouragment. Jason Dowd and the rest of members of team 266 made the difficult parts of graduate school more enjoyable by sharing in the experience. Dave Patterson kept me

off the streets in the last few weeks of working on my thesis. My mom, Laurie Dorr, always told me I could do anything I wanted and genuinely believed it, even when I was not sure myself. John DeBell has always been like a father to me, and he was partly responsible for starting me down the path of being a physicist by introducing me to the weird world of quantum mechanics. Elaine Auyoung is by far the best thing I discovered in graduate school, and I would like to thank her for her love and friendship.

Chapter 1

Motivations and Background

This thesis describes the preliminary measurements and quantum jump spectroscopy of a single electron suspended in a cylindrical Penning trap at 100 mK. These measurements have been made in a new, high stability apparatus, designed to improve the precision of the electron and positron magnetic moments. Though the precision of the electron magnetic moment is already staggering, several motivating factors drive us toward improving the measurement. These include a more precise determination of the fine structure constant, better tests of quantum electrodynamics (QED), tighter limits on electron substructure, and finally, with an improved positron magnetic moment measurement, a better test of CPT in a lepton system.

1.1 The Magnetic Moment

The electron is a simple spin 1/2 particle. Its magnetic moment $\vec{\mu}$, the subject of this thesis, is pointed along the direction of the spin,

$$\vec{\mu} = -\frac{g}{2}\frac{e\hbar}{2m}\frac{\vec{S}}{\hbar/2} = -\frac{g}{2}\mu_B\frac{\vec{S}}{\hbar/2} \tag{1.1}$$

where -e is the charge of the electron, m is its mass, $\hbar$ is the reduced Planck, $\vec{S}$ is the spin of the electron and g is the g-factor of the electron. The second equality further highlights the magnetic moment as a product of the dimensionless angular momentum ($\vec{S}/(\hbar/2)$), the natural magnetic moment scale (μ_B, the Bohr magneton), and the dimensionless constant that sets the strength of the magnetic moment (g/2) in Bohr magnetons.

Though equation 1.1 is specific to the electron, this form (the product of angular momentum, natural scale and dimensionless constant) applies to the magnetic moment for many systems, though the g-factor will be different for each situation. For a classical system with equal uniform charge to mass distribution, g = 1. For a Dirac point particle, g = 2. The interactions of the electron with the vacuum of free space cause this value to deviate slightly from 2 by about a part per thousand. Internal substructure can also have a significant effect on the g-factor; for example, for the proton, $g/2 \approx 2.793$ [1].

1.2 Measuring the g-factor

The g-factor of the electron is the most precisely measured property of a fundamental particle to date. Its most recent value of $g/2 = 1.001\ 159\ 652\ 180\ 73\ (28)$ [0.28ppt] comes from our 2008 measurement using a single electron trapped in a cylindrical Penning trap and cooled to its cyclotron ground state [2]. This remarkable precision was achieved by building on a long history of g-factor measurements.

A review of the early history of lepton g-factors can be found in [3]. Though the electron anomaly had been measured using atomic beam techniques [4], the first direct measurement of the electron g-factor came in 1954 at the University of Michigan [5] with a precision of $\approx 10^{-2}$ (still consistent with g=2 for a Dirac point particle). In 1958, the measurement technique was refined to measure the anomaly rather than g [6] to a precision of nearly a part per thousand in the anomaly (so $\approx$ a ppm in g). The first single electron [7] measurement came in 1979 [8] (with a positron comparison in 1981 [9]) and a series of refinements lead to the longstanding 1987 measurement of the electron and positron g-factor at the $\approx$ 4 ppt level [10]. This measurement was made in a hyperbolic Penning trap [11] at 4.2 K.

A series of measurements at Harvard [12, 2, 13] has improved the precision of the electron, but the positron value has yet to be improved upon since 1987, as the apparatus used for the Harvard measurements did not have the space needed to load positrons.

It has been said that one should "Never measure anything but frequency" [14]. At its core, the g-factor is a frequency measurement, or rather, a ratio of frequencies, which is even better. For an electron in free space, the g-factor can be represented by a ratio of the spin and cyclotron frequencies, as is shown in equation 1.2:

$$\nu_s = \frac{2\mu B}{h} = \frac{g}{2}\nu_c \rightarrow \frac{g}{2} = \frac{\nu_s}{\nu_c} \tag{1.2}$$

where ν_s is the spin frequency and ν_c is the cyclotron frequency. This relationship is true for any spin 1/2 particle. For a proton, whose g-value is far from 2, measuring this ratio has lead to the most accurate single particle g-factor measurement [1] and

the most accurate measurement of the antiproton g-factor [15]. For the electron, however, the g-factor only deviates from 2 by about a part per thousand. In this case, it is convenient to express the g-factor as:

$$-\frac{\mu}{\mu_B} = \frac{g}{2} = \frac{\nu_s}{\nu_c} = \frac{\nu_s - \nu_c + \nu_c}{\nu_c} = \frac{\nu_a + \nu_c}{\nu_c} = 1 + \frac{\nu_a}{\nu_c} \tag{1.3}$$

where $\nu_a \equiv \nu_s - \nu_c$ is the anomaly frequency (named after the "anomaly" that $g \neq 2$). Since g/2 for the electron deviates only slightly from 1, measuring the anomaly and cyclotron frequencies (rather than the spin and cyclotron) improves the precision of the g-factor by three orders of magnitude for the same measurement precision in the individual frequencies.

As will be discussed throughout this thesis, at the current precision of the electron g-factor, equation 1.3 is modified into equation 1.4, which includes contributions from an imperfect Penning trap (see chapter 2), special relativity (see chapter 6), and a cavity correction (see chapter 6).

$$\frac{g}{2} \simeq 1 + \frac{\bar{\nu}_a - \dfrac{\bar{\nu}_z^2}{2\bar{f}_c}}{\bar{f}_c + \dfrac{3}{2}\delta + \dfrac{\bar{\nu}_z^2}{2\bar{f}_c}} + \frac{\Delta\omega_c}{\omega_c}. \tag{1.4}$$

where the inputs are the measured anomaly frequency, $\bar{\nu}_a$, the measured cyclotron frequency from $|0,\uparrow\rangle$ to $|1,\uparrow\rangle$, $\bar{f}_c$, the measured axial frequency, $\bar{\nu}_z$, the cavity correction, $\frac{\Delta\omega_c}{\omega_c}$, and the special relativistic correction, δ.

1.3 The Fine Structure Constant and g

As mentioned above, the interactions with the vacuum modify g (away from 2) for the electron. The effects of these fluctuations can be calculated in the framework of QED and the Standard Model, with

$$-\frac{\mu}{\mu_B} = \frac{g}{2} = 1 + C_2\left(\frac{\alpha}{\pi}\right) + C_4\left(\frac{\alpha}{\pi}\right)^2 + C_6\left(\frac{\alpha}{\pi}\right)^3 + C_8\left(\frac{\alpha}{\pi}\right)^4 + C_{10}\left(\frac{\alpha}{\pi}\right)^5 + ... + a_{\text{hadronic}} + a_{\text{weak}} \tag{1.5}$$

where a_{hadronic} comes from terms involving hadronic interactions, a_{weak} comes from weak interactions, C_n are the coefficients for the n-vertex QED terms with only photons and leptons, and

$$\alpha = \frac{e^2}{(4\pi\varepsilon_0)\hbar c} \tag{1.6}$$

is the fine structure constant.

The fine structure constant sets the scale for the electromagnetic interaction and is one of the dimensionless input parameters of the Standard Model and our system of fundamental constants. Equation 1.6 is actually the low-energy limit of the fine structure constant, as the vacuum interactions screen the electron charge and can be penetrated at higher energies, and equation 1.5 also refers to this low energy limit.

The C_n coefficients can be calculated by evaluating the Feynman diagrams with n vertices involving photons and leptons. Figure 1.1 shows some of the Feynman diagrams at each relevant order. Because the number of vertices is increasing with each coefficient, so are the number of possible diagrams, as well as the number of integrals necessary to calculate each coefficient.

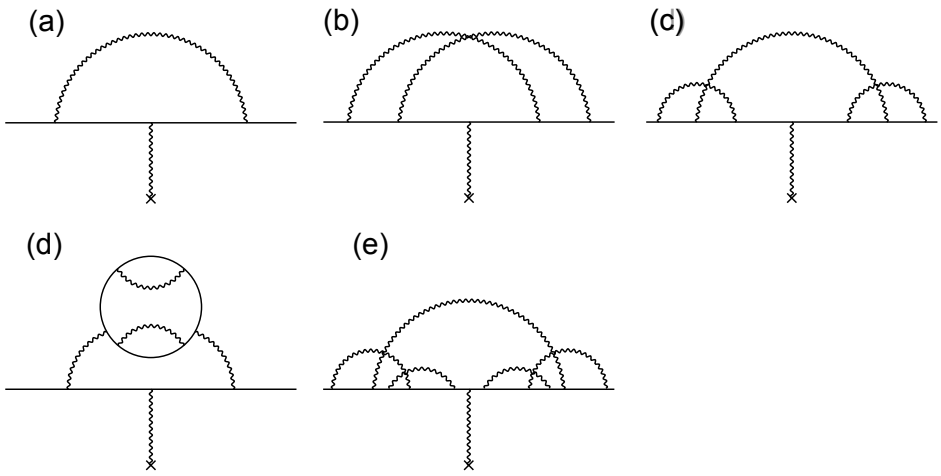

Figure 1.1: An example of the Feynman diagrams contributing to the g-factor: (a) the second order term and (b-e) an example of each of the 4-10th order diagrams, respectively.

The first three coefficients (C_2, C_4, and C_6) have been calculated analytically. The mass independent terms are known exactly and the mass dependent terms are known exactly as functions of lepton mass ratios (m_e/m_μ, m_e/m_τ). Their combined values and uncertanties (arising from the uncertainties in the mass ratios) can be seen in equations 1.7 a-c.

$$C_2 = \frac{1}{2} = 0.5\,(\text{exact}) \qquad [16] \qquad (1.7a)$$

$$C_4 = -0.328\,478\,444\,002\,55\,(33) \qquad [17,\ 18,\ 19,\ 20] \qquad (1.7b)$$

$$C_6 = 1.181\,234\,016\,815\,(11) \qquad [21,\ 20] \qquad (1.7c)$$

C_8 and C_{10} have yet to be calculated analytically, but at the current g-factor precision, they must also be known. Instead, decade long computational calculations

have provided the following numerical values, with C_{10} just calculated for the first time last year.

$$C_8 = -1.909\,7\,(20) \qquad [20,\,22] \tag{1.8a}$$

$$C_{10} = 9.16\,(57) \qquad [20,\,22] \tag{1.8b}$$

For C_{10}, the number of Feynman diagrams is staggering (12,672) and even keeping track of the diagrams becomes cumbersome. Indeed, an automated scheme has been created both to generate and evaluate the integrals associated with these diagrams [23, 24, 25].

The remaining terms in the expansion a_{hadronic} and a_{weak} do not arise from QED. The total contribution from the hadronic loops is given by:

$$a_{\text{hadronic}} = 1.677\ (16) \times 10^{-12} \tag{1.9}$$

and is large enough to contribute to $\frac{g}{2}$ at its current precision. The uncertainty in a_{hadronic} is neglible compared to the other dominant experimental and theoretical uncertainties.

The best estimate for the weak contributions comes the electroweak corrections to the muon magnetic moment [26], scaled down for the electron to give:

$$a_{\text{weak}} = 0.029\ 7\ (5)\ \times 10^{-12}. \tag{1.10}$$

This is an order of magnitude to small to contribute to g/2 at its current precision.

A summary of the contribution of all of these elements and their uncertainties is shown in figure 1.2. For comparison, the figure also shows the 2008 Harvard experimental result.

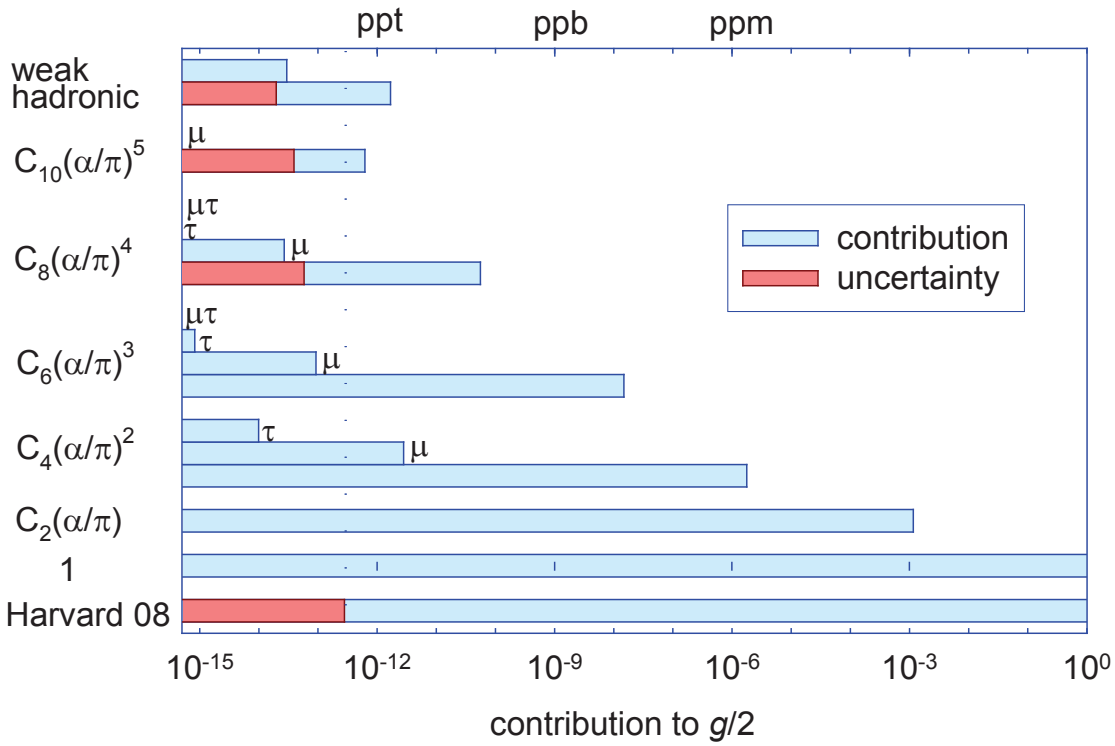

Figure 1.2: A summary of the contributions and uncertainties to g/2.

By inverting the series in equation 1.5, we can extract a value of the fine structure constant in terms of the electron g-factor. At the current precision of the g-factor, this yields the most precise determination of α. However, this makes the assumption that the expansion in equation 1.5 completely encapsulates all of the relevant physics relating g and α. The value of α from inverting the series is

$$\alpha^{-1} = 137.035\ 999\ 173\ (34)\ [0.25\text{ppb}] \tag{1.11}$$

where the number in parentheses is the error and the number in square brackets is the relative uncertainty. With the recent evaluation of C_{10} and update of C_8, the dominant source of uncertainty arises from the g-factor measurement [0.24 ppb] rather than the theory [0.06 ppb].

1.4 Comparisons of α and Tests of QED

By comparing this determination of α with the next most precise independently measured value of α, we can test the physics going into equation 1.5, namely QED. Figure 1.3 shows several of the most precise determinations of α. There are numerous other less precise determinations of the fine structure constant (see, for example, Table XXV in [27]).

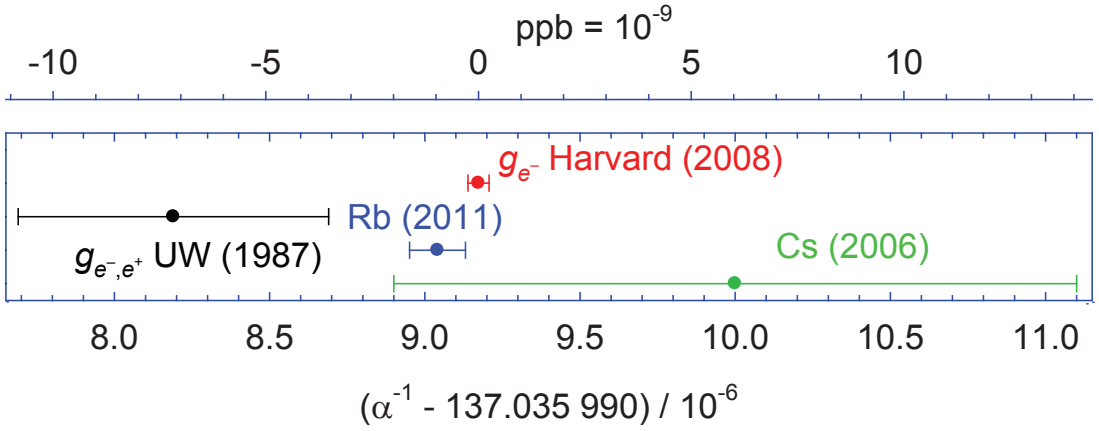

Figure 1.3: Recent determinations of the fine structure constant from g-factor and atom recoil measurements.

Aside from the g-factor, the next most precise determination of α comes from the "atom recoil" experiments. Though this determination actually requires the input from several different experiments, they are named after the measurement of the

recoil velocities of atoms, which limits the uncertainty in the determination of the fine structure constant.

To understand how the measurement can determine the fine structure constant, we begin by rewriting the fine structure constant in terms of the Rydberg constant,

$$\alpha^2 = \frac{2R_\infty}{c}\frac{m_X}{m_e}\frac{h}{m_X} \tag{1.12}$$

where R_∞ is the Rydberg constant, c is the speed of light, m_e is the electron mass, h is the Planck constant and m_X is the mass of the atom used in the recoil experiment. In this expression, nearly each term comes from a different experiment (or experiments). The speed of light, c, is exact in the SI system of units, so it contributes no uncertainty. R_∞ is known to extremely high precision (5.0 ppt) from hydrogen and deuterium spectroscopy [27]. The electron mass is known from a comparison of the cyclotron frequency to that of a fully ionized carbon ion [28] and is known to 2 ppb (or can be determined from bound electron g-factor measurements [29] to $\approx$ 0.4 ppb). The mass of the atoms is also determined by comparisons of cyclotron frequencies of simultaneously trapped ions in Penning traps [30] and are known to better than 0.2 ppb.

Finally, the limiting measurement comes from determining h/m_X. The basic idea of the experiment is to give an atom a momentum "kick" as it absorbs a photon and to measure the recoil velocity. The two most precise experiments involve cesium and rubidium. In the cesium experiment, an atom interferrometer is used to measure the recoil velocity of a cesium atom, which can be used to obtain a value of h/m_{Cs}, and to determine the fine structure constant with a relative uncertainty of 7.4 ppb [31].

The fine structure constant determination from this experiment can be seen in figure 1.3.

A more accurate determination, however, comes from ^{87}Rb. In this experiment, a Ramsey-Borde atom interferometer is combined with Bloch oscillations to coherently transfer many "kicks" to the atom and measure the final veloctiy. This measurement, combined with the others described above, has yielded a determination of the fine structure constant with a relative uncertainty of 0.66 ppb [32]:

$$\alpha^{-1} = 137.035\ 999\ 037\ (91)\ [0.66\ \text{ppb}] \tag{1.13}$$

The comparison of this value to the value determined from the g-factor and equation 1.5 is the best numerical test of QED to date:

$$\frac{\alpha^{-1} - \alpha^{-1}(\text{Rb})}{\alpha^{-1}} = (9.6 \pm 6.9) \times 10^{-10} \tag{1.14}$$

which agrees within 1.4 σ. We could instead use the next most accurate determination of α to calculate $\frac{g}{2}$. This leads to:

$$\frac{g}{2}(\alpha) = 1.001\,159\,652\,181\,84\,(76)\,[0.76\,\text{ppt}] \tag{1.15}$$

with a difference between the experimental and calculated values of:

$$\frac{g}{2} - \frac{g}{2}(\alpha) = (-1.11 \pm 0.81) \times 10^{-12} \tag{1.16}$$

which places a limit of:

$$\left|\frac{\delta g}{2}\right| < 2.0 \times 10^{-12} \tag{1.17}$$

1.5 Limits on Electron Substructure

Placing limits on $\delta g/2$ constrains the new physics that could be entering into the expansion in equation 1.5 [25]. As mentioned above, the proton's rich internal structure modifies the proton g-factor substantially away from 2. The electron could also have an internal substructure. So far none has been found, but the structure could still remain hidden and produce the low mass, small radius electron if it were comprised of very tightly bound constituents of high mass (m^*) [33]. Naively, we might imagine that $\delta g/2 \approx \mathcal{O}(m_e/m^*)$. If we made the assumption that $\delta g/2 = (m_e/m^*)$, we would find very tight limits for the m^* (where $m^* = 2/(\delta g)m_e$) and for the electron radius ($R_e = \hbar/(m^*c)$).

Without lucky cancellations, however, this model would predict a very high contribution to the fermion self energy, and thus, a high electron mass. Since the observed electron mass is much less than m^*, a more natural scaling might be one that supresses the first order contribution due to some symmetry (for example, a chirally invariant model [33]). In this case the first order contribution the the magnetic moment would also cancel, and we would be left with $\delta g/2 \approx \mathcal{O}(m_/m^*)^2$. If we assumed that $\delta g/2 = (m_e/m^*)^2$, then we could again place limits on the mass of the constituent particle, as well as the electron radius. These would be:

$$m^* > 360 \text{ GeV}/c^2 \tag{1.18}$$

$$R_e < 5 \times 10^{-19}\text{m} \tag{1.19}$$

This bound on the electron radius compares favorably with the most stringent

limit set by the Large Electron Positron (LEP) collider, in which they used scattering measurements to look for evidence of contact interactions at 10.3 TeV [34], which places a limit on the electron radius of $R_e \lesssim \hbar c/E = 2 \times 10^{-20}$ m.

1.6 CPT

Because of its high precision and because the recent techniques for measuring the electron g-factor can be used on positrons as well as electrons, the g-factor is an ideal system in which to test charge, parity, and time reversal (CPT) symmetry. CPT combines three separate discrete symmetries: charge conjugation (where antimatter is transformed into matter), parity (where all spacial coordinates are reversed so that $\vec{r} \to -\vec{r}$), and time reversal ($t \to -t$).

At one time, each of these symmetries was believed to be an exact symmetry of nature. A groundbreaking experiment measuring the axial assymmetry of electrons emitted in the beta decay of ^{60}Co [35], however, revealed parity violation (in interactions containing the weak force). It was then posited that perhaps the combined symmetry of charge conjugation and parity (or CP) was instead the preserved symmetry. In 1964, it was discoverd that the K_2^0 meson could decay to 2 pions through a CP violating decay [36], and several more meson decays have also since shown CP violation [37, 38, 39].

Presently, the combined symmetry of CPT is believed to be a valid symmetry, and the CPT theorem states that any quantum field theory that satisfies some assumptions (e.g. locality and lorentz invariance) must obey CPT symmetry [40]. However, gravity cannot yet be described by a quantum field theory and CPT remains an open topic of

investigation. One consequence of the CPT theorem is that particle and anti-particles should have equal masses, energy levels, magnitudes of charge and magnetic moments, etc. Experimental searches have repeatedly confirmed the validity of CPT in several systems. See figure 1.4 for some of the best tests of CPT.

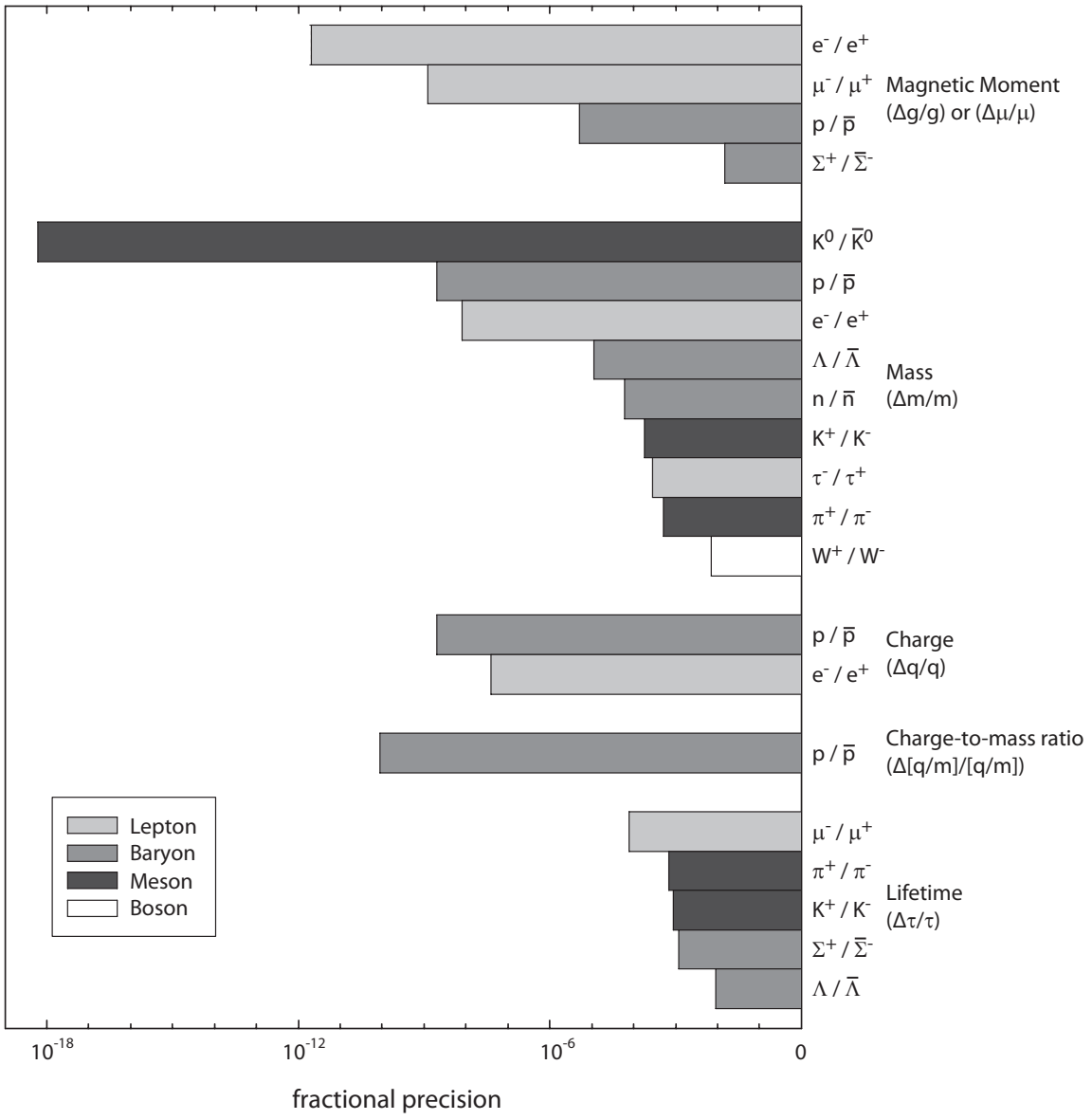

Figure 1.4: The fractional precision of various tests of CPT. The data is compiled from [41] and [15].

The comparison of the electron and positron g-factor is currently the best test of CPT in a lepton system and one of the best tests of CPT to date [10]. The limit comes from the 1987 Univeristy of Washington g-factor comparison and is given by:

$$r_g \equiv |(g_- - g_+)/g_{av}| \lesssim 2.1 \times 10^{-12} \tag{1.20}$$

Our group has measured the electron g-factor more precisely (by a factor of nearly 20), but in an apparatus that lacked a method for loading positrons to perform a similarly precise measurement [2]. With the apparatus described in this thesis, there is reason to believe the positron will be measured with at least the precision of the 2008 electron measurement.

Currently, the precision of the g-factor comparison as a test of CPT is only beaten by a comparison of the nuetral kaon and anti-kaon mass [42, 43]. This measurement, which takes advantage of a large cancellation in the masses of K_L and K_S, finds that:

$$r_K \equiv |(m_K - m_{\bar{K}})/m_K| \lesssim 6 \times 10^{-19} \text{ [90\% CL]} \tag{1.21}$$

Despite the high precision of these experiments, it remains important to pursue CPT violation in a variety of systems (baryons, leptons, bosons, etc.) and measurements (masses, magnetic moments, energy levels, etc.), as we do not yet know what form any violation might take.

The benefit of the measurements shown in figure 1.4 is that any difference observed in these parameters would constitute a violation of CPT. In the search for CPT violations, however, a model for how CPT might be violated might provide a more directed search. One such model is a standard model extension [44], which allows for

CPT and Lorentz violations, but preserves gauge invariance, microcasuality, power counting renormalizability, conservation of energy, conservation of momentum, and covariance under observer rotations and boosts (though it allows covariance to be broken for the particle's reference frame).

The extension adds terms to the standard model Lagrangian that satisfy the above requirements and are also Hermitian. These additions can be parameterized with constants whose limits can be bound by several experiments (for a summary, see [45]). In the context of the g-factor experiment, the extension serves to modify the Dirac equation [46, 47] to:

$$\Big(\imath\gamma^\mu\partial_\mu - eA_\mu\gamma^\mu - a_\mu\gamma^\mu - b_\mu\gamma_5\gamma^\mu - \frac{1}{2}H_{\mu\nu}\sigma^{\mu\nu} + \imath c_{\mu\nu}\gamma^\mu\partial^\nu - eA^\nu c_{\mu\nu}\gamma^\mu + \imath d_{\mu\nu}\gamma_5\gamma^\mu\partial^\nu - qA^\nu d_{\mu\nu}\gamma_5\gamma^\mu - m\Big)\psi = 0 \quad (1.22)$$

where a_μ and b_μ are CPT violating coupling constants and $c_{\mu\nu}$, $d_{\mu\nu}$ and $H_{\mu\nu}$ are CPT preserving coupling constants. An analysis of these contributions for our system [46] reveals that the primary coefficient that has a measurable effect is b_3, whose presence can be seen in the difference in anomaly frequencies for the electron and positron:

$$\Delta\omega_a = \left(\omega_a^- - \omega_a^+\right) = -4b_3 \quad (1.23)$$

In addition, the framework provides a methodology for comparing tests of CPT that is a more direct comparison of a CPT violating parameter [46] (rather than comparing masses, charges, coupling constants, etc. directly). For our system, they posit that the CPT figure of merit, which is more comparable to the energy scaling

of the kaon CPT violating parameter in equation 1.21, should be:

$$r_e \equiv \left| \left(E^-_{n,s} - E^+_{n,-s} \right) / E^-_{n,s} \right| \tag{1.24}$$

which reduces to:

$$r_e = \left| \frac{\Delta\omega_a}{2m} \right| = \left| \frac{2b_3}{m} \right| \tag{1.25}$$

For the 1987 g-factor measurement, this sets a limit of $r_e \lesssim 12 \times 10^{-22}$ [48]. Since $\vec{b}$ violates Lorentz invariance by having a fixed direction in space, it is possible to set a bound on the magnitude of $\vec{b}$ by measuring b_3 as the earth rotates around its axis (or as the earth rotates around the sun). For the University of Washington data, this places a limit of $\left|\vec{b}\right| \lesssim 50$ rad/sec [48], which could have been $\left|\vec{b}\right| \lesssim 0.7$ rad/sec for the most fortuitous alignment of $\vec{b}$ and the magnetic field. Any improvement in the electron positron g-factor (or anomaly) measurements could significantly improve these bounds.

1.7 Summary

This chapter has discussed the motivations for improving the electron and positron g-factor measurements, which include improving the determination of the fine structure constant and tests of QED, setting limits on electron substructure and improving the best test of CPT in a lepton system. The remaining chapters will describe the apparatus, techniques and measurements we have made on our way toward an improved g-factor measurement, with a focus on the single electron quantum jump spectroscopy.

Chapter 2

Penning Traps

Though it would be ideal to measure the electron and positron magnetic moments in free space, practically, we cannot perform these measurements if the particles are not first confined long enough for a precise measurement. One of the key techniques that allows for precision spectroscopy on single electrons and positrons is the ability to trap charged particles. Although a number of schemes exist to trap ions [11, 49, 50], all of the work in this thesis takes place in Penning traps, which are described here.

Beginning with a discussion of ideal traps and their effect on the free space motions of an electron or positron, we will also explore real Penning traps—including their possible geometries and imperfections—and an invariance theorem that allows us to account for these imperfections in the measured trap frequencies. Finally, the various frequencies and damping timescales for the traps used in this work will be discussed.

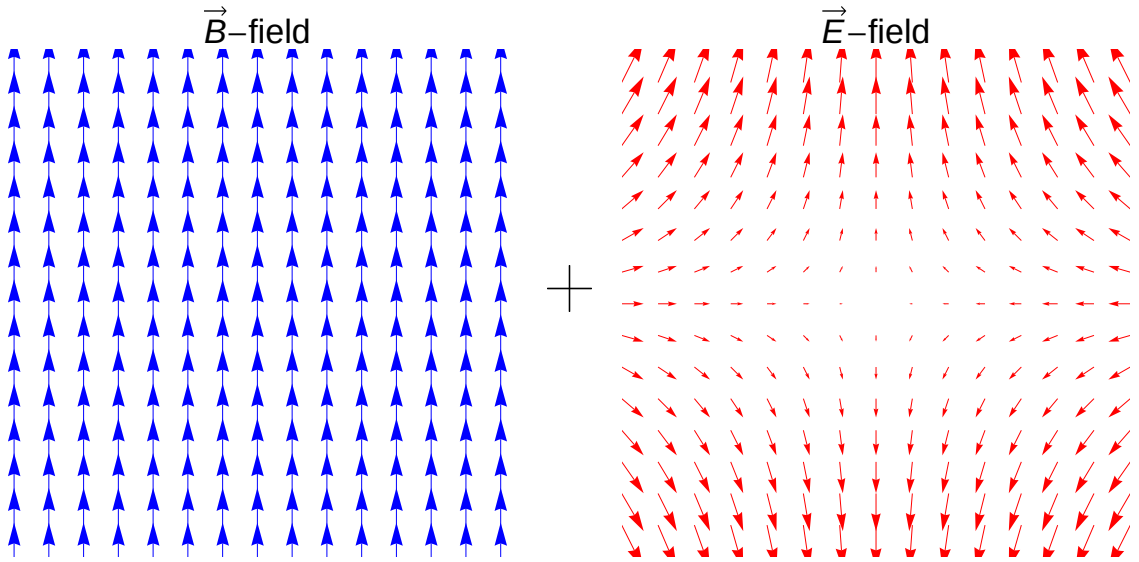

Figure 2.1: An ideal Penning trap is the superposition of an axial magnetic field (seen in blue) plus an electrostatic quadrupole (seen in red). The above electric field configuration has been chosen to make a trapping potential for an electron. For a positron, only the sign on the electric field needs to be reversed.

2.1 Ideal Penning Traps

The Penning trap is a superposition of a strong, homogeneous magnetic field (equation 2.1) and an electrostatic quadrupole (equation 2.2). These fields can be seen in figure 2.1. The homogenous magnetic field provides radial confinement of a charged particle; the electrostatic quadrupole adds axial confinement, while slightly reducing the radial confinement.

$$\vec{B} = B\hat{z} \tag{2.1}$$

$$V \propto z^2 - \frac{\rho^2}{2} \tag{2.2}$$

Though the Penning trap confines a charged particle to allow for spectroscopy, the addition of the trapping fields has some added consequences. To consider the effect of these fields, let us first consider an electron or positron in a magnetic field in free space. For a positron or electron of mass m and charge ±e in a magnetic field $B\hat{z}$, the particle will have a cyclotron frequency

$$\nu_c = \frac{eB}{2\pi m} \tag{2.3}$$

and a spin frequency

$$\nu_s = \frac{2\,|\vec{\mu}|\,B}{h} = \frac{g}{2}\nu_c, \tag{2.4}$$

where h is the Planck constant and $|\mu|$ is the magnitude of the magnetic moment so that $\vec{\mu} = \mu\ \vec{S}/(\hbar/2)$ and $\mu/\mu_B = -g/2$.

With the addition of the electrostatic quadrupole, however, 4 characteristic frequencies arise: the unchanged spin frequency, the axial frequency, the trap-modified cyclotron frequency and the magnetron frequency. The axial frequency, ν_z arises from the harmonic axial confinement from the electrostatic quadrupole. The quadrupole also slightly weakens the radial confinement, which leads to a modified cyclotron frequency, $\nu_c^{'}$ and also adds a new motion, the magnetron motion (with a frequency ν_m), which can be thought of as arising from a slow $\vec{E} \times \vec{B}$ drift. The 3 motional frequencies are represented in figure 2.2 (not to scale).

For a perfect quadrupole, the trap-modified cyclotron frequency

$$\nu_c^{'} = \nu_c - \nu_m \tag{2.5}$$

differs from the free space cyclotron frequency only by the magnetron frequency [11]

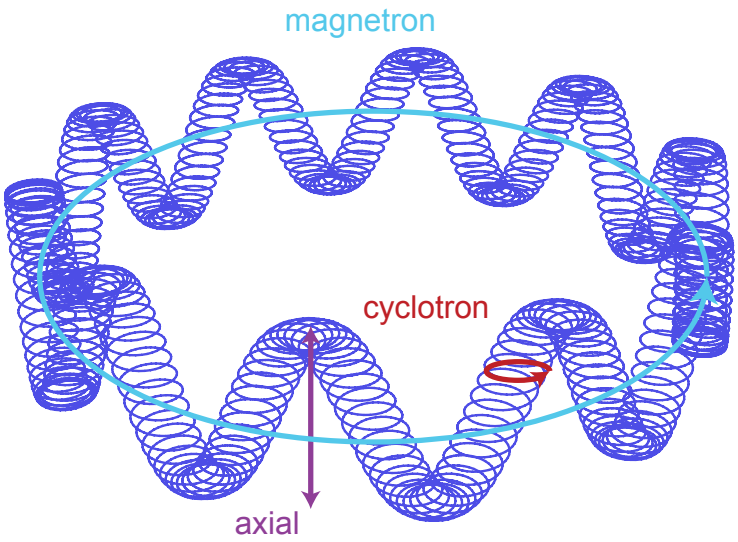

Figure 2.2: The motions of an electron in a Penning trap. Note that the relative sizes are not to scale for the relative frequencies used in this work.

$$\nu_m = \frac{\nu_z^2}{2\nu_c'} \tag{2.6}$$

2.2 Real Penning Traps

Although a discussion of ideal Penning traps provides a useful framework for understanding the motions and frequencies involved with the addition of the electrostatic quadrupole, in the real world, we can realize only an approximation. There are, however, several ways to make a good approximation. This is normally done by fabricating a Penning trap out of electrodes with a carefully selected geometry to produce the desired potential.

The most straightforward of these geometries is to place the surfaces of the electrodes on the equipotentials of the electrostatic quadrupole. These traps are typically

called hyperbolic Penning traps (because the electrodes are hyperbolas of revolution), and an example can be seen in figure 2.3. To produce a perfect quadrupole potential, these electrodes would have to extend infinitely, be perfectly conducting and be perfectly machined. Though these constraints cannot be realized, optimized designs have been discussed [51], and many succesful hyperbolic traps have been constructed and used, for example, in the observation of a single trapped electron [7] and a previous comparison of the electron and positron g-factors [10].

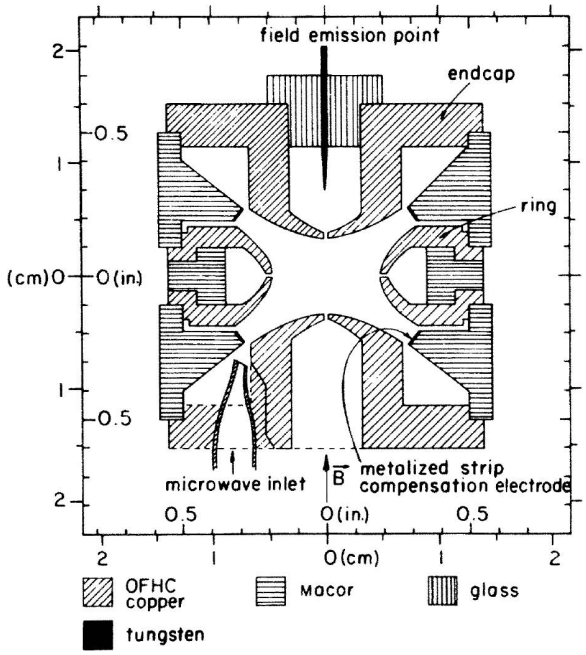

Figure 2.3: An example of a hyperbolic Penning trap. Figure taken from [52]: a schematic of the first trap to exhibit inhibited spontaneous emission.

The earliest alternative to the hyperbolic electrodes was the cylindrical Penning trap (figure 2.4) proposed long ago for electron magnetic moment experiments [53]. Other geometries can also be useful. Open endcap Penning traps [54] can be made to approximate the quadrupole potential and are useful when axial access is necessary (for transferring particles, or loading from an accelerator or ion source). We employ

an open endcap Penning trap (figure 2.5) to improve the positron loading rate (see chapter 5). Planar Penning trap geometries (see figure 2.6) have also been proposed [55] and may be a viable option for making harmonic Penning traps stable enough to detect a single electron.

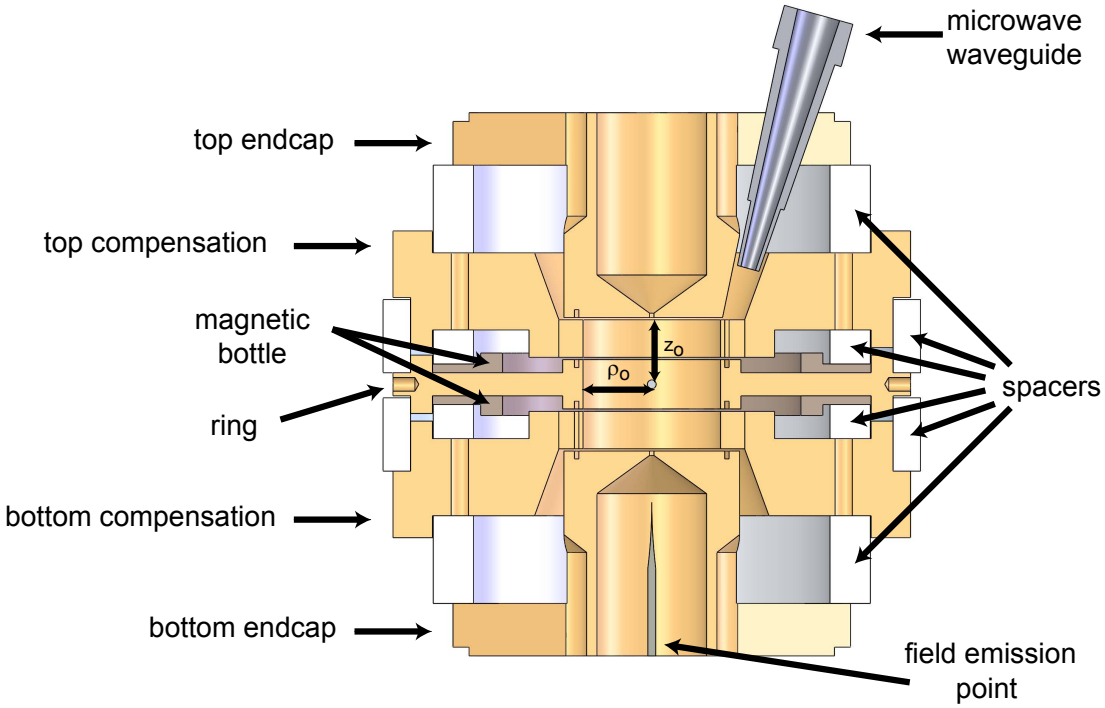

Figure 2.4: A cross section of the cylindrical Penning trap used for most of this work. This trap is also referred to as the "precision" trap, to distinguish it from the open endcap, loading trap. The dimensions, z_0 and ρ_0 are the radius and half height of the cylindrical trap, and their values are listed in table 2.1.

Figure 2.5 shows a cross-sectional view of the "loading" trap as an example of an open endcap trap. The cylindrical trap (similar to the one used in this work) has produced a sufficiently harmonic pontential to observe a single electron [56], and has also been used in the previous installment of the electron g-factor measurement [2] to make the most accurate measurement of a property of a fundamental particle to date.

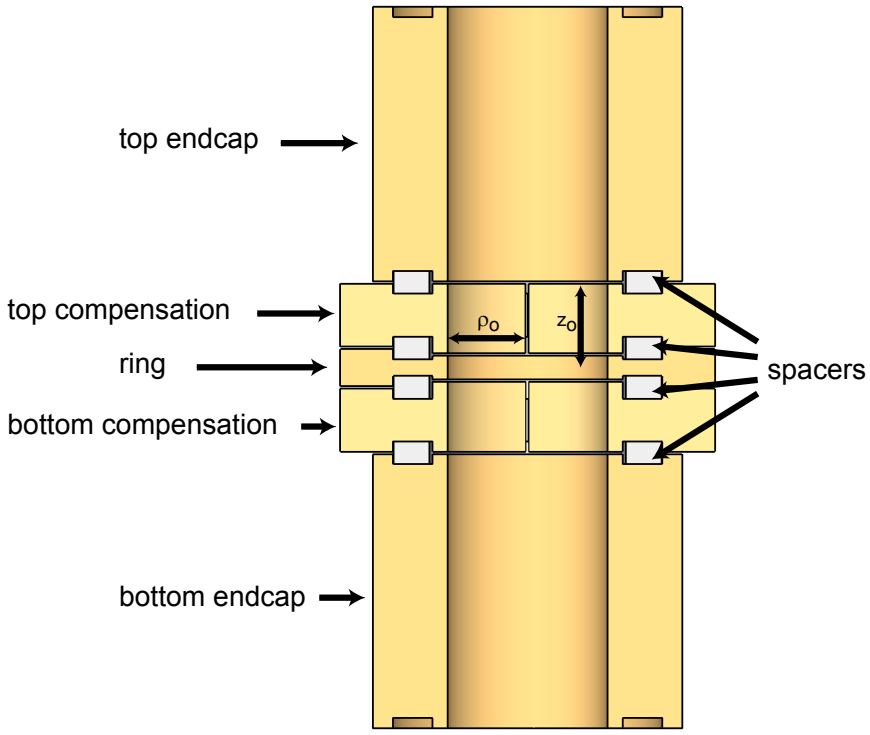

Figure 2.5: A cross sectional view of the open endcap Penning trap used to accumulate positrons. This trap is frequently referred to as the "loading" trap to distinguish it from the cylindrical trap in which spectroscopy is performed. The dimensions, z_0 and ρ_0 are defined in the figure, and their values are listed in table 2.1.

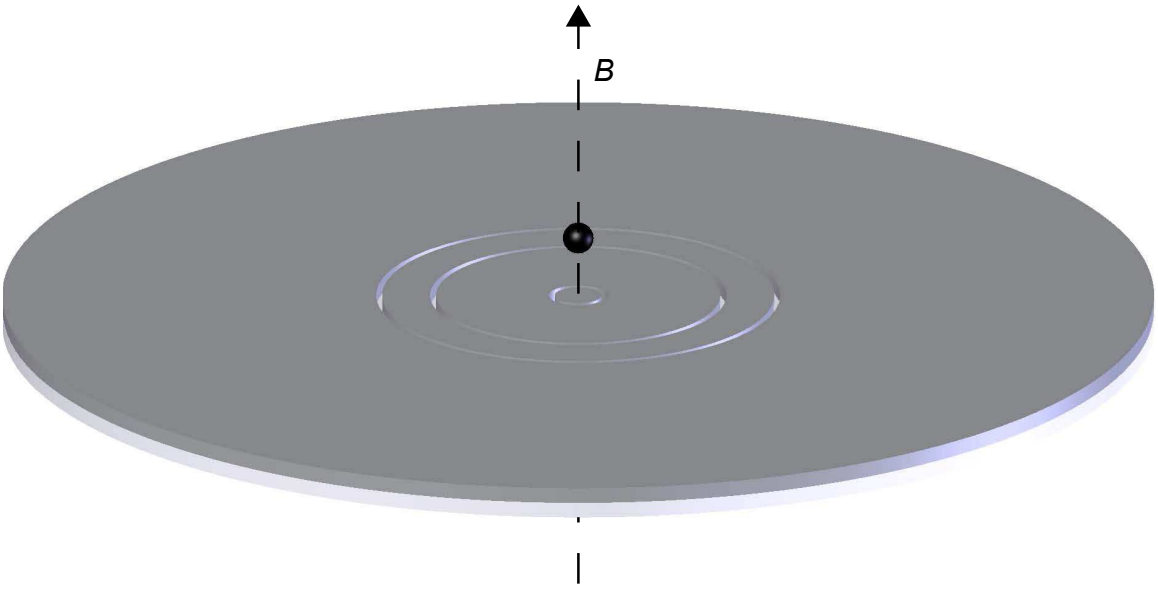

Figure 2.6: A three-gap planar trap with an electron (not to scale) drawn in to show the trapping region. Taken from [55].

Perhaps its greatest advantage (compared to the other geometries discussed so far), however, is its analytically calculable and easily identifiable cavity mode structure, used to control the radiation field and modify the electron's spontaneous emission. The advantages of this will be discussed further in chapter 6.

In our typical setup, we apply the potential V_R between the ring and endcap electrode to set the depth of the potential well, we apply V_{Comp} to the compensation electrodes to tune the anharmonicity of the potential well, and we ground the endcaps. The values of these voltages and other typical trap parameters for both the loading and precision trap can be seen in table 2.1.

With a particular geometry of electrodes in mind, it is now possible to characterize the electrostatics of our cylindrical Penning trap. These ideas can be extended to the other geometries listed, though some goemetries have the disadvantage of less

Table 2.1: Dimensions and typical values for both the precision and loading traps.

Precision Trap Parameters		**Loading Trap Parameters**	
z_0	0.3880 cm	z_0	0.3186 cm
ρ_0	0.3995 cm	ρ_0	0.3001 cm
Δz_c	0.2337 cm	Δz_c	0.2703 cm
V_R	96.98 V	V_R	-8.537 V
V_{EC}	0 V	V_{EC}	0 V
V_{Comp}	79.19 V	V_{Comp}	- 7.567 V
B	5.2 T	B	5.2 T

symmetry [55]. It is useful to define a trap dimension constant, d:

$$d^2 = \frac{1}{2}\left(z_0^2 + \frac{\rho_0^2}{2}\right) \tag{2.7}$$

where ρ_0 and z_0 are defined in figure 2.4. The potential near the center of the trap can be expanded in a series:

$$V = -V_R \frac{z^2 - \frac{\rho^2}{2}}{2d^2} - \frac{V_R}{2}\sum_{\substack{k=0 \\ \text{even}}}^{\infty} C_k \left(\frac{r}{d}\right)^k P_k(Cos(\theta)) \tag{2.8}$$

where symmetry under $z \rightarrow -z$ is assumed. Here, V_R is the potential on the ring electrode, z is the axial coordinate, r is the spherical radial coordinate, θ is the angle (defined from the z-axis), ρ is the cylindrical radial coordinate, d is the trap dimension as defined above, C_k are the trap coefficients and P_k are the Legendre polynomials.

To show the dependence on the compensation electrode potential, we can further

separate out the trap coefficients into terms that depend solely on geometry, C_k^0, and a term that depends explicitly on the compensation voltage, D_k, as in equation 2.9. For a given choice of geometry, these coefficients can be calculated explicity, as shown by the expressions in [11, 57], and the values for our traps are given in [58].

$$C_k = C_k^{(0)} + D_k \left(\frac{1}{2} - \frac{V_{Comp}}{V_R} \right) \tag{2.9}$$

We can now explicitly write down an expression for the axial frequency.

$$\nu_z = \frac{1}{2\pi} \sqrt{\frac{eV_R}{md^2} (1 + C_2)} \tag{2.10}$$

The compensation potential affects the axial frequency via the coefficient D_2. Since we use the compensation voltage to tune the anharmonicity of the potential well, it is convenient to have the axial frequency independent of this tuning parameter. D_2 can be set to 0 by carefully choosing the geometry of the ring and compensation electrodes and traps with $D_2 = 0$ are said to be "orthogonalized" [51]. The cylindrical Penning trap described in this thesis is an example of such an orthogonalized trap [53].

2.3 Brown-Gabrielse Invariance Theorem

Thus far, we have only discussed imperfections in approximating an electrostatic quadrupole with real electrode geometries. These imperfections can lead to anharmonic terms in the potential, which can be accounted for and minimized with a careful choice of geometry and the adjustment of a compensation voltage (see more about tuning the anharmonicity of a trap in chapter 5). Unfortunately, this does not

cover the spectrum of imperfections that could arise in a real Penning trap. Slight changes in the dimensions (which always exist within the machining tolerances) or patch potentials (which are harder to quantify) could still cause harmonic distortions to the potential or lead to a misalignment of the strong axial magnetic field and the electrostatic quadrupole.

Fortunately, these imperfections can be carefully accounted for. This analysis leads to an invariance theorem,

$$\nu_c^2 = \bar{\nu}_c^2 + \bar{\nu}_z^2 + \bar{\nu}_m^2 \tag{2.11}$$

which relates the measured trap frequencies (each denoted with a bar over the top of them) to the free space cyclotron frequency, which we are interested in for the magnetic moment measurement. The relationship is derived in [59]. In the case where $\bar{\nu}_c \gg \bar{\nu}_z \gg \bar{\nu}_m$, the free space cyclotron frequency can be approximated by the familiar expression from the ideal Penning trap.

2.4 Damping rates, Equilibrium and Stability

A Penning trap is not an intrensically stable ion trap—the magnetron motion is an inverted harmonic oscillator [11]. On a long enough timescale, the magnetron radius grows as the motion decays, until an electron or positron is lost from the trap. The cyclotron and axial motions, however, can both be represented by harmonic oscillators, and are therefore stable. Any damping mechanisms in these motions should drive a particle towards its axial or cyclotron ground state with some associated time scale. However, the equilibrium state for each of these motions is not necessarily

the ground state, but rather depends on the details of the energy level spacing for each motion, and the temperature of the bath to which each motion is coupled.

For our typical magnetic field of about 5.2 T, the cyclotron energy spacing is about about 7 K (in temperature units). As we will see below, the cyclotron motion is in radiative equilibrium with the trap electrodes, which are held constant at 100 mK. Since the cyclotron motion is in thermal equilibrium with the electrodes, the distribution of states follows a simple Boltzmann distribution. Since the temperature is small compared to the level spacing, the odds of being in anything but the ground state are suppressed by the Boltzmann factor of $e^{-\frac{h\nu}{k_B T}}$. For the first excited state, this suppression is already $\approx e^{-70}$, so the cyclotron is effectively always in its ground state.

The axial motion is in thermal equilibrium with the detection electronics. Though the axial temperature can vary somewhat [2], it is believed to be set by the temperature of the amplifier that detects the axial motion. See chapter 7 for a discussion on how to measure the axial temperature. In the previous version of the experiment [13], this temperature varied between 0.23 and 1.09 K at different magnetic field values (when the amplifiers were off). This variation in temperatures was not fully understood, but given this range, we can see that the axial motion is far from its ground state. At our typical axial frequency of about 200 MHz, the energy spacing of the axial levels is $\approx 0.01K$, which means that the average quantum number (k) is > 10.

In addition to the equilibrium state, each of the damping timescales is important for spectroscopy or an eventual g-factor measurement. For the unstable magnetron motion, the damping time needs to be very long compared to the measurement time

(so we do not lose the electron or have its magnetron radius change too much) which we achieve with careful filtering and due to the magnetron's low coupling. For the axial motion, the damping timescale sets the time necessary for the axial motion to cool and also determines the amount of axial signal measured (see chapter 5). For the cyclotron motion, the damping rate determines the amount of time that the electron spends in its first excited state after a successfully driven cyclotron excitation. This timescale must be at least long enough to get the necessary averaging time to detect that a cyclotron transition has occured (see chapter 7).

For the cyclotron motion, the primary damping mechanism is radiative. Since the electron and positron are charged particles, any acceleration leads to radiated power (as is given by the Larmor formula in equation 2.12), which damps the motion.

$$P = \frac{e^2 a^2}{6\pi\varepsilon_0 c^3} \tag{2.12}$$

Where a is the acceleration, c is the speed of light and ε_0 is the permittivity of free space.

The amount of radiated power is highly frequency dependent, as the acceleration scales as the frequency of a given motion. The axial and magnetron motions are also damped radiatively, but for the precision trap shown in Figure 2.4 and the biases we apply in table 2.1, with very long lifetimes.

In the case of the axial motion, our method of detection (see chapter 5) reduces the axial time constant considerably by adding a resistive damping mechanism. For the magnetron motion, the radiative damping timescale is so long that it is difficult to even measure. Practically we find that the motion tends to damp much more quickly (on

Table 2.2: Precision trap frequencies and radiative damping rates.

Trap Motion	**Frequency**	**Radiative Damping**
magnetron	$\nu_m \approx 137$ kHz	$\gamma_m^{-1} \approx 4$ Gyr
axial	$\nu_z \approx 200$ MHz	$\gamma_z^{-1} \approx 1$ yr
cyclotron	$\nu_c \approx 145.5$ GHz	$\gamma_c^{-1} \approx 100$ ms
spin	$\nu_s \approx 145.7$ GHz	$\gamma_s^{-1} \approx 5$ yr

Table 2.3: Loading trap frequencies and radiative damping rates. Note that the cyclotron and spin motions aren't addressed in the loading trap, so their values are estimated from the value of the magnetic field in the precision trap center.

Trap Motion	**Frequency**	**Radiative Damping**
magnetron	$\nu_m \approx 9.75$ kHz	$\gamma_m^{-1} \approx 10 \times 10^{12}$ yr
axial	$\nu_z \approx 53.3$ MHz	$\gamma_z^{-1} \approx 62$ yr
cyclotron	$\nu_c \approx 145$ GHz	$\gamma_c^{-1} \approx 100$ ms
spin	$\nu_s \approx 145$ GHz	$\gamma_s^{-1} \approx 5$ yr

the order of days), likely due to magnetron heating (see below) or accidental resistive damping of the motion, so we prevent the radius growth with sideband cooling [11]. The radiative damping timescales can be seen in table 2.2 for the precision trap and in table 2.3 for the loading trap. Note that the cyclotron and spin frequencies are not measured in the loading trap, but are instead estimated from the expected magnetic field shift between the loading trap and the precision trap.

The damping timescale for the cyclotron motion is listed as if the the cyclotron were in free space. In practice, the Penning trap forms a microwave cavity that can inhibit spontaneous emission [52] by more than 2 orders of magnitude by reducing the density of states that the into which the cyclotron motion can radiate. This increase in lifetime provides the necessary time to average long enough to measure the cyclotron motion in its excited state, and varies with each cyclotron frequency

(see chapter 6).

2.5 Magnetron Cooling

After loading, transferring, or to counteract heating in between measurements, we need a method to reduce the magnetron radius. If we apply a drive at the axial frequency plus or minus the magnetron frequency (to one half of a split compensation electrode), we can drive a sideband of the axial frequency that exchanges energy between the axial magnetron motion. As we are interested in decreasing the magnetron radius, we typically apply the sideband that is the sum of these frequencies $\omega_z + \omega_m$. Because the harmonic oscillator of the magnetron motion is inverted, this "sideband cooling" actually adds energy to the magnetron motion, pushing the electron up the potential hill to a smaller magnetron radius.

Ideally, we would cool the magnetron motion to its ground state ($l = 0$, where l is the quantum number of the magnetron motion). In practice, however, there is a limit to the amount of "cooling" we can do on the magnetron motion. If we denote the axial quantum number as k, the cooling limit occurs when $l = k$. This limit can be understood by considering the transition rates when a drive of $\omega_z + \omega_m$ is applied to the particle [11]. Two separate transitions can occur. Cooling occurs when a transitions is driven such that $|k, l\rangle \rightarrow |k+1, l-1\rangle$ but heating occurs when $|k, l\rangle \rightarrow |k-1, l+1\rangle$. The transition rate for the cooling process contains the term $a_z^\dagger a_m$ and therefore carries a factor of $(k+1)l$. The heating rate, on the other hand has the operator $a_z a_m^\dagger$, which carries the factor $k(l+1)$. Since these factors are the only difference between the cooling and heating rates, it is now easy to see that the

cooling and heating rates balance when $k = l$. This cooling limit can be derived from thermodynamic principles, as well [60].

Chapter 3

A New Apparatus

The previous chapter covered an overview of the physics of Penning traps, including some of the imperfections that can be accounted for in real Penning traps. In practice, it takes a significant amount of supporting equipment to make our Penning trap work. This chapter will focus on the apparatus, consisting of a superconducting solenoid, cryogen spaces and a dilution refrigerator that allow us to have 100 mK Penning trap in a 5.2 T magnetic field. Chapter 5 discusses the electronics necessary for such a trap.

The following apparatus is new for the work done in this and another [58] thesis. Its benefits over the previous version of the apparatus [2] include increased space for a positron loading source, improved cooling power at 100 mK, improved mechanical stability between the trap and the magnet, increased cryogen volumes for longer cryogen hold times and the addition of a helium reliquifier. The realization of these improvements is discussed in detail below.

3.1 Superconducting Solenoid

At the heart of our apparatus is the superconducting solenoid that generates the up to 6 T confining magnetic field for our Penning trap. We use a Cryomagnetics model 4983, which consists of a 6 T main superconducting coil, a ± 0.5 T Z0 superconducting coil, 11 superconducting shim coils (Z, Z2, Z3, X, Y, ZX, ZY, C2, S2, Z2X and Z2Y) and a Gabrielse-style shield coil [61].

The main coil is made from monofliament niobium titanium (NbTi) and is designed to run in persistent mode (i.e. the current flows without being connected to the power supply). It produces 6 T at 45.33 A and has an inductance of 210 H. The Z0 coil is also a monofliament NbTi coil, but it only produces 0.5 T with 39.7 A and has an inductance of 1.8 H. The smaller field from the Z0 coil allows for finer control of the homogeneous field at the center of the solenoid. Both the main coil and the Z0 coil are powered by a cryomagnetics CS4-10V power supply.

The 11 shim coils are designed to provide their full fields at only 1 amp of current. They are powered by a custom current supply designed and built by the Harvard physics electronic instrument design lab. The current supply provides currents of up to 1.25 A with stability (jitter and drift) at better than one part in 10^{-5}. The output is also insensitive to changes in temperature of a few degrees C (the amount the lab temperature tends to vary over the course of the day) at the part in 10^{-5} level, as well. These shim coils can be used to produce a very homogeneous magnetic field, as discussed in chapter 4.

The Gabrielse-style shield coil is an extra pair of superconducting coils added to guard against external fluctuations in the homogeneous magnetic field [61]. The

geometry of the loops is chosen such that, when a homogeneous external magnetic field is applied, the condition that $\int B \cdot dA = 0$ also ensures that the magnetic field does not change at the center of the solenoid. Cryomagnetics measured a shielding factor of >1000 when they applied a magnetic field from an external Helmholtz coil. Though this is an order of magnitude better than the magnet in which the 2008 g-factor measurement was made, the coil Cryomagnetics used only approximates a homogenous field. Thus, the shielding factor for the magnet may actually be less than the measured value.

Despite the numerous advantages this new magnet offers, when the magnet first arrived, it regularly quenched during charging (typically around half of the stated field value). A thorough investigation revealed two disturbing facts. Firstly, the X-shim persistent switch heater (PSH) was disconnected (see figure 3.1a). Second, the wiring of the coils was different than the manual claimed, as Cryomagnetics had tested the magnet in one configuration, then modified it and shipped it without further testing. Since the X-Shim coil remained superconducting during charging, it would build up enough current to quench the shim coil. When the shim coil rapidly quenched, it would sometimes cause the main coil to quench, as well, leading to our charging difficulties. Our repair of the X-shim heater can be seen in figure 3.1, after which we have had no problems charging the magnet.

3.2 Dilution Refrigerator and Experimental Insert

Both the loading and precision trap are kept at 100 mK by being in thermal contact with the mixing chamber stage of a Janis Research Company Model JDR-500 ^3He-

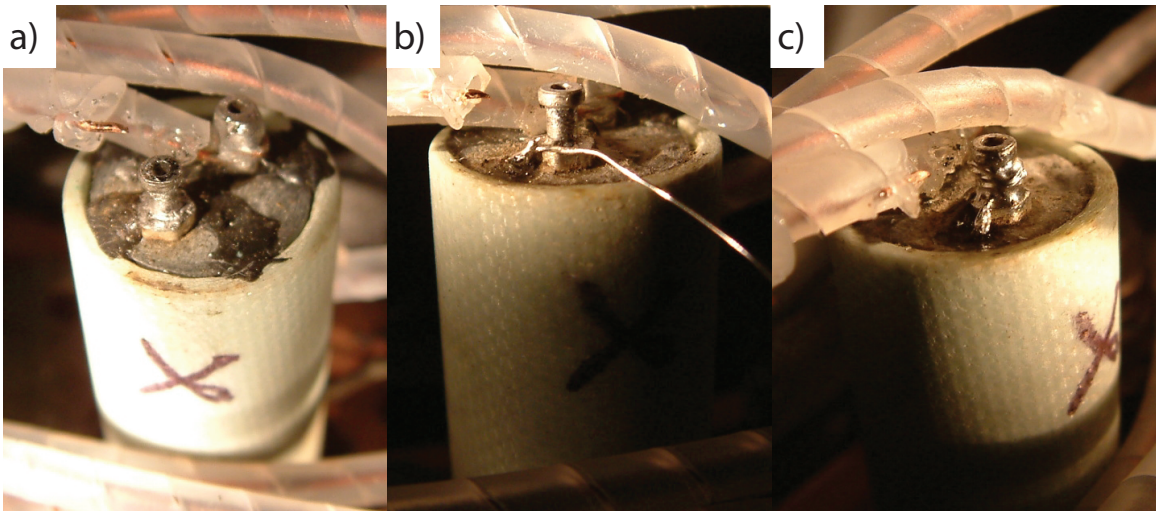

Figure 3.1: Fixing the persistent switch heater on the X-shim: a) the persistent switch heater (PSH) is buried under the epoxy and disconnected from the its lug, b) the PSH lead is extricated and a new wire is soldered on, and c) the wire is soldered onto the lug.

^4He dilution refrigerator system, which can provide up to 330 μW of cooling power at 100 mK (as measured without the trap wiring). The five stages of the refrigerator (4K plate, 1K pot, still, intermediate cold plate (ICP), and mixing chamber (MC)) are kept thermally isolated from one another and are all held under vacuum within an inner vacuum can (IVC). The IVC is surrounded by liquid helium within the Dewar and has several ports that extend to room temperature for access to the experiment (for microwaves, electronics, positron source, etc).

Extending from the mixing chamber plate there are two custom made silver tripod extensions (one included from Janis and one made in house), which provide room for cold electronics and locate the traps in the center of the superconducting solenoid (with the precision trap centered in the solenoid). The tripod region is home to the first stage of detection amplifiers and the electronic components that provide the final stage of filtering for signals going to the electrodes (see chapter 5), and can be seen

in figure 3.2.

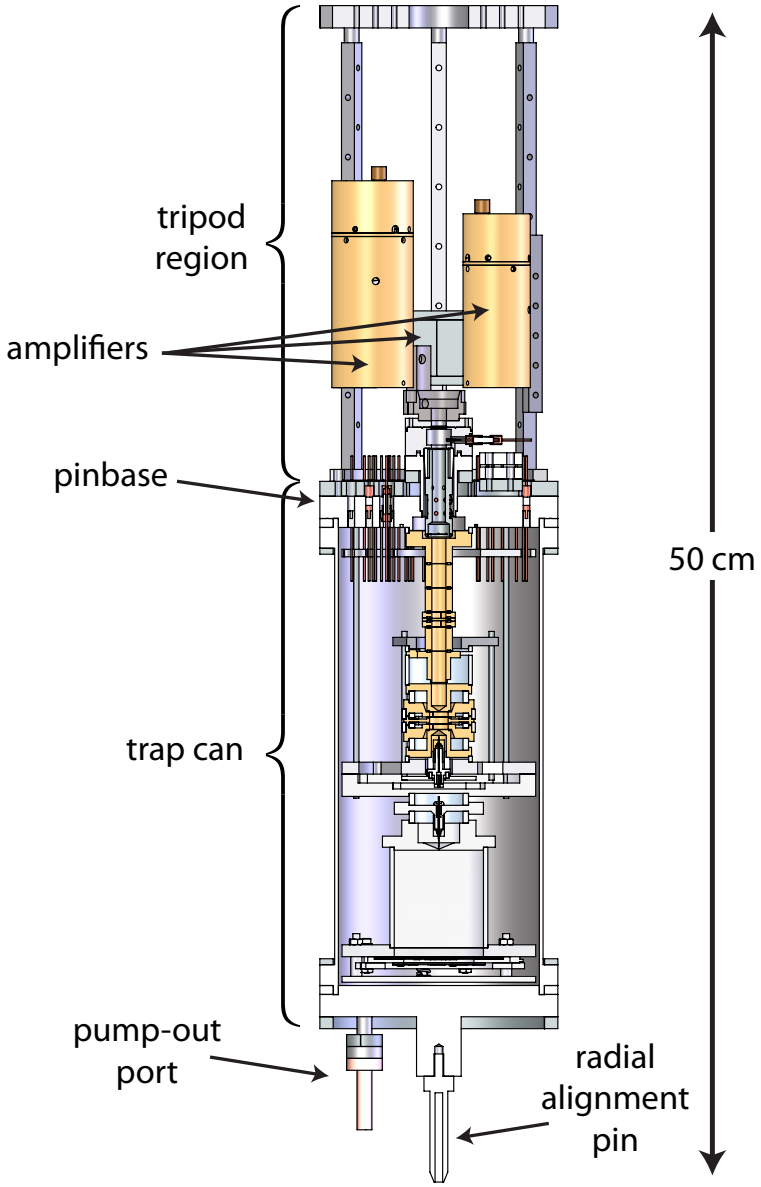

Figure 3.2: A schematic of the tripod and trap can region.

Attached to the bottom of the tripod region is a separate vacuum enclosure, called the trap can, which houses the Penning traps. Constructed from titanium and sealed off with indium and a copper pinch off tube, the trap can allows us to have an better

vacuum in the trapping region ($< 5 \times 10^{-17}$ torr in a similar apparatus at 4.2 K [62]) than in the IVC ($\approx 10^{-7}$ torr). This vacuum is achieved by pumping out the trap can at room temperature (to $\approx 10^{-7}$ torr), closing off the vacuum chamber (by pinching off the copper tube on the pump out port), and cooling down to 100 mK. Cryopumping of the remaining gases gives us the low vacuum necessary to have long particle lifetimes in the trap. The trap can's top flange (the pinbase) holds all of the electronics feedthroughs, as well as a microwave flange, a positron flange, a special 200 MHz feedthrough flange and one spare flange. It also acts as the ground for the experiment and a schematic of the pinbase layout is shown in figure 3.3. A schematic of the trap can is shown in figure 3.2

We must be very careful to avoid magnetic materials near the Penning traps. In addition to avoiding materials that are electronically paramagnetic, it has been observed that even the nuclear paramagnetism from many common trap materials (copper, macor, etc.) can cause magnetic field instabilities [12] due to slight temperature fluctuations around 100 mK. We limit the materials in the trap can region to those with low nuclear magnetic moments (silver, titanium, molybdenum and quartz), though there is still some unavoidable amount of copper in the pinbase feedthrough pins and in some electronic component connectors.

The experimental insert also contains a retractable positron source. This source has been described thoroughly elsewhere [58], and only a brief descrition will be provided here. A sealed ^{22}Na source is suspended by a nylon string that is coiled around a spool on rotatable vacuum feedthrough at room temperature. By rotating the spool, the positron source can be lifted or lowered through tubing within the

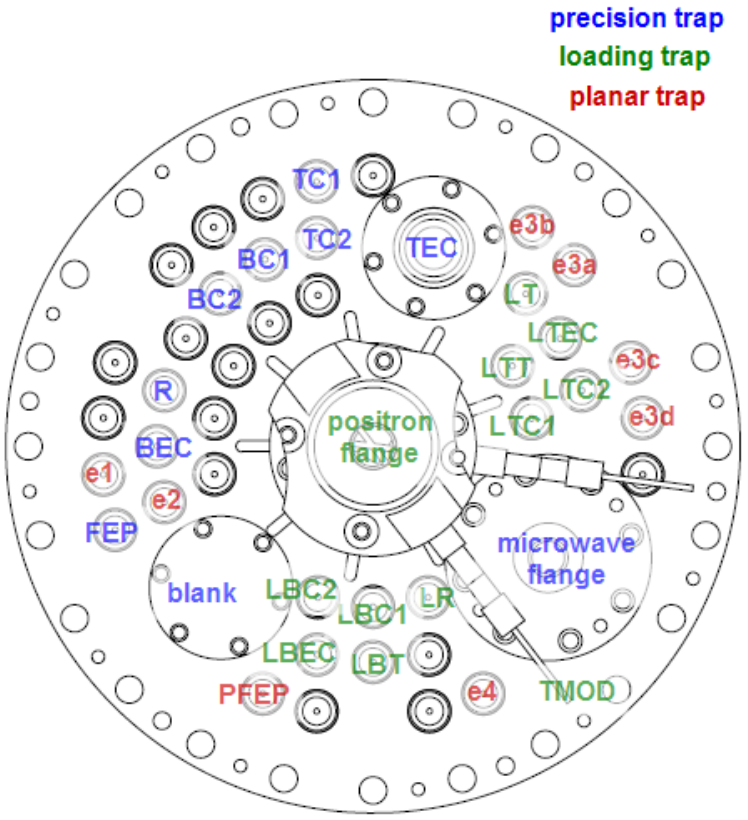

Figure 3.3: A schematic of the pinbase as viewed from the top, showing the location of every electrode connection, as well as the positron, microwave and 200 MHz feedthrough flange.

dilution refrigerator. The source can be positioned above the pinbase for loading (as described in chapter 5), or retracted to the mixing chamber or 4K plate for storage. Four sets of LEDs and photodiodes can read out the position of the source at these locations (two at the pinbase, one at the MC, and one at the 4K plate). As the source moves through the tripod region, it passes through a bend in the tubing, which cuts off the line of sight to the positron loading flange and discontinues loading.

To insert the dilution refrigerator and experiment into the helium space (see the next section for a discussion of the cryogen spaces), the experiment is surrounded by an aluminum and G10 tube that mates into an 8.57" sliding seal on the Dewar neck. By engaging the sliding seal and venting all of the rapidly boiling off helium through the dilution refrigerator, the experiment and refrigerator can be efficiently vapor cooled and set directly into the same liquid helium bath that surrounds the magnet, all without quenching the superconducting solenoid. The sliding seal o-ring is made from a teflon covered stainless steel spring. The advantage of this over traditional o-ring materials (viton, buna-n, etc.) is that the teflon ostensibly makes a good seal down to very low temperatures.

In practice, however, we have found that the seal slightly leaks when the G10 and aluminum tube is too cold. In addition, the lower portion of the IVC extends beyond the sliding seal (to mate into the magnet) and must be inserted into the helium space before the seal can be made. In order to avoid getting oxygen into the magnet and helium into the lab, we use a helium-filled glove bag (Spilfyter hands-in-bag 4-hand Chamber Model Number 690341) when inserting the experiment.

The typical procedure begins with the Dewar closed off and the dilution refrigera-

tor/experiment hanging from a crane. First, we exchange (in a glove bag) the Dewar top plate with a plexiglass plate. The plexiglass plate has no radiation baffles and allows us to look into the magnet bore to look for ice or other impediments. If the magnet bore is clear, we (once again in the glove bag) exchange the plexiglass plate for the experiment, lowering the experiment in enough to engage the sliding seal. Even with the sliding seal engaged, we leave the helium atmosphere in the glove bag until the experiment is fully inserted.

3.3 Cryogen spaces, Hold Times, and Stability

One of the major improvements of this apparatus over the previous apparatus is the support between the Penning trap and the magnet. For the 2008 measurement, the dilution refrigerator supporting the Penning trap hung from a nearly 2 meter structure relative to the magnet. In the new apparatus, however, the trap support is located directly on top of the superconducting magnet, with the radial alignment set by a pin that mates to a hole in the bottom plate of the magnet. See figure 3.4 for the layout.

In order for the experiment to rest on the magnet top, it must be decoupled from the Dewar top. Only a flexible bellows connects the hat of the dilution refrigerator to the Dewar top (see figure 3.4). This configuration alone would mean that pressure variations in the Dewar space would create variations in the upward force felt by dilution refrigerator, which could cause vibrations or other instabilities. To cancel these out, there is an additional upper bellows connected to the helium space.

Another benefit of the new apparatus is the size and number of the cryogen spaces.

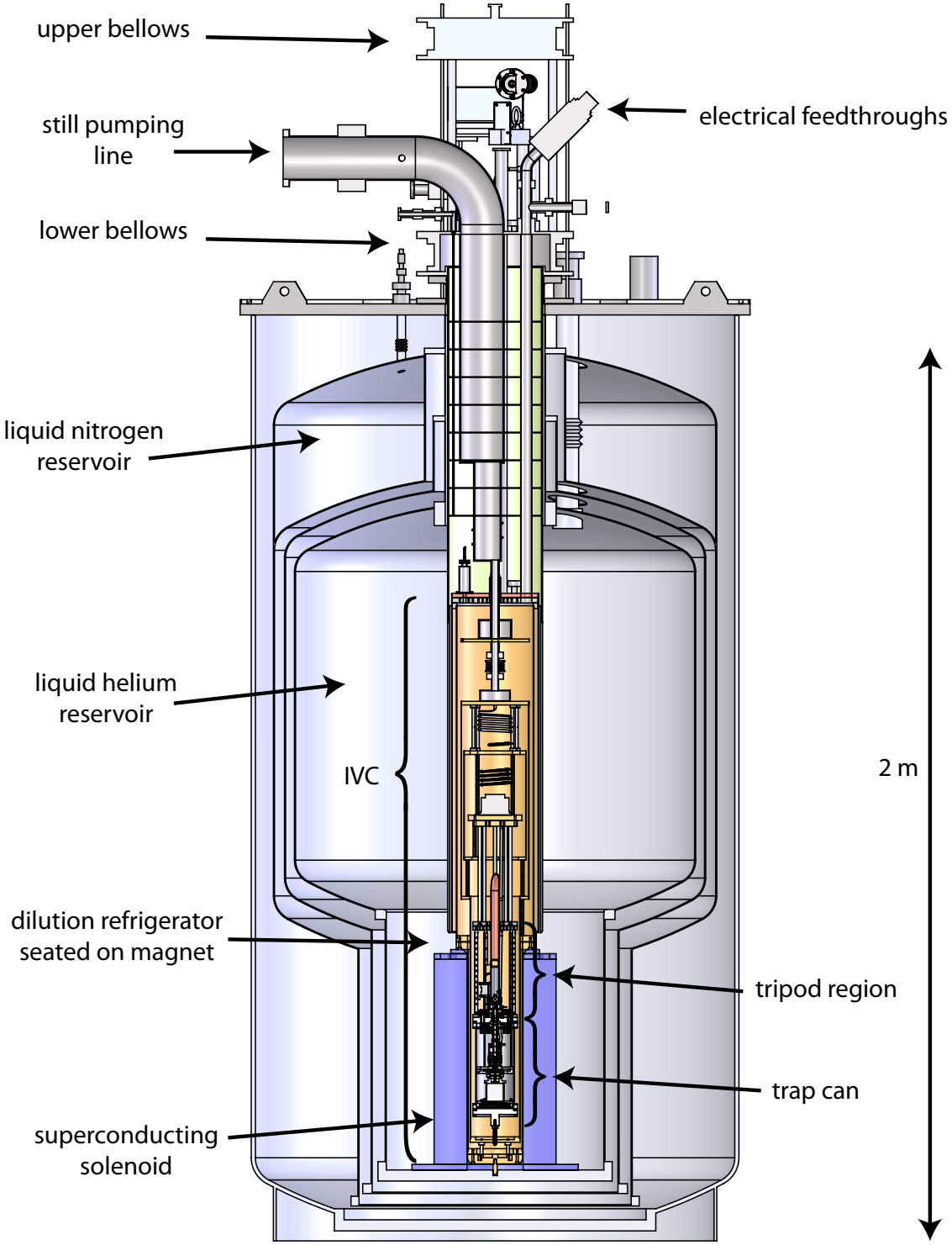

Figure 3.4: A schematic of the Dewar, magnet and dilution refrigerator showing several of the key features mentioned in the text.

In the previous version of the experiment, which evolved historically, the apparatus had 5 separate cryogen spaces. Each reservoir had to be filled on a different timescale, and each fill disrupted the stability of the system (see chapter 7), causing delays in data taking while the system settled. The new apparatus has only 2 cryogen spaces—one large reservoir for liquid helium and another for liquid nitrogen. This reduction in the number of cryogen spaces comes from combining experiment and magnet cryogen spaces. See figure 3.4 for the layout of the cryogen reserviors.

Each cryogen space is also much larger than in the previous experiment, reducing the number of fills even further. The liquid helium reservoir (ignoring the helium necessary to cover the superconducting magnet) can hold 500 liters, while the nitrogen Dewar space holds 190. Given the typical boil off with the dilution refrigerator running ($\approx$20 liters/day), this means that the helium space can go more than 3 weeks without having to be filled. This has been extended to almost indefinitely by the addition of a helium reliquifier (discussed below).

The nitrogen space was designed to have a hold time of 2 weeks. However, when the apparatus arrived, the nitrogen hold time was closer to 3.5 days. After some investigation, we found large sections of super insulation missing from the nitrogen Dewar space, allowing room temperatue radiation to be incident directly on the nitrogen space. By pulling apart the Dewar and adding more superinsulation, we have increased the hold time of the nitrogen space to over a week.

3.4 Helium Recovery System

Helium is a valuable resource. Currently, the main supply of helium comes from the United States government, whose stockpile has supported research and children's birthday parties for decades [63]. As the stockpile has dwindled, however, helium prices have increased [64], and with them, the uncertainty of the future of liquid helium based experiments. To offset these cost concerns, protect a valueable non-renewable resource, and increase the stability of our system, we have retrofitted a helium reliquifier into the existing apparatus. Given the size of our Dewar and its relatively high heat load (both from radiation and from conduction when the dilution refrigerator is inserted), we have chosen the current state of the art local helium reliquifier, which is a Cryomech PT415-RM Helium Reliquefier. The heart of the reliqfuier is a 2 stage pulse tube driven by a (model number CP1010) compressor that can provide 1.5 W of cooling power at 4.2 K.

The reliquifier is specified to be able to reliquify from 15 L of liquid helium per day from room temperature gas up to >27 L of liquid helium per day recondensing/reliquifying rate. In practice, this has turned out to be enough to reliquify all of our helium boil off, even with the dilution refrigerator running and the 1 K pot helium being recovered (see below).

The reliquifier must be carefully positioned and inserted into the helium Dewar to protect the fragile vacuum transfer line (stinger). The apparatus necessary to insert the reliquifier is custom and begins with a plate that is carefully mounted on a beam above helium Dewar. The plate is aligned with a plumb bob such that the stinger of the reliquifier will line up with a sliding seal into the helium Dewar space (within

1/8"). Once mounted, the reliquifier hangs from a custom made birdcage mount (see Figure 3.5c). The stinger is lowered until it's just over the sliding seal, at which point the sliding seal is uncapped in the stinger is slowly inserted (see Figure 3.5b). The reliquifier is then slowly lowered, with the stinger guiding the reliquifier into the Dewar. It is advisable to keep one hand on the mount and one hand on the stinger to make certain that they are moving at the same rate, while another person slowly lowers the crane.

Before the reliquifier can be inserted into the helium space, it must be purged of the air inside the cold head and stinger space. This can be done via the external valves that we have added to the reliquifier, by simply closing off the exhaust valve (see Figure 3.6) and flowing the purge gas through the purge valve. Typically we flow nitrogen initially for about 30 minutes followed by about 30 minutes of helium purging. The helium can continue to flow until the stinger is inserted into the helium Dewar space, which ensures that air does not flow in and freeze in the narrow channel of the stinger.

The reliquifier is then lowered onto a custom stand that has been mounted on the Dewar top (see Figure 3.5c). The stand has been designed such that the reliquifier can be bolted down to secure the reliquifier and protect the stinger. The stand also sets the final vertical position of the reliquifier, and has been chosen to keep the length of the stinger outside of the dewar to (much) less than 1 inch (see Figure 3.5d).

The reliquifier is connected to a remote motor via a 3 foot long, high pressure helium line, which was purchased to decouple vibrations from the Dewar top. The compressor and remote motor are connected through two 75 foot long stainless steel

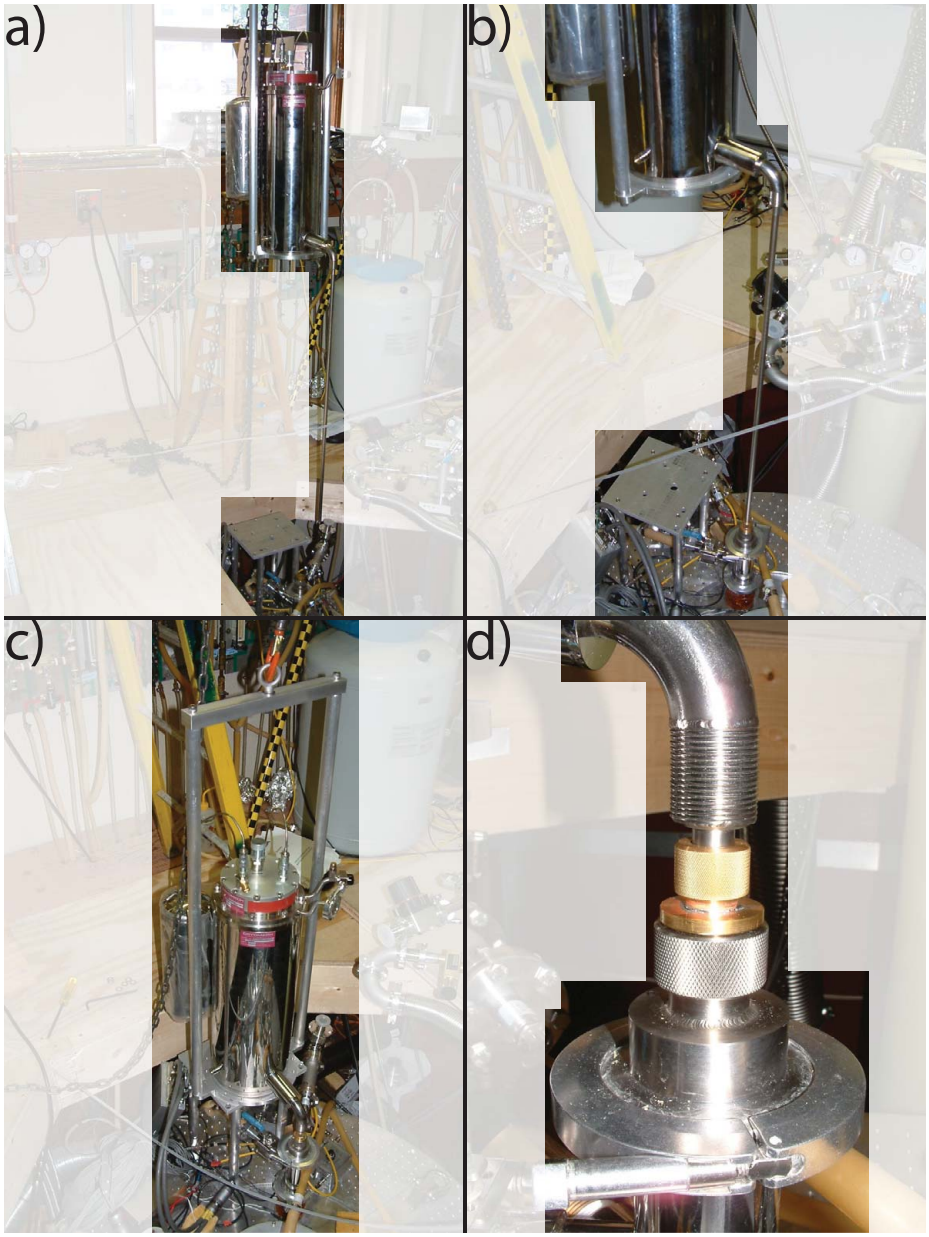

Figure 3.5: a) The helium reliquifier is hanging from a crane, carefully positioned such that the stinger lines up over the sliding seal into the helium Dewar b) The reliquifier is lowered so that the stinger is engaged in the sliding seal c) The reliquifier is lowered until it sits on a custom stand and is bolted down d) A view of the stinger and the sliding seal after the reliquifier has been inserted. The exposed stinger should be $\ll$1 inch.

lines, which isolate the compressor (stored in a separate room with cooling water and power) from the Dewar top. The noisy electrical ground from the compressor is kept from the experiment by electrical breaks in both the 75 foot lines and through an electrical break on the line connecting the remote motor and the reliquifier.

The Dewar's helium exhaust is fed into the input of the reliquifier. By allowing the helium vapor to exhaust out of Dewar in the usual configuration, we are still able to take advantage of any vapor cooling that occurs as the helium leaves the Dewar. See Figure 3.6 for a schematic of the helium exhaust recovery. Once the compressor is started, the cold head typically cools down from room temperature to below 4.2 K (where we start reliquifying helium) within a few hours. We monitor the temperature of the cold head with a silicon diode temperature sensor, read out by a Scientific Instruments Model 9700 temperature controller. The controller also controls the power applied to a 50 V, 50 W, 50Ω heater on the cold head. This heater is useful for controlling the reliquification rate and for heating up the cold head quickly when we would like to pull out the reliquifier.

When the helium space is sealed off from exhausting to the outside world, the system is effectively closed. Thus, by controlling the heat that we put into the cold head heater, we are able to control the pressure in the Dewar/exhaust/reliquifier system. By regularly measuring the pressure and feeding back this information to the heater on the cold head, we are able to stabilize the pressure in the system to the level of a few mpsi. This level of pressure regulation is comparable to the previous version of the experiment [13] and should keep the magnetic field from the solenoid similarly stable (see chapter 7). This pressure control loop, including its safeguards,

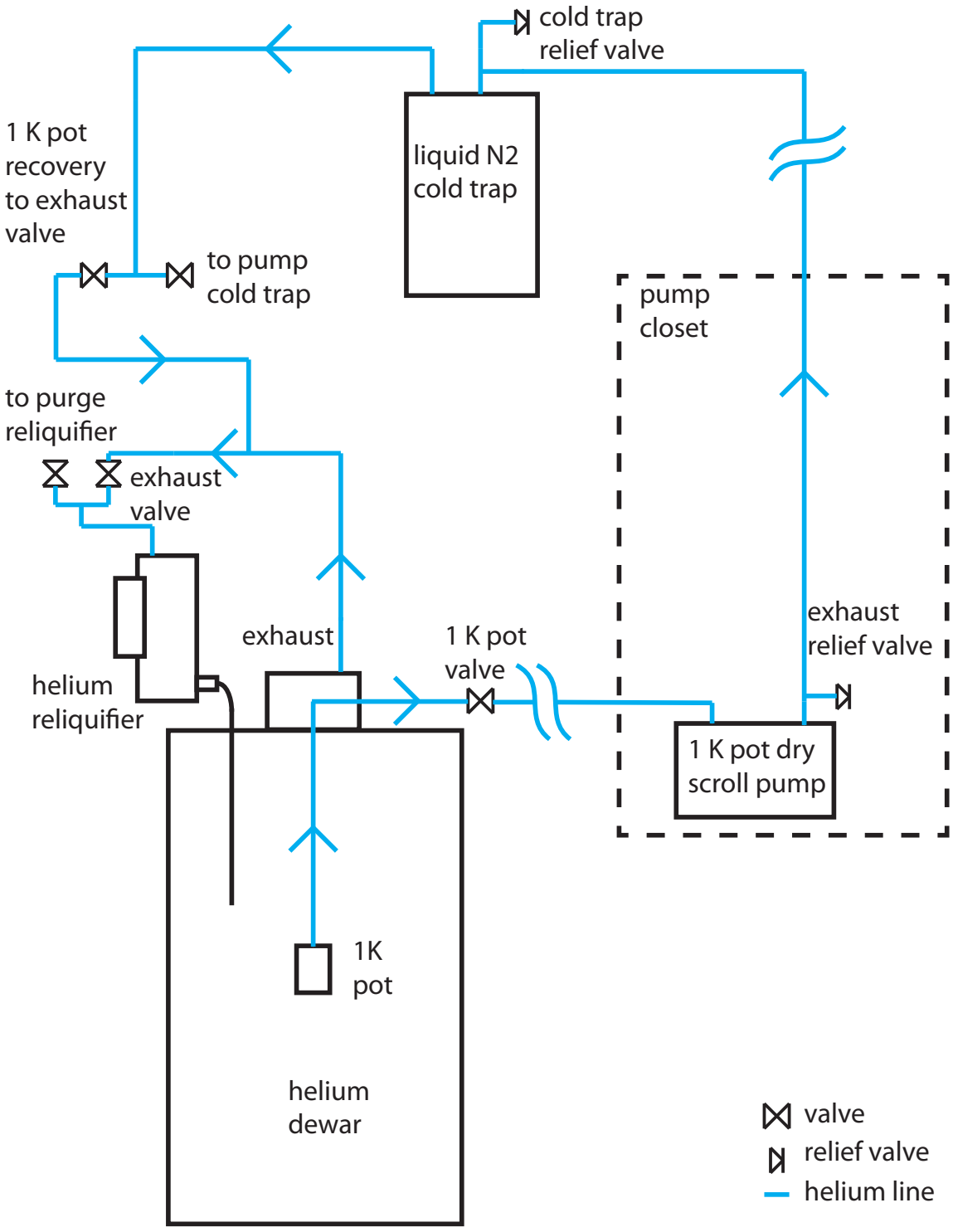

Figure 3.6: Schematic of the helium recovery system, including the 1 K pot helium recovery. The arrows indicate the direction of helium flow.

will be written up more completely in a future thesis [65].

When the dilution refrigerator is running, there is an additional source of helium loss—the 1 K pot. In order to keep the 1 K pot cold, we must continually pump on and evaporate helium from it. To recover this helium, we have replaced the 1 K pot pump with a large dry scroll pump (Edwards XDS35i) and fed its exhaust through a custom nitrogen cold trap (which shares a low loss nitrogen Dewar with the ^3He-^4He mixture cold trap) and then back into the exhaust of the Dewar. Extra valves have been added so that the cold trap can be isolated from the helium Dewar exhaust and pumped out with a separate pump (See Figure 3.6), which can be used to clean out the cold trap upon warm up.

With this addition, the helium system is truly closed, and we have run without seeing any helium loss for weeks. See figure 3.7 for an example of the helium level before and after the reliquifier is turned on. If the reliquifier never shut down and the experiment never needed to be cycled, the hold time of our helium space would essentially be indefinite. In practice however, we have been limited by experimental cycling. While we are lowering in the experiment from room temperature, the helium boiloff rate is much too high for the reliquifier to handle (typically about 50 liters of liquid helium over 3 hours).

We have also found that, on a slow timescale (typically $\approx$ months), the reliquifier stinger can clog up. We believe that the culprit is the stinger clogging with nitrogen ice (which may be entering through the latex tubing connecting the exhaust to the reliquifier). When this happens, the cold head remains $<$4.2 K, but the reliquifier no longer keeps up with the boil off of the Dewar. If we heat up the cold head, we find

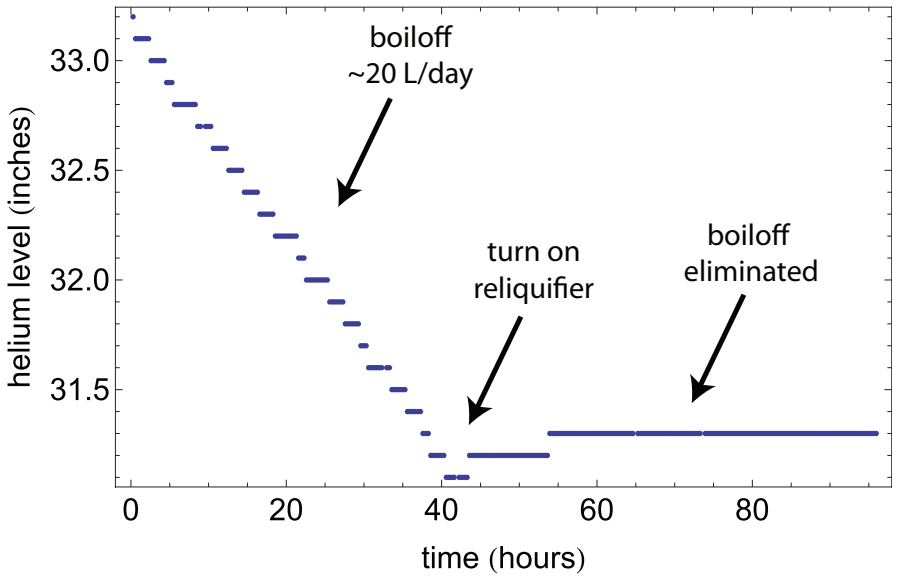

Figure 3.7: The level of the helium in the experiment with the reliquifier off and on. Note that the boiloff number is when the dilution refrigerator is inserted into the Dewar.

that the temperature increases to nearly 4.2 K, remains level for quite some time (as the pressure relief valve on the reliquifier goes off) and then continues to increase, which is consistent with the stinger being clogged and liquid helium building up around the cold head. We have found that the rate of clogging increases (sometimes to immediately) if we warm up the cold head well above 4.2 K. Presumably this is because the cold head is acting as a cold trap for nitrogen or other gases, which are then dumped into the stinger as the cold head warms up.

We have shown that the reliquifier can drastically reduce boiloff and increase the helium hold time, which saves money and could increase stability, since filling the helium space disrupts the experiment. There is some chance, however, that the vibrations from the reliquifier and remote motor could couple into the experiment. How these vibrations could couple into the experiment is a complex problem, which

we are not eager to understand. Instead, it would be nice to rid ourselves of the vibrations caused by the reliquifier. The vibrations at the remote motor, the reliqifier and Dewar top have been measured, with the reliquifier on and off, and plans to introduce a significant damping system are already underway.

Chapter 4

Low-Temperature Nuclear Magnetic Resonance

The ideal Penning trap is the superposition of a uniform magnetic field and an electrostatic quadrupole, as discussed in chapter 2. Our quadrupole is approximated by carefully biasing trap electrodes of the appropriate geometry. Our homogeneous magnetic field is approximated by a superconducting solenoid with a main coil and several shim coils (detailed in chapter 3). This chapter will disuss the methods we use to measure the field produced by these coils and how to make the field more uniform (or "shim" the magnet).

In the new apparatus, the bore of the superconducting magnet must remain at 4.2 K (or at least below the superconducting temperature of niobium titanium, $\approx$ 7K in our magnetic field) while the magnet is energized. The experiment helium space and the magnet helium space are shared, which allows us to set the experiment directly on the top of the magnet. Although this design choice may have significant improvements

in stability over the old apparatus (see chapter 3), it has provided new challenges for measuring and shimming the magnetic field prior to inserting the experiment.

The 2008 electron g-factor measurement was made in a magnet whose bore could be warmed up, which allowed for room temperature measurements and shimming of the magnetic field with a water nuclear manetic resonance (NMR) probe. This chapter will discuss the extension of our NMR techniques into the low-temperature realm, with the focus on the design and implementation of a new ^{3}He probe used to measure and shim magnetic fields at 4.2 K. The unusual feature of this probe is that the ^{3}He is gaseous at 4.2 K.

4.1 A Brief Introduction to Pulsed Fourier Transform NMR

There is more than one way to shim a magnet using NMR [66, 67, 68, 69], but our technique focuses on pulsed Fourier transform spectroscopy. In this technique, we begin with a collection of nuclear spins in a homogeneous (or nearly homogenous, as we'll see below) magnetic field. Here, the uniform magnetic field, $\vec{B} = B_z\hat{z}$, defines the direction of the z-axis. We then apply a short, pulsed radio frequency (RF) oscillating magnetic field near the Larmor frequency of a nuclear spin, but in a direction orthogonal to the static field (in the x-y plane). If the drive frequency is close enough to the precession frequency, the pulse tilts the spins away from the direction of the uniform field and into the x-y plane. After applying the RF drive pulse, the newly tilted magnetization vector then precesses in the x-y plane (since the

spins precess around the static field along the z-axis), which can be measured with an RF pickup coil (often, as in our probes, the same coil as the drive coil).

The precession in the x-y plane, which is called a free induction decay (FID), decays with several well known time scales. The most energetically favorable equilibrium position is for the spins to align with the homogeneous magnetic field. Thus, the spins will eventually line back up along the z-direction, on a timescale called the longitudinal relaxation time (or T_1 for short). Another useful timescale, called the transverse relaxation time (or T_2 for short), measures the timescale on which the transverse signal decays. Though these timescales naively might sound as though they should be the same (and in some limits, they can be), T_2 is often shorter than T_1 due to dephasing of the spins. The source of the dephasing can sometimes be complex interactions between the spins (which is why T_2 is often called the spin-spin relaxation time), but in one simple case, can be due to inhomogeneities in the applied magnetic field. In the limit that the transverse signal decay is dominated by external magnetic field inhomogeneities, the timescale for decay is called T_2^*. This decay mechanism is distinguished from T_2, because the process is not truly random, but rather is a position dependent dephasing (for stationary spins). The signal in the x-y plane could be recovered, for example, by a spin echo measurement [70].

Once an FID has been measured, we can then extract useful information about the static magnetic field. The fast oscillation frequency (usually determined by taking the Fourier transform of the FID), plus the knowledge of the magnetic moment of the nuclear species of interest, determines the value of the static magnetic field. In addition, we can also extract the decay time of the FID (which translates into the

width of the Fourier transform peak). In the limit that the applied magnetic field is the dominant source of dephasing, this width determines the field inhomogeneity over the sample volume.

The ring down frequency and timescale provide us with the mechanisms to measure and shim a magnetic field via two methods. In the first method, a small sample can be used to measure the magnetic field at several distinct locations within a magnet. The magnetic field profile can then be adjusted until at each point reads the same value. The other method, typically used as a second step, places a larger sample volume over the region of interest to be shimmed, and uses the width of the Fourier transform of the FID as a measure of field homogeneity. By adjusting the magnetic field profile, the ring down time can be monitored and maximized, thus, maximizing the homogeneity.

4.2 Room-temperature NMR

For the 2008 g-factor measurement, the magnetic field was shimmed with both techniques. The initial shimming was carried out by moving a small water sample axially. Finally, a 1 cm diameter sample was used to maximize the ring down time of an FID. For similar magnets, we have previously shown that the magnetic field can be shimmed to a part in 10^8 over a 1 cm diameter sphere, as in figure 4.1. This shimming data comes from a magnet used for antiproton mass measurements in [71]. Data from the magnet used for the 2008 g-factor measurement will be discussed below.

Since water NMR has proved a fast and efficient method for shimming magnetic fields, it is worthwhile to consider some of the characteristics of the water NMR that

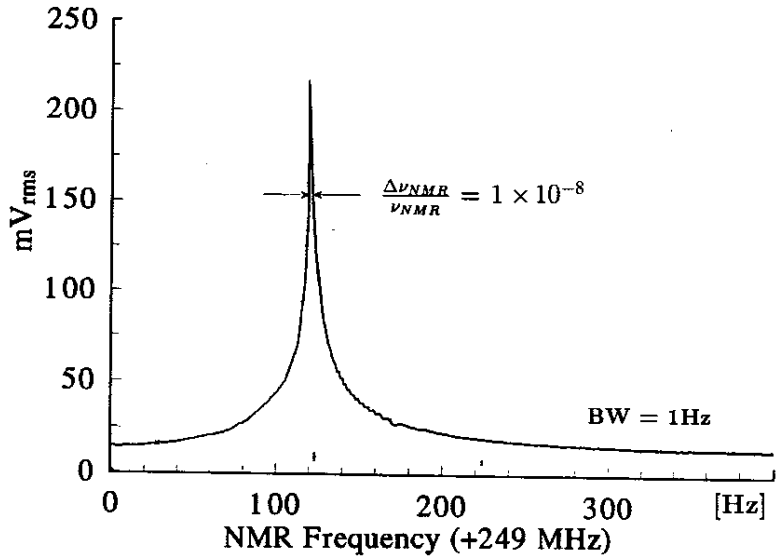

Figure 4.1: An example of a water NMR signal from a well-shimmed magnet taken from [71]

will motivate the design of a low-temperature NMR probe. Firstly, water in its liquid form at room temperature has a fairly long T_2 time [72], which means that when the magnetic field homogeneity is tuned, the FID has a narrow resonance. This allows for both an accurate determination of the absolute value of the field, as well as the possibility of measuring a very homogeneous field (since the transverse decay time will not be dominated by T_2 at low field homogeneities).

Secondly, we are easily able to measure the FID from a 1 cm diameter water sample. We would like to have a comparable signal size from our low-temperature NMR setup. Since the drive and detections electronics will be similar, it is mainly the size of the magnetization vector from the sample that will determine the signal size. For water at room temperature ($\approx$ 300 K) in a 1 cm diameter spherical sample volume (0.530 cm^3) in a 5.3 T magnetic field, the magnetization of a macroscopic

water sample will follow the typical magnetization of a 2 state paramagnet (see, for example, equation 3.32 in [73]):

$$M = N\mu \tanh \frac{\mu B}{k_B T} \tag{4.1}$$

where M is the magnetization, N is the number of spins, μ is the magnetic moment of each spin, k_B is the Boltzmann constant and T is the temperature. For the conditions listed above, we would expect our sample volume to have a magnetization of $M_{watersample} = 9.0 \times 10^{-9}$ A/m. For our low-temperature NMR probe, we have strived to match this magnetization (as discussed below).

4.3 Low-temperature NMR

Though water is ideal for our room-temperature NMR, it is a poor candidate for measuring and shimming the magnetic field to the same degree of precision in the 4.2 K bore. Though liquid water at room temperature has a long T_2 time, the interactions in water ice decrease T_2 and broaden the resonance [72], make the absolute value of the field and the field homogeneity difficult to determine as accurately. A water sample presents other practical problems. For example, having a spherical sample of water enclosed by pyrex glass (our typical sample containment material), which freezes and thaws regularly, could thermally stress and crack the glass. A much better candidate would be a substance that remains liquid at 4.2 K. Of course, ^{4}He is liquid at 4.2 K, but unfortunately has no magnetic moment.

The alternative presented here is to use a gaseous ^{3}He sample. ^{3}He is gaseous at 4K (it liquifies at 3.2K at 1 atmosphere of pressure) and has a magnetic moment

(which is about 76% that of a proton water) [74]. The challenge, of course, is that there are typically far fewer spins in a gas compared to a liquid, and the FID is proportional to the number of spins.

A naive approach might be to fill up a spherical sample volume with ^{3}He, as we typically have done with water. Looking at equation 4.1 for the ideal paramagnet, we see that there are two competing factors for the size of the magnetization vector associated with the sample. On the one hand, the density of spins in a gaseous sample is severely reduced. On the other hand, the lower temperature means there will be a much larger polarization of the spins.

It turns out that, if we were to follow the same procedure as the water NMR (simply filling a 1 cm diameter pyrex sphere with one atmosphere of ^{3}He at room-temperature), we would decrease the signal size by nearly 2 orders of magnitude, which would be difficult to detect using our previous methods. However, if we could use the same spherical sample volume at 4.2 K, but keep the pressure at nearly 1 atmosphere, we would recover nearly the same magnetization vector as the water sample, and therefore, nearly the same signal size.

In order to achieve a 4.2 K sample of ^{3}He with 1 atmosphere of pressure, we could drastically over-pressurize the sample at room-temperature. This would be inadvisable for multiple reasons. Firstly, the pressure in the pyrex sample volume would present a serious shatter hazard. Secondly, the high pressure ^{3}He gas would leak out of the seals and diffuse out of the glass at a faster rate, which would not be desirable due to the high cost of ^{3}He ($450 per STP liter in 2009).

A better alternative is to link the small 4.2 K sample volume to a large ^{3}He

reservoir at room temperature. We can then fill both the reservoir and sample volume with 1 atmosphere of ^{3}He at room temperature. As the sample volume is cooled down, ^{3}He will cryopump into the cold volume, increasing the density of spins. As long as the reservoir is large enough, the pressure will remain at nearly 1 atmosphere, and the magnetization vector will be similar to the water sample. We were surprised after developing our He3 NMR probe, when a literature search for related room temperature probes turned up the suggestion that the room temperature probe being reported could possibly be adapted for low temperature operation, much as we had done [75].

From a signal standpoint, ^{3}He is an ideal candidate for our low-temperature NMR. However, it is worth mentioning a few of the concerns for using ^{3}He. Firstly, the cost of ^{3}He is very high (several hundred dollars per liter at standard temperature and pressure (STP)) compared to distilled water, which could be prohibitive. However, as we'll see in the next section, the amount needed for a ^{3}He probe is small ($\approx$ 1 liter STP) and can be stored within the apparatus. Perhaps more of a concern is that ^{3}He has applications in homeland security [76] as a neutron detector. After the conception and construction of the probe described below, ^{3}He has become a regulated substance by the government. Currently, ^{3}He is still available to universities for research purposes, but the future status is unknown.

Finally, ^{3}He experiments have sometimes demonstrated extremely long T_1 times [77] (and sometimes as long as $>$ 1 hour in a cryogenic experiment [78] and $>$ 74 hours for a polarized sample at room temperature [79]). For comparison, protons in water typically have a T_1 of a few seconds [72, 80]. Though this would not be a

problem in principle, in practice, too long of a T_1 time could limit the duty cycle of the experiment, which could slow down shimming or make an initial NMR resonance at a new field difficult to find. We can partially avoid this constraint by tipping only a small fraction of the spins, which allows us to repeat the measurement several times without drastically depleting the longitudinal magnetization vector.

Still, we can see the effects of a long T_1 time in our apparatus. If we repeatedly measure a signal too quickly, we notice that the size of the FID (as measured by the initial amplitude of the voltage oscillations) slowly begins to decrease, but rebounds if we wait long enough in between measurements. Though we do not actually have enough power to measure T_1 in the usual manner (inversion recovery), we can still make a measurement of T_1 in our system.

By applying so many RF pulses so as to completely deplete the magnetization vector in the z direction (as measured by the peak amplitude of the FID in response to another RF pulse), we can then measure the timescale on which the axial magnetization recovers (again measured by the FID). The recovery follows equation 4.2, and we can fit this to measure T_1. We further check that this number is independent of the number of scrambling pulses. The T_1 time in our system is 42.6 ± 4.2 seconds, where the error bar comes from the standard deviation of all of fits. Though this is still much longer than the water probe, in practice, this timescale has not been prohibitive for shimming our magnet.

$$M_z(t) = M_{z,\mathrm{eq}}\left(1 - e^{-t/T_1}\right) \tag{4.2}$$

4.4 The ^{3}He Probe

Following the two volume approach, the apparatus consists of a 1 liter, room temperature reservoir connected through a thin capillary to a 1 cm diameter spherical pyrex sample volume at 4.2 K. The spherical pyrex bulb is located near the center of our superconducting magnet. The room temperature reservoir is made of standard 3" diameter capped copper piping. The upper half of the capillary is a thin-walled, stainless steel tube while the lower half is OFE copper (to minimize magnetic materials near the magnet field center). A copper flange is soldered onto the bottom of the copper capillary. The pyrex sphere was purchased from Wilmad Labglass (in order to use low iron content pyrex), and joined to an OFE copper capillary via a glass to metal seal made by Larson Electronic Glass. In order to keep the impurity content low, we must provide Larson with low iron content pyrex with which to make the glass to metal seal. The OFE copper tube coming from the pyrex sphere is soldered into a copper flange and makes an indium seal with the flange on the copper capillary. These flanges allow the sample volume to be easily exchanged. Figure 4.2 shows the relevant 4.2 K portion of the apparatus.

The system is initially filled to a pressure of 1 atmosphere with ^{3}He with the entire apparatus at room temperature. As the sample volume is cooled down, the number of spins increases in the sample volume, while only slightly decreasing the pressure of the system. For a 1 liter reservoir at room temperature and a 0.53 cm^3 volume at 4.2 K, this leads to a helium density increase of over 63 times over system with no room temperature reservoir. Though the polarization of the sample in our 5.2 T magnetic field is only about 0.096%, the density increase leads to a magnetization of

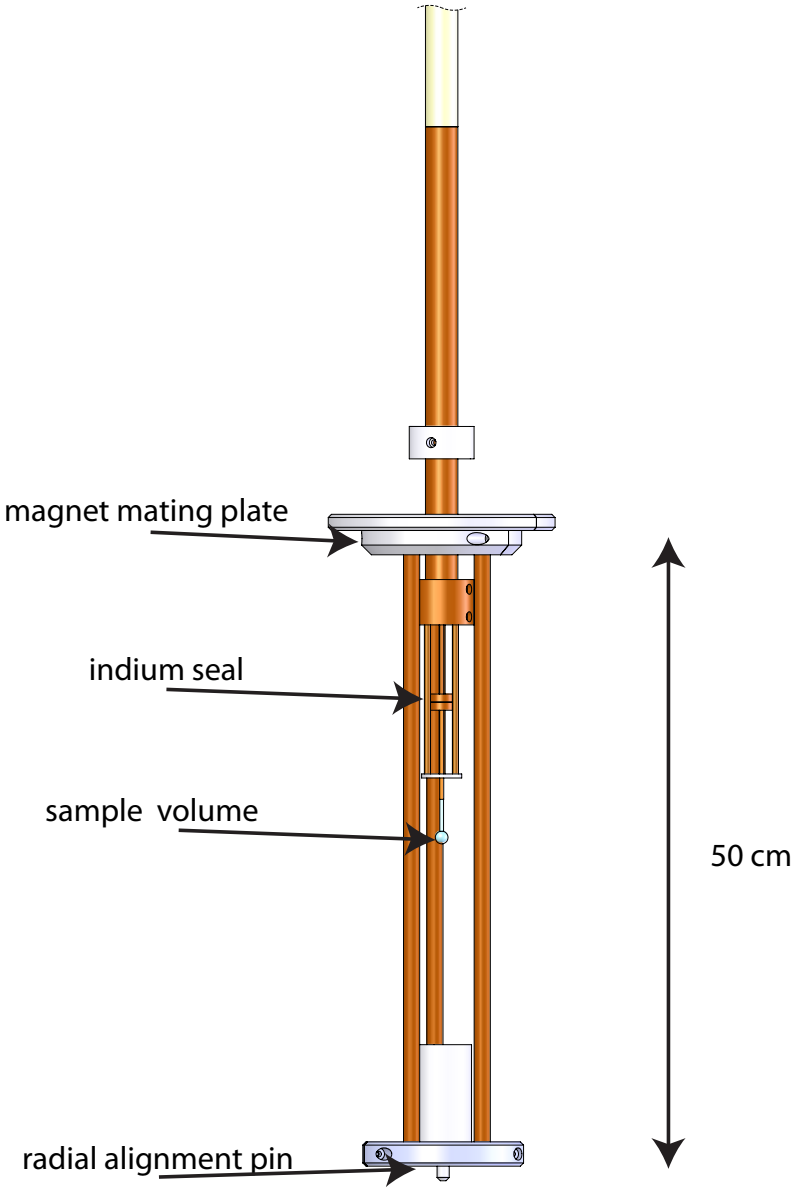

Figure 4.2: A schematic of the 4.2 K section of the ^{3}He probe.

$\approx 9 \times 10^{-9} \frac{A}{m}$, which, by design, is comparable to that of the room temperature water sample with the same volume.

By adding a valve at room temperature, the 1 liter reservoir also doubles as a storage container for the helium when the magnetometer is not in use. By cryopumping (submerging into liquid nitrogen) the ^{3}He into the reservoir, more than 99% of the helium can be stored in the copper reservoir, which reduces diffusion losses through the glass portion of the apparatus. This also allows the sample volume to be exchanged (with an indium seal) with minimal ^{3}He loss.

The body of the apparatus is compatible with both the new ≈5" bore magnet for the positron/electron g-factore measurements, as well as with the bucket Dewar that fits into the previous generation of Nalorac magnets. In its stripped down form, the probe can slide into a bucket Dewar with an adapter that seals between the top plate of the apparatus and the top of the magnet bore. To put the probe into the new system, aluminum exentions are added on. These extensions increase the size of the radiation baffles to reduce the radiative heat load while in the larger opening to the helium space of the new system. More importantly, a precisely machined aluminum extension also attaches onto the lower portion of the apparatus. This allows the probe region to mate securely onto the top of the new magnet, for alignment and stability.

Inserting the ^{3}He probe into the magnet is done in the same manner as inserting the experiment (by mating to the same sliding seal). While venting only through a port on the top plate of the probe, the entire lower portion of the apparatus is vapor cooled, plunged into the liquid helium bath and set on top of the magnet. The thermal mass of the probe is much lower than that of the dilution refrigerator, so it

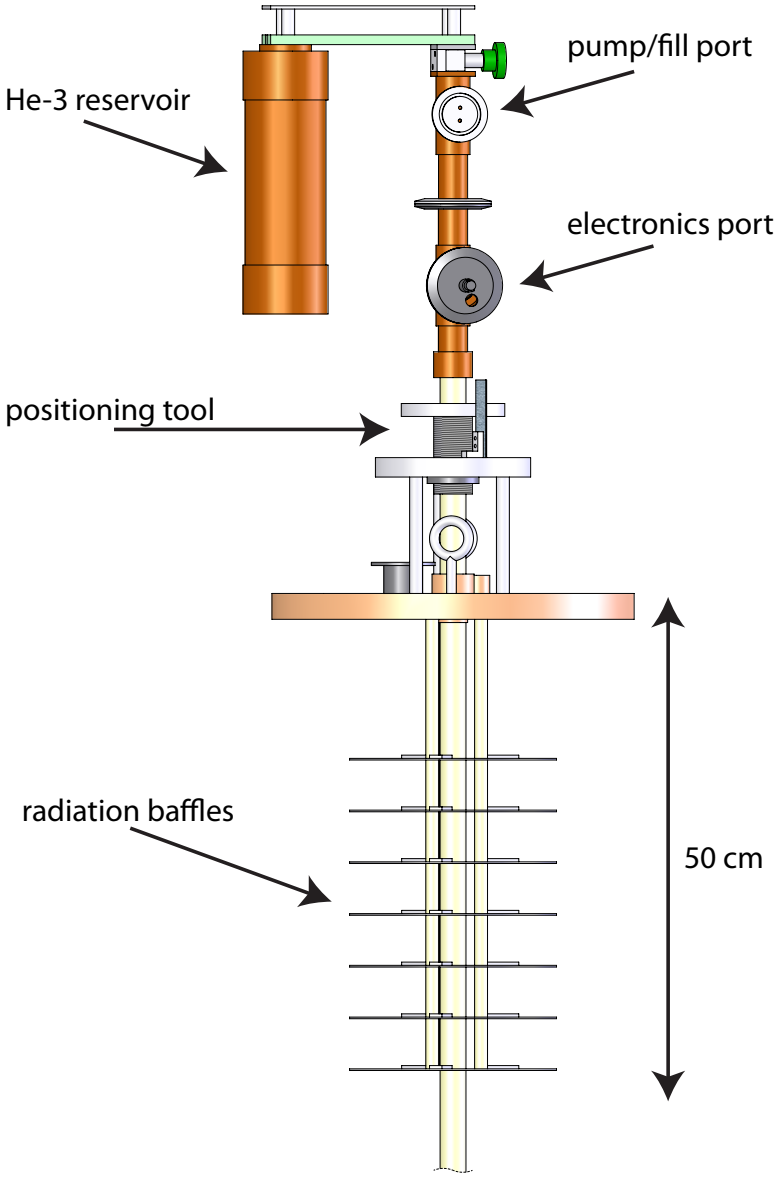

Figure 4.3: A schematic of the upper section of the ^{3}He probe.

can be plunged in far more quickly (typically $<$ 1hour as compared to 3-4 hours for the experiment) with less helium loss.

The sample volume is radially aligned in our magnet by an assembly that surrounds it. The lower portion has a pin which mates to the bottom of the magnet, and the upper portion has a plate that fits into the magnet bore. These can be seen in figure 4.2. The aluminum assembly mates concentrically with a nylon tube that, in turn, mates concentrically with a centering ring on the copper capillary. Note that the nylon tube is not shown in figure 4.2 in order to show the pyrex sample volume. The axial positioning of the sample is adjusted at room temperature. A 1 1/2" diameter, 28 threads per inch positioning tool allows the sample to be located axially to sub-millimeter precision over a 2.5" range around the center of the magnet. This can be seen in figure 4.3.

The drive and detection electronics are shown in figure 4.4. A radio frequency drive is generated from a Programmed Test Sources (PTS) 250. A timing pulse closes two normally open switches and passes the signal into a power amplifier. The power amplifier boosts the signal while another timing pulse closes a switch between the drive and the probe coil through a SPDT switch. After the drive pulse is complete, a third timing pulse closes a switch between the coil and the detection chain. The NMR signal passes through two low noise amplifiers and a band pass filter, before being mixed down with the initial radio frequency signal. The signal is mixed into the audio regime where it is detected via a National Instruments data acquisition card adapter and recorded on the computer.

In order to get good power transfer into the probe coil, the impedance of the

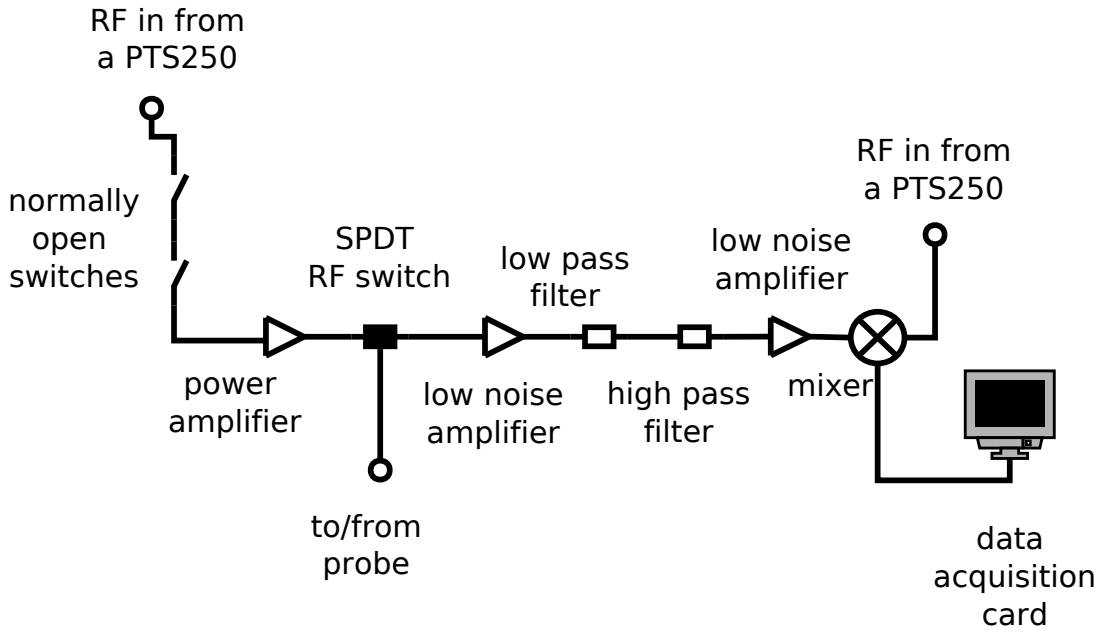

Figure 4.4: The NMR drive and detection schematic used for the ^{3}He probe.

coil must be well matched to the source. To accomplish this, we have used the standard NMR matching circuit shown in figure 4.5. The matching circuit makes use of both a matching and a tuning capacitor. For our initial design, we used a fixed matching capacitor and a variable capacitance diode (varactor) for the tuning capacitor. In practice, however, the detection has worked reasonably well by tuning the matching circuit at room temperature, and the varactor was later removed due to its magnetism and its limited tuning range at low temperature. The capacitors are now both American Technical Ceramics (ATC) capacitors and the coil is hand wound from high purity OFE copper, to minimize magnetism.

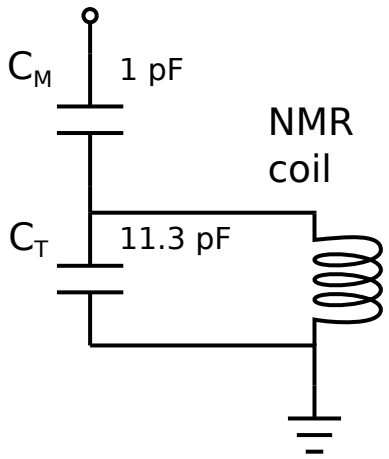

Figure 4.5: Matching circuit for the NMR coil. Typical values of C_M and C_T are shown, though C_T must be adjusted for each coil.

4.5 Magnetic Field Measurements and Shimming

With the above apparatus, we are able to measure NMR from 4.2 K gaseous ^{3}He. To test the probe and the shim coils in the new magnet, we measured the magnetic field shift for the Z and Z^2 shim coils. Figures 4.6 and 4.7 show the magnetic field shifts created by the Z and Z^2 shim coils for $\pm$ 1 amp relative to the uncharged coils. These values are consistent with the shim coil design specs.

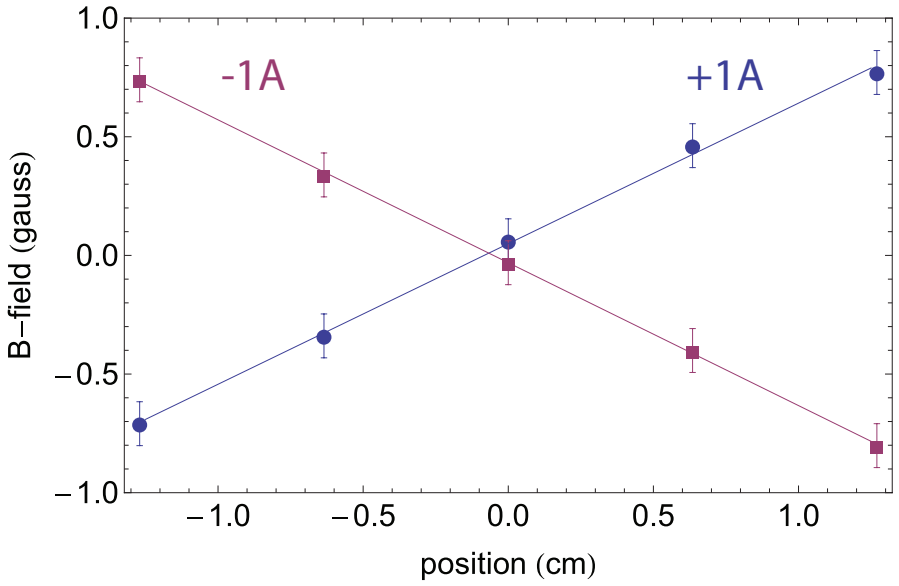

Figure 4.6: The magnetic field profile of the Z-shim at $\pm$ 1 A, as measured by the ^{3}He probe. The position axis is centered around the expected center of the field based on the probe dimensions.

Once we have mapped out the Z-shim magnetic field profile, we can use the information to determine the center of the magnetic field. This occurs where the Z-shim coil crosses zero (i.e. where the fully energized Z-shim doesn't shift the magnetic field from the unenergized value). Using the expected dimensions of the ^{3}He probe, we can also confirm that this occurs at the expected location relative to the probe

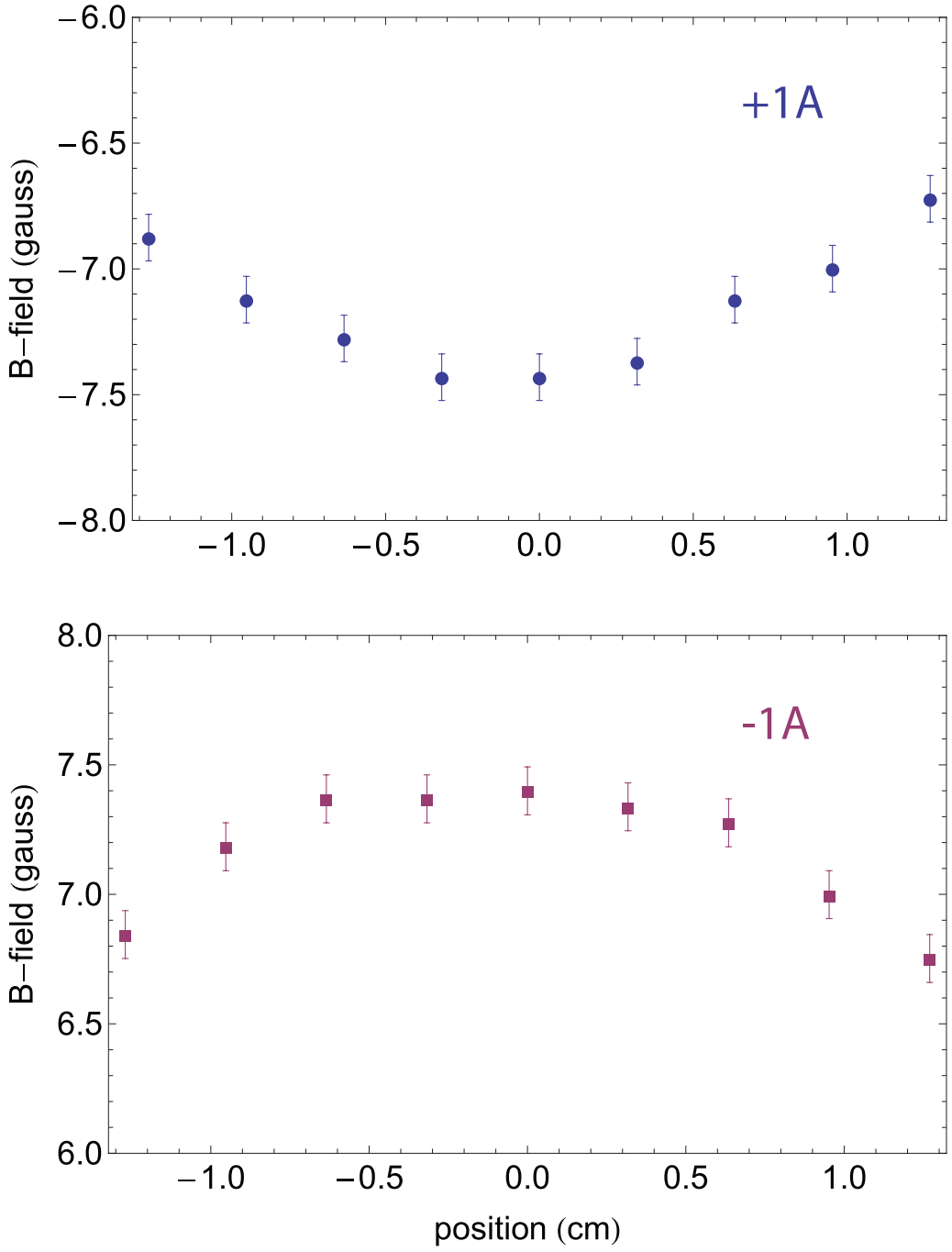

Figure 4.7: The magnetic field profile of the Z^2-shim at $\pm$ 1 A, as measured by the ^{3}He probe. The position axis is centered around the expected center of the field based on the probe dimensions. Notice that the Z^2 shim also adds a substantial offset to the homogeneous magnetic field.

dimensions. The center is found to be within 1/8" of where it was expected, which is close to the limit of how accurately the probe length has been determined.

After these initial measurements, we can locate our 1 cm diameter spherical volume at the center of the magnet and attempt to shim the magnet. At this phase, T_2^* is our primary handle for determining the homogeneity of the magnetic field. We begin by measuring an FID and looking at the decay envelope (or width of the FFT). The process of shimming then involves choosing a shim coil and adjusting its current. Then we measure another FID and check to see if the field homogeneity has been improved. Initially, several field coils may appear to have no effect on T_2^*. This is typically because one gradient is dominating the field inhomogeneity and the other coils cannot be set until the limiting gradient is removed. In this fashion, all of the shim coils are set to maximize T_2^*. The process is iterative, and each shim coil is adjusted several times before a suitable current in all coils is found.

The left column of figure 4.8 shows an example of an FID after shimming the new magnet with the ^{3}He probe. The figure shows the full time trace of an FID (top), the first few ms of the FID to show the fast oscillations (middle) and the Fourier transform of the data (bottom). Note that the full width half maximum (FWHM) of this data is 11.5 Hz, which corresponds to a field homogeneity over 1 cm diameter sphere of 68 ppb.

As shown above, measurements in previous magnets have demonstrated field homogeneities of a part in 10^8 over 1 cm diameter sphere. However, if we compare to the recent shimming data used for the 2008 g-factor measurement, as shown in the right column of figure 4.8, we actually see that the FID is longer our the new magnet, and

the field is actually better shimmed over the 1 cm diameter sphere. It is not clear why our shimming should be able to produce a more homogeneous magnetic field, but this is our first confirmation that the new magnet and shims can make a homogeneous enough field for a g-factor measurement comparable to the 2008 measurement.

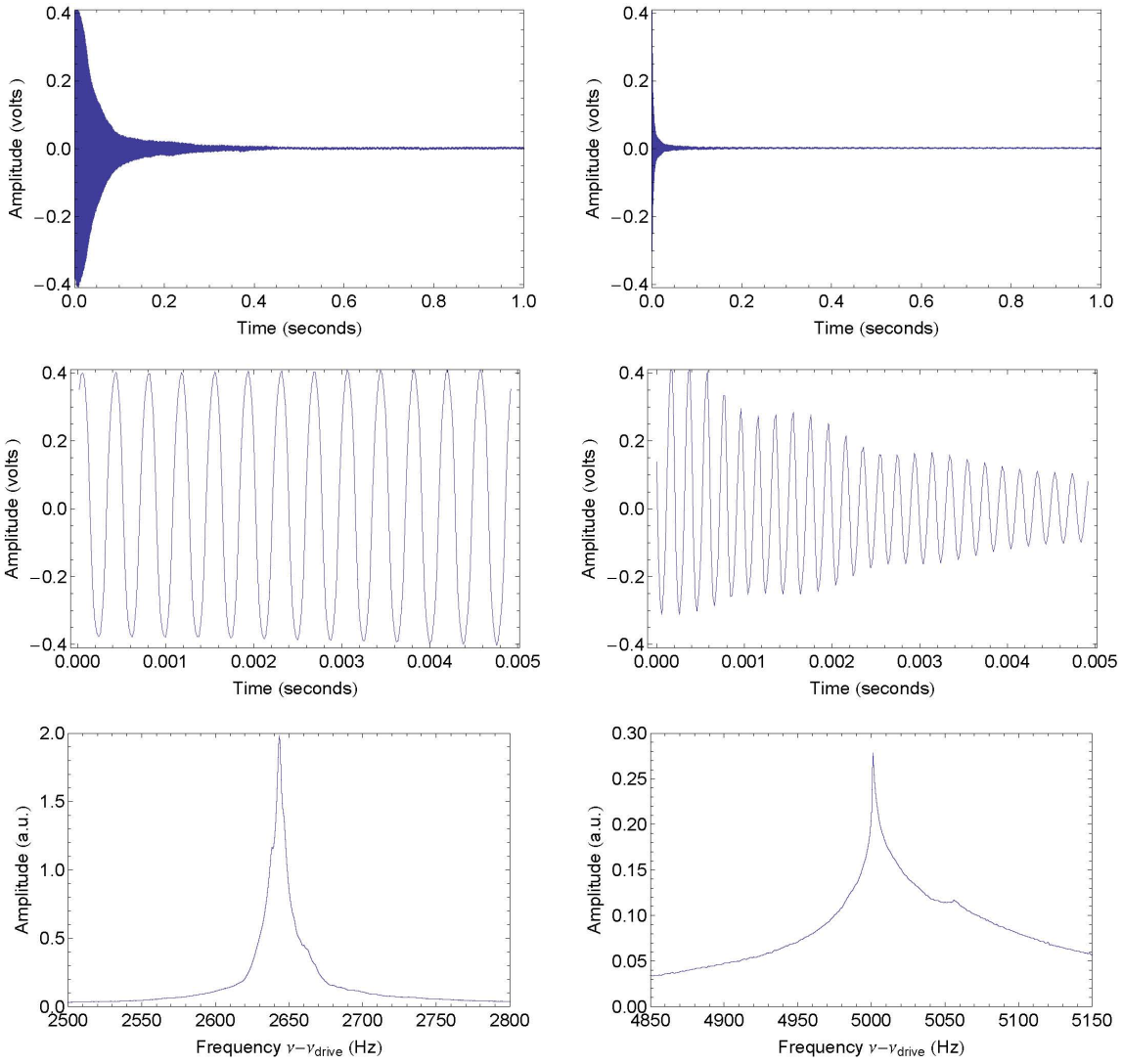

Figure 4.8: A side by side comparison of the NMR signal from a well-shimmed magnet for the ^{3}He probe in the new magnet (left) and the water probe in the 2008 g-factor magnet (right). From top to bottom: the full FID time trace, the first 5 ms to show the fast oscillations, and the Fourier transform.

With the narrow Fourier transform of figure 4.8, we can make a measurement of the magnet drift rate. By measuring the peak value of the Fourier transform over time, we can see that the magnet current is decaying and can measure the rate. 5 weeks after charging the magnet, we took two measurements of the Fourier transform nearly 41 hours apart. We measured an 11 Hz shift on a 168.6 MHz frequency, which shows an average drift rate of 1.6 ppb/hour. This is well within the 10 ppb/hour drift rate guaranteed by the Cryomagnetics, and close to their "expected" value of 1 ppb/hour. We would have expected a slightly lower drift rate ($<$ ppb/hour) after 5 weeks of charging, and this may point to the need for a more aggressive overshoot of the magnet current while charging (we typically "ring in" on the magnet current by overshooting by 1 A, undershooting by 1/2 A, etc.). We have seen a much lower drift rate, which comes from our measurements of the cyclotron frequency, and is discussed in chapter 7.

Further attempts to characterize the magnet stability with the probe were interrupted by our discovery that minor changes in the position of the probe seemed to greatly change the shimming, which is the topic of the next section.

4.6 Rotational Variation of the Magnetic Field Shimming

After carefully shimming the magnet with the ^{3}He probe, we found that rotating the probe caused the shimming to degrade (worsening as the probe was maximally rotated from the original position). Figure 4.9 shows how the FFT of an FID varies

for a particularly bad case as the probe is rotated over 2π radians. For the data in the figure, the magnet has been shimmed at $\Theta = 0$, and is rotated via the positioning threads shown in figure 4.3. This means that, at 2π rad, the probe is rotated back to the original position, but is axially shifted (lower in this case) by 1/28 of an inch. Note that despite this axial shift, the shimming again looks good at 2π.

There could be more than one possible cause for this rotationally dependent shimming. One is poor radial alignment in the magnet. If the sample volume were located far away from the center of the magnet in the x-y plane, rotating the probe could swing the sample volume from a well shimmed location to a poorly shimmed location. The water NMR used in the previous magnet also displayed some rotational dependence to the shimming and radial alignment was a primary suspspect.

However, the radial alignment of the ^{3}He probe should be better than the water NMR probe, due to the assembly discussed above. Estimates of radial misalignments place them at a couple of millimeters at most. The fact that the sample volume can move ≈ 1 mm axially in the field without destroying the shimming suggests that this level of translation should be acceptable if the magnet were well shimmed.

Perhaps a more likely possibility is that there is some residual magnetism in the ^{3}He probe. In this scenario, the initial shimming at $\Theta = 0$ would remove the magnetic gradients introduced both by the superconducting solenoid and by the ^{3}He probe. As the probe is rotated, the gradients from the probe will also rotate, while the shim coils and superconducting solenoid remain fixed, which could cause the shimming to degrade.

Much effort has gone into the search for magnetic materials in the ^{3}He probe.

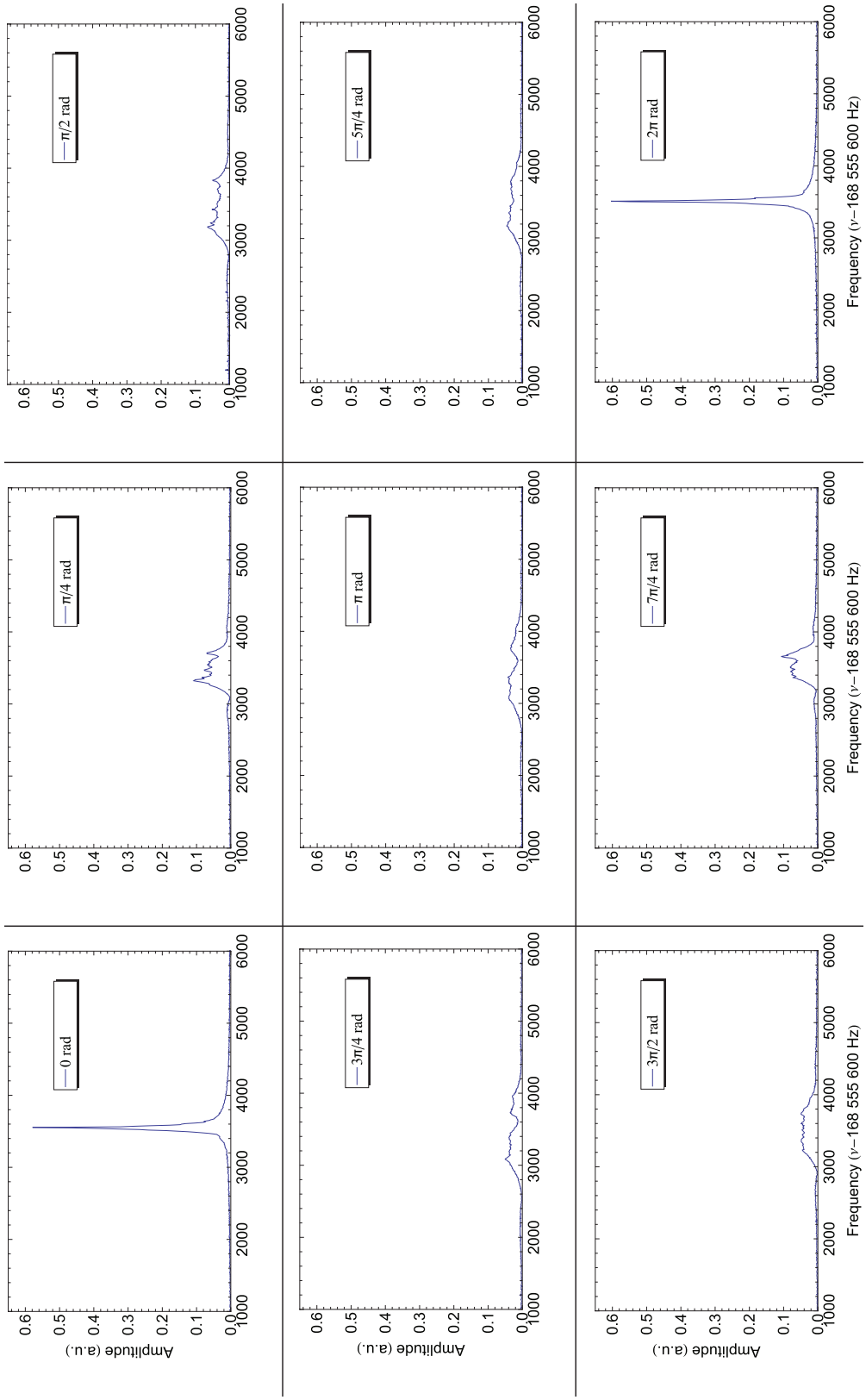

Figure 4.9: A particularly bad case of rotational variation to the shimming for ^{3}He probe. The magnet is shimmed with the probe at $\Theta = 0$, then the probe is rotated while measuring an FID at each point. Note that, at 2π rad, the probe is 1/28" lower in z, even though it has returned to the initial Θ.

Initially, it was found that some SMA connectors that were OFE copper and gold plated contained a thin layer of nickel plating as an adhesion layer. These were replaced with non-magnetic connectors. Several aluminum parts near the magnet region were also replaced with OFE copper. Though the rotational variance improved (to the few ppm level), unfortunately, the sensitivity of the shimming to rotating the probe has not been fully removed.

4.7 Summary

We have designed, built and demonstrated a gaseous ^{3}He NMR probe for magneometry at 4.2 K. This probe can be used in each of the magnets in the lab and can be inserted into the new magnet with the same sliding seal technology that the dliution refrigerator uses. The ^{3}He probe has confirmed the functionality of the shim coils, and we have also shown that the new magnet can be shimmed to 68 ppb over a 1 cm diameter sphere, which is more homogeneous than the magnet in which the previous version of the experiment was performed. However, some rotational dependence of the ^{3}He probe remains, and may be due to residual magnetism in the probe or to radial misalignment of the sample. The previous water NMR probe also showed some rotational variability, and the effect in the new probe will have to be investigated.

Chapter 5

Loading and Detecting a Single Electron

The previous chapters have discussed the general physics of Penning traps, the new cryogenic apparatus used to support the traps and supply the magnetic field, and the low-temperature magnetometry used to measure and shim the magnetic field. This chapter focuses on the electronic interactions with the electrons (and positrons). Guided by the push toward single electron measurements, the chapter will cover the loading mechanisms for both electrons and positrons, the DC biasing necessary to apply the trapping fields and bias the amplifiers, the RF drive and detection schematics used to cool or excite the particles, and, finally, the various methods of detection we use to determine the number of electrons, to tune the anharmonicity, and determine the axial frequency precisely enough to see the small shift from a single quantum cyclotron excitation.

5.1 Electron and Positron Loading

Our easiest method of loading electrons comes from using a field emission point (FEP). We start with 0.018" diameter tungsten rods (ESPI 3N8 tungsten), which we electrochemically etch (see, for example, Appendix A in [81]) to a sharp point. With a tip that has a small radius of curvature, we can now apply a modest voltage (typically < 1 kV) to the FEP under vacuum (preferably in a vacuum of $\ll 10^{-7}$ torr) and generate a large enough electric field to cause field emission. As can be seen in figure 5.4, the current going through the FEP is monitored through a 1 MΩ resistor at room temperature. We also add 200 MΩ in series with the monitoring resistor to limit the current in the event of an accidental short.

Since the electric field in our Penning trap is conservative, trapping electrons fired from the FEP requires the removal of some of their energy in the trapping region. Collisions with background gases are the primary mechanism by which the electrons lose their energy. Though the vacuum in the trap can is typically extremely good ($< 5 \times 10^{-17}$ torr in a similar apparatus at 4.2 K [62]), electrons fired into the trap electodes can free gases that have been cryopumped onto the struck surfaces. As some of the electrons collide and lose energy, they can now remain in the trapping well. We typically fire the FEP for 30-60 seconds at a low current (< 1 nA). To load smaller numbers, we simply fire the FEP at lower and lower currents until we find only 1 in the trap.

The positron loading mechanism is quite different, and one of the main features of the new apparatus is additional space needed to accomodate a positron source. Our source is comprised of ^{22}Na salt that has been electron beam (e-beam) welded into a

thin, titanium-foil covered disc (from Eckert and Ziegler). The activity was measured to be 15.6 $\pm$ 0.5 μCi on Dec 1st, 2009, but the half life of ^{22}Na is 2.603 years, so the activity is constantly decaying, to a value of 5.6 μCi as this thesis is written.

To trap the emitted positrons, we also need to remove some of their energy in the trapping region. Since they would annihilate upon contact with electrodes, we cannot use the same method of collisions as we do for the electron beam. Instead, positrons leaving the source pass through a 2 μm thick, single crystal tungsten moderator, where they are slowed and some of them pick up an electron to form a loosely bound positronium atom [82]. If the atom passes through a sufficiently strong electric field in the trapping region, it can be ionized, and the stripped off electron can carry away enough energy to leave the positron trapped.

This method can also be used to load electrons. By simply inverting the loading electric field (changing the sign of the voltage on all the electrodes), the positron can be ejected while the electron remains. The loading rates from each of these processes should be the symmetric, provided that the trap electrodes are biased to keep secondary electrons from loading into the trap. As expected, the large asymmetry observed when the electrodes are not biased (to prevent secondary loading) is greatly reduced as the biasing is improved [58].

To load positrons, we position the source (see chapter 3) over the loading trap and bias the electrodes to the loading configuration, as shown in figure 5.1. The length of time determines the number of positrons (or electrons) loaded into the trap, and we have demonstrated a rate of 1-2 e^+/min. Given the size of our source ($\approx$ 6.3 μCi at the time the loading data was taken), this leads to a loading rate per mCi

of 3-6 e^+/s/mCi, which is comparable to the rate achieved in a similar loading set up with a 2.5 mCi source[82]. Our absolute loading rate is 2.5-5 times higher than that observed in the University of Washington experiment (using a different loading mechanism) [83], even though our source activity is ≈80 times smaller.

We have found that firing the FEP can reduce the loading rate. Firing the FEP 20 times (at ≈1 nA for ≈1 minute per firing) roughly cut the loading rate in half (for both positrons and electrons). This is not unexpected, since the current from the FEP strikes the tungsten moderator, and the loading requires a layer of adsorbed gas on the moderator. A reduced loading rate has been seen for the same loading mechanism if antiprotons strike the moderator [84], or if a laser heats the moderator [85]. The layer of gas (and loading rate) is restored by thermal cycling the experiment.

To get positrons into the precision trap, they will have to be transferred between the two traps. This will be discussed in chapter 8.

5.2 DC Biasing and RF Drive Lines

In order to bias the electrodes and amplifiers necessary for trapping and detection, we need to bring voltages from the noisy room temperature environment to the 100 mK stage of the dilution refrigerator. To detect the signal from 1 electron, these biases must have very little noise and key voltages must be exceptionally stable. Filtering begins at room temperature, where each of the bias lines is broken out, filtered with an LC lowpass (see figure 5.4) and passed into the IVC via one of several 40-pin Fischer connectors. Since the room temperature filtering happens inside the breakout box, the connection between the breakout box and the hat must be very well

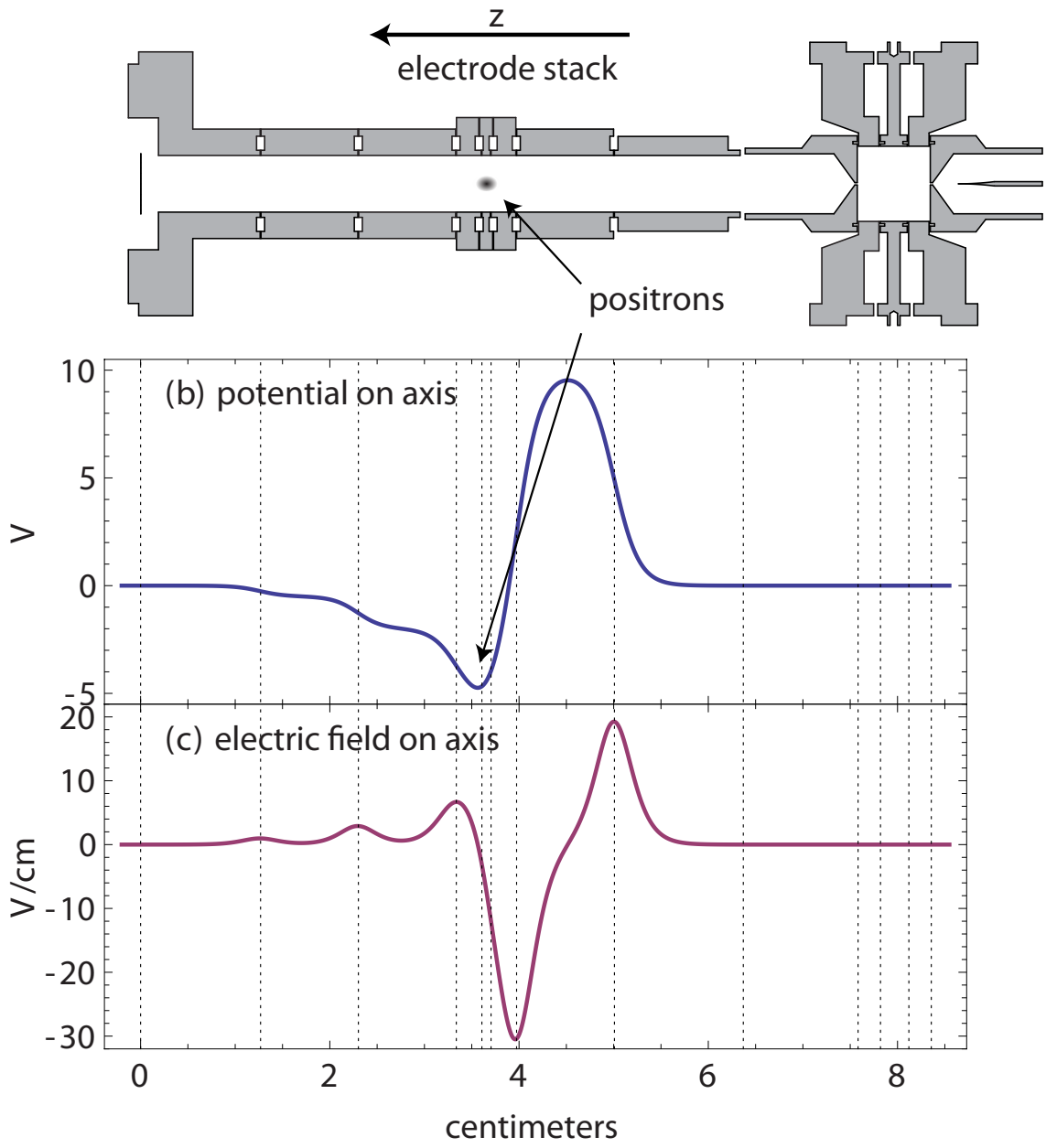

Figure 5.1: The potentials for loading and trapping positrons overlaid on the loading trap stack.

shielded, as in figure 5.2. Adding this shiedling to our own cables, as well as to the temperature sensor and heater cables provided from Janis, proved to be instrumental in eliminating noise and seeing the signal from 1 electron.

Figure 5.2: A cable showing the amount of shielding necessary between the room temperature filter box and the IVC of the experiment.

Each line is then filtered carefully at 1 K and again at 100 mK (see figure 5.4) with another LC filter, before going through one final RC filter at the pinbase. Each bias voltage has its negative lead grounded to the pinbase, which acts as the ground for the whole experiment. This helps to avoid ground loops (provided that the power supplies are not internally grounded, as well), which would reduce the stability of the voltages reaching the electrodes.

For the most sensitive lines (e.g. the ring lines), there is another inductive filter at room temperature, just before the ceramic vacuum feedthrough. Though this set of inductors is, in principle, not a filter (since there is no frequency dependent voltage division), in practice, the stray capacitance of the lines and feedthroughs makes the inductors behave as a low-pass filter. Since it has been left out of the last few schematics of the experiment wiring, this filter is shown carefully in 5.3. Its

absence could be seen via increased noise on the amplifier.

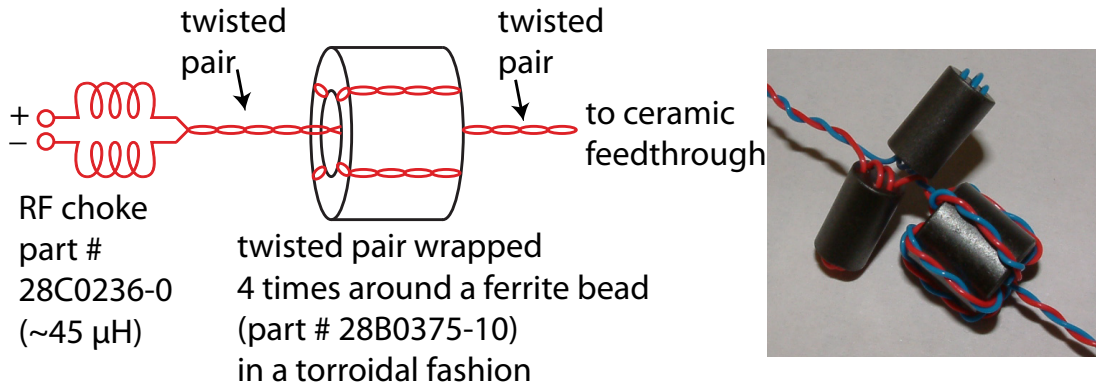

Figure 5.3: Ring filter at the ceramic feedthrough schematic (left) and photo (right)

The FEP requires special filtering, since the components used for the 1 K and 100 mK filter boards are not rated to handle the high voltage of the FEP (up to 1 kV). The FEP filter can be seen in figure 5.4. The capacitor is an ATC capacitor, whose voltage rating is only 50 VDC, but which we have discovered routinely withstands 1 kV when it is cold.

In the typical running configuration (as discussed in chapter 2), the voltage stability of the ring electrode determines stability of the axial frequency. Since the axial response from a single electron is quite narrow ($\approx$1 Hz damping width out of a 200 MHz frequency), we require a high degree of stability for the ring voltage. This is, in part, achieved by a state of the art voltage source (a Fluke 5720A voltage calibrator), which has a stability of 500 ppb per 24 hours. This voltage is filtered through either 1 (a 1 MΩ) or 2 (a 1 MΩ + a 100 MΩ) resistors going to a 10 μF metalized polypropylene film capacitor, leading to a time constant of 10 seconds or 16.8 minutes, depending on which configuration is used. The smaller resistor is typically used

to make large changes in voltage quickly, while the large resistor is used while taking data (and can be added by plugging in an additional box at the hat). To improve the drift when the self-excited oscillator (described below) is on, we can measure the axial frequency to monitor the ring voltage. If the axial frequency drifts, we can apply a correction and charge pump the 10 μF capacitor to keep it stable, by applying 50 ms pulses from a biasDAC (a stable digital to analog converter built by the Harvard physics electronic instrument design lab) stacked on top of the Fluke. These pulses are applied as frequently as the averaging time of the self-excited oscillator.

The ring bias lines go through a high leakage resistance (to avoid forming a voltage divider with the 100 MΩ resistor) ceramic feedthrough at the hat. The resistance is too high to test with a standard electrometer (whose scale typically maxes out at $\approx$ 10 TΩ). Instead, we can use the electron's axial frequency (see section 5.3) to measure the leakage resistance. By unplugging the ring voltage and monitoring the axial drift overnight, we can use the known trap coefficients and the 10 μF capacitance to calculate an RC time constant and extract R. For our test, the axial signal only drifted 82 Hz on 201.177828 MHz over nearly 16 hours, which indicates a leakage resistance of $>$1 PΩ (1 P$\Omega = 10^{15}\Omega$).

The endcap voltages affect the axial frequency stability at the same level as the ring voltage, but are kept extremely stable by grounding them at the still via 10 MΩ resistors. These 10 MΩ resistors are carefully chosen so that their resistance at 4K matches to one part in 10^4, so they can be used for antisymmetric biasing of the endcaps. The stability of the compensation electrode voltage, since the precision trap is orthogonalized [57], is less important (by a factor of $\approx$100) than that of the ring

voltage. We bias the comps with three floating biasDAC channels stacked on top of the output of the Fluke 5720A.

The stability requirements for the loading trap electrodes are also less of a concern to the final measurement. They must be good enough to load and detect particles in the loading trap, but can be unplugged and shielded during g-factor measurements in the precsion trap. The loading trap ring and endcaps are biased with a Fluke 5440B voltage calibrators, while the remaining electrodes are biased with a BabyDAC (a stable digital to analog converter built by the Harvard physics electronic instrument design lab, whose output is not floating).

The cooling power ($\approx 300\ \mu$W at 100 mK) of the dilution refrigerator necessitates careful heat sinking of each bias line as it makes its way from room temperature to the trap electrode. Bias voltages come down in twisted pairs of teflon coated 0.003" diameter constantan wire. Bundles of constantan wires (typically 40 pairs) are then wrapped a few times around a gold plated copper heat sink bobbin (homemade or LakeShore part number HSB-40) and epoxied with (black or blue) Stycast 2850. The bobbins are then bolted onto each stage of the dilution refrigerator.

The RF drive lines are carefully heatsunk and filtered. Each RF drive line from the hat comes down a section of semi-ridgid stainless steel microcoaxial cable (microcoax) to 4 K, to minimize the heatload. At each stage of the dilution refrigerator, a section of copper microcoax is wrapped several turns (typically 4-5) around a heat sink bobbin and is epoxied with Stycast 2850. To reduce room temperature RF noise (either Johnson noise or noise picked up by imperfect shielding of cables), we also add a cold attentuator to each RF drive line. These attenuators can be seen in figure 5.4 and are

installed at the 1 K pot stage of the dilution refrigerator. These filters reduce both the drive amplitude and the noise going down the drive line, which is a worthwhile trade, as we are not limited by the strength of our drives.

5.3 Axial Detection

The axial motion is our primary handle for measuring the spin and cyclotron states of the electron and positron, and is chosen to be about 200 MHz in the precision trap and 53.3 MHz in the loading trap. This careful choice of axial frequeny in the precision trap is determined by several factors: the axial shift for a cyclotron transition, the width of the cyclotron resonance and the power necessary to drive an anomaly transition.

The axial shift for a cyclotron transition (see chapter 6) is given by equation 5.1. Since the shift is inversely proportional to ω_z, moving to higher axial frequencies means that it will be harder to resolve the axial shift from a cyclotron excitation. However, the width of the cyclotron lineshape (see chapter 6) is given by equation 5.2, which goes as ω_z^{-2}. As the axial frequency is increased, the linewidth is getting smaller more quickly than the axial shift. As long as the axial shift is still resolved, this means that a higher frequency is desirable.

$$\delta_c = \frac{e\hbar}{m\omega_z} B_2 \propto \frac{1}{\omega_z} \tag{5.1}$$

$$\Delta\omega_c = \bar{n}_z \delta_c \propto \frac{1}{\omega_z^2} \tag{5.2}$$

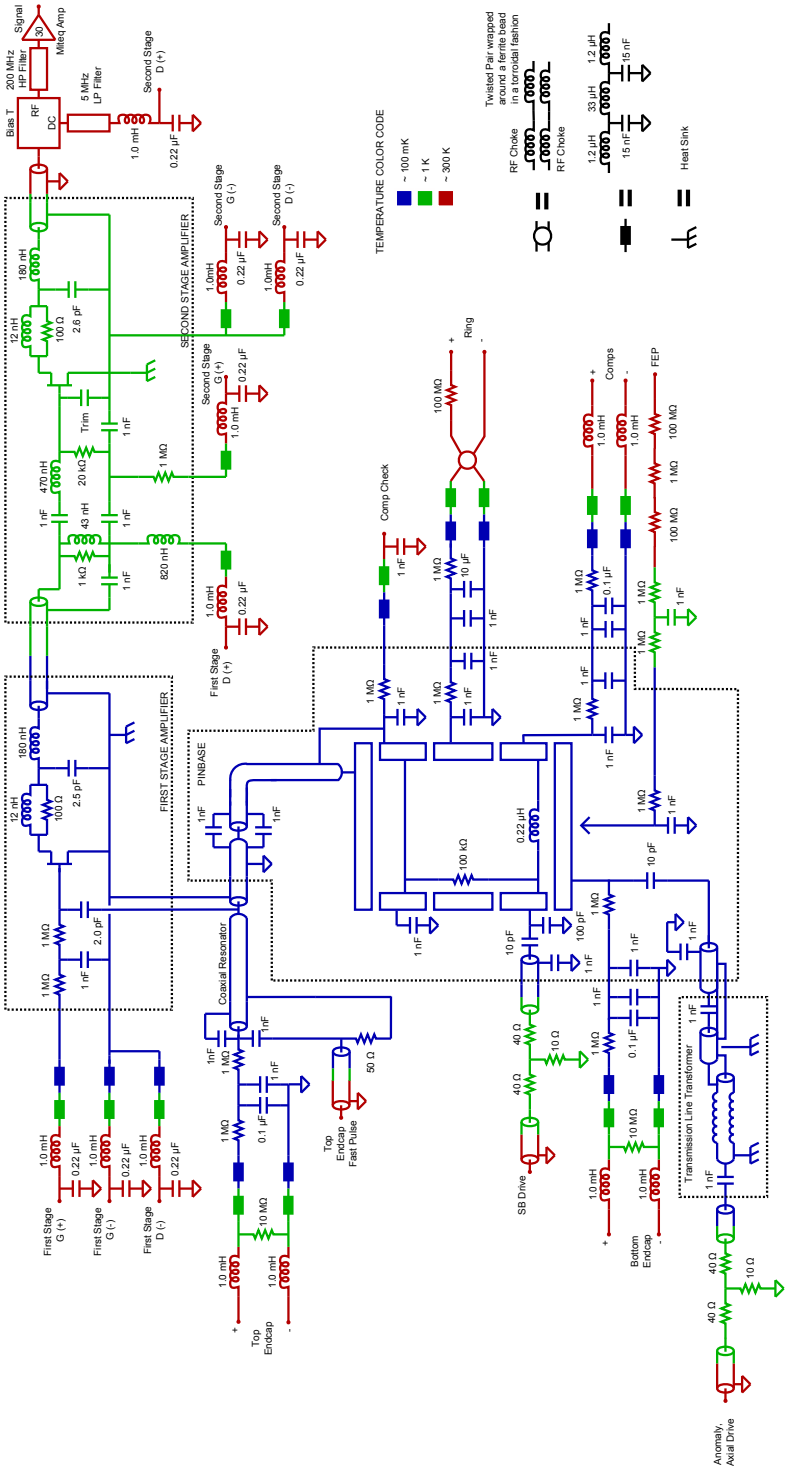

Figure 5.4: Precision trap wiring diagram

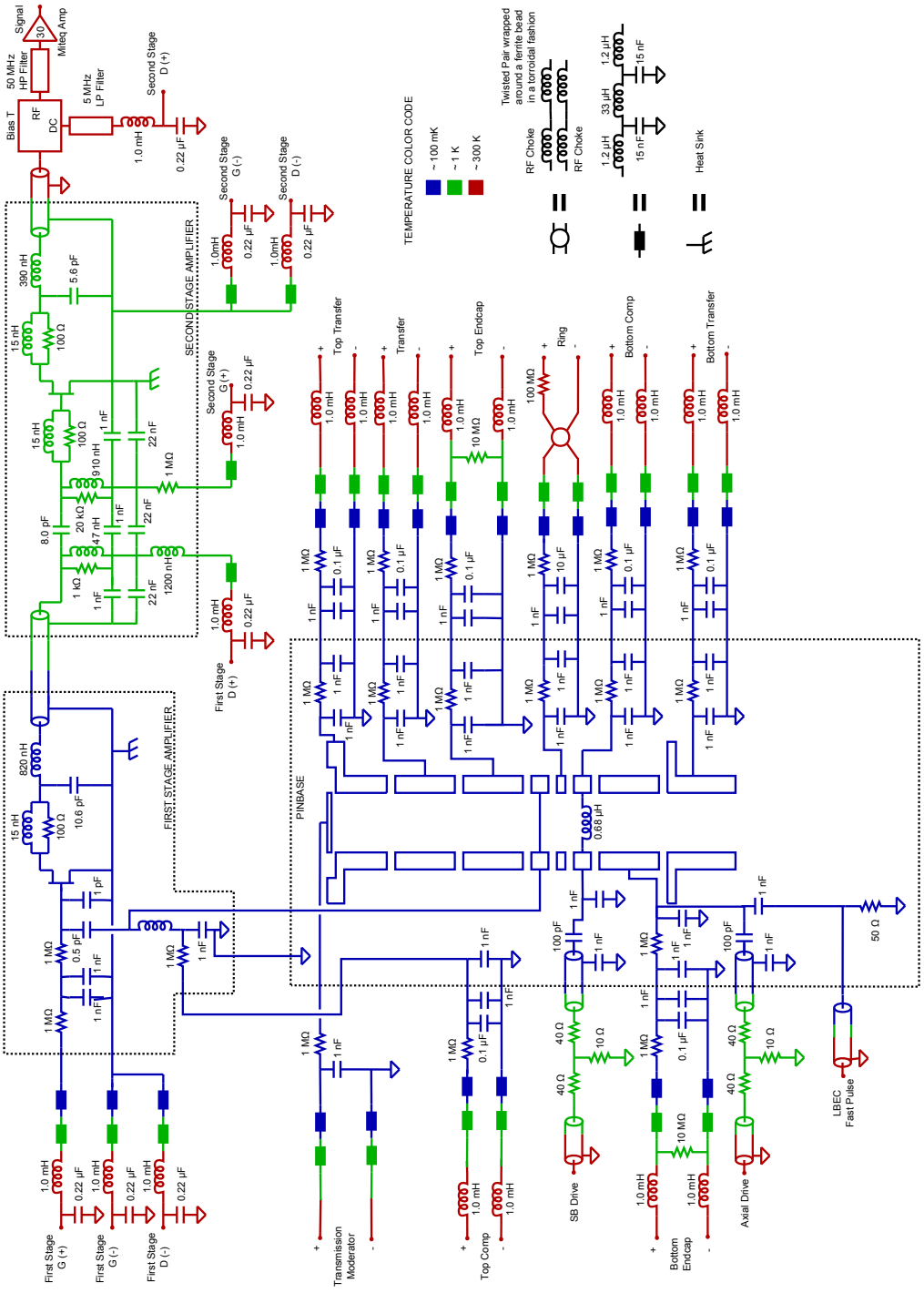

Figure 5.5: Loading trap wiring diagram

The other primary consideration is the power necessary to drive the anomaly transition. This is given by equation 5.3 [81] (relative to the power required at $\omega_z = 0$). The approximation applies when ω_z is far from ω_a.

$$\frac{P(\omega_z)}{P(\omega_z = 0)} = \frac{(\omega_a^2 - \omega_z^2) + \omega_a^2\gamma_z^2}{\omega_a^4 + \omega_a^2\gamma_z^2} \approx \left(1 - \frac{\omega_z^2}{\omega_a^2}\right)^2 \tag{5.3}$$

The anomaly transition can be driven with lower power when the axial frequency approaches the anomaly frequency. If the frequency is too close, axial thermal motion could drive unwanted anomaly transitions; too far, and the power required to drive the anomaly transition may be large enough to induce systematic errors, as has been seen in previous experiments [86].

Balancing these three considerations lead the previous version of this experiment to the choice of 200 MHz for the axial frequency for the precision trap. This choice produced narrow cyclotron linewidths, a measurable axial shift and no measured anomaly power systematic. Thus, we have also chosen 200 MHz for our precision trap axial frequency.

The axial frequency for the loading trap is far less crucial to the measurement. Its value of 53.3 MHz was chosen due to the extensive lab knowledge concerning amplifiers in this frequency range and is much more managable than a 200 MHz coupling. The inductor is wound by hand and the exact frequency is chosen to avoid RF noise from tv stations.

In detecting the axial frequency in either of these cases, the trapping electrodes themselves are the first step. As the electron oscillates in the axial potential well, it induces an image current in the trapping electrodes, given by equation 5.4 [11].

$$I = \frac{e\kappa}{2z_0}\dot{z}, \tag{5.4}$$

Where I is the current induced in the endcaps, e is the electron charge, κ is a dimensionless geometric constant, z_0 is the trap half height (defined in Chapter 2) and $\dot{z}$ is the velocity of the electron.

To detect this current, we put it through the effective resistance of a tuned circuit amplifier (see figure 5.6 for a schematic). The detection electrode and its neighboring electrodes add the unavoidable capacitance. To tune out their reactance at the axial frequency, we add an inductor to form a resonator. For the loading trap amplifier, a hand wound silver coil adds the necessary inductance. At 200 MHz, the inductance necessary to cancel the trap capacitance ($\approx$ 10 pF) is only $\approx$30 nH, which would be difficult to achieve reliably with a traditional coiled inductor, so instead we use the distributed inductance of a transmission line.

The transmission line is custom and consists of a silver wire surrounded by a cylindrical silver outer conductor with vacuum (and the occasional teflon spacer) between them. In order for the axial signal to leave the trap can vacuum, it passes through a custom made, low capacitance feedthrough. This feedthrough is made from a copper outer conductor joined to glass joined to a tungsten inner conductor (constructed by Larson Electronic Glass). The feedthrough becomes part of the transmission line by torch brazing the silver inner conductor to each side of the tungsten (a tricky procedure outlined in [81] Appendix B).

Unavoidably, there is also some loss in the resonator. This can arise from a small series resistance in the inductor (or solder joints) or from lossy RF materials nearby

the resonator (though these are minimized). Near resonance, these losses can be modeled as a large parallel resistor, as is show in figure 5.6.

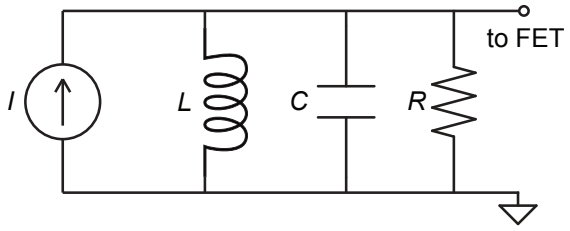

Figure 5.6: Equivalent schematic of the tuned circuit near resonance where Johnson noise in the resistor plus the electron signal acts as a current source, the trap capacitance acts as the capacitor, the coil (or inductance from the transmission line) acts as the inductor and the resistance arises from a small series resistance in in the inductor.

On resonance, the impedance of the RLC circuit is resistive and is given by equation 5.5, where L is the inductance, ω_r is the resonant frequency and Q is the typical Q-factor of a resonator. The size of the signal we measure from the electron is proportional to this resistance, so we aim to have as high of a Q-factor as possible.

$$R = Q\omega_r L \tag{5.5}$$

When there are no charged partices in the trap, the amplifier is driven by Johnson noise in the resistor, as given by equation 5.6:

$$I_n = \sqrt{\frac{4k_B T \Delta f}{R}} \tag{5.6}$$

where I_n is the current noise, k_B is the Boltzmann constant, T is the temperature, and Δf is the frequency bandwidth of interest.

The Johnson noise current going through the resistor dissipates power in the form of $(I_n)^2 Re(Z)$, where Z is the frequency dependent impedance of the resonator. The impedance of the parallel RLC circuit is well known (see, for example, section 8.4 in [87]) with a real component

$$Re(Z) = R\frac{(\Gamma/2)^2}{(\omega - \omega_R)^2 + (\Gamma/2)^2} \tag{5.7}$$

that has a Lorentzian shape with a full width at half maximum of $\Gamma = \omega_r/Q = 1/(RC)$. These amplifier noise resonances are our typical method for evaluating the Q of our resonators, with examples shown in figures 5.7 and 5.8 at 4 K for the first stage precision amplifier and loading amplifier, respectively.

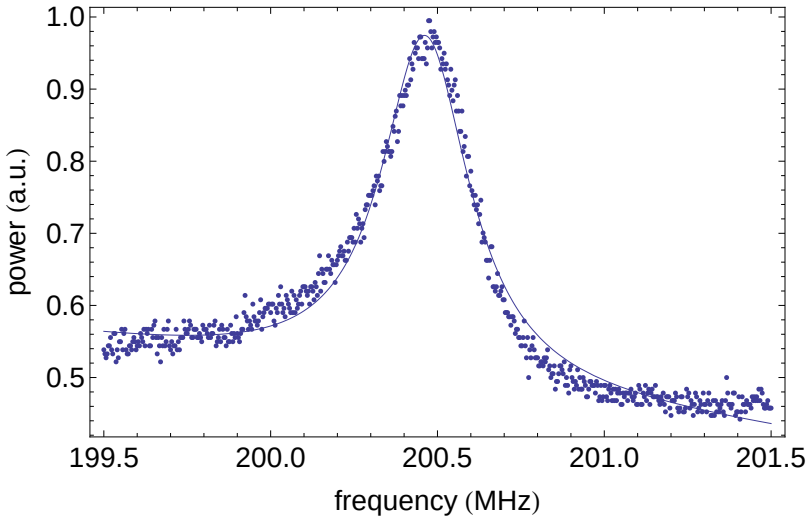

Figure 5.7: The noise resonance of the first stage precision amplifier at ≈ 4K viewed through the detection chain. The amplifier is dissipating 100 μW and the Q fits to greater than 600.

The apparatus places several demands on the choice for an amplifier, which must be able to function at high magnetic fields and cryogenic temperatures (which can cause the carriers can freeze out of many silicon based devices, for example). In

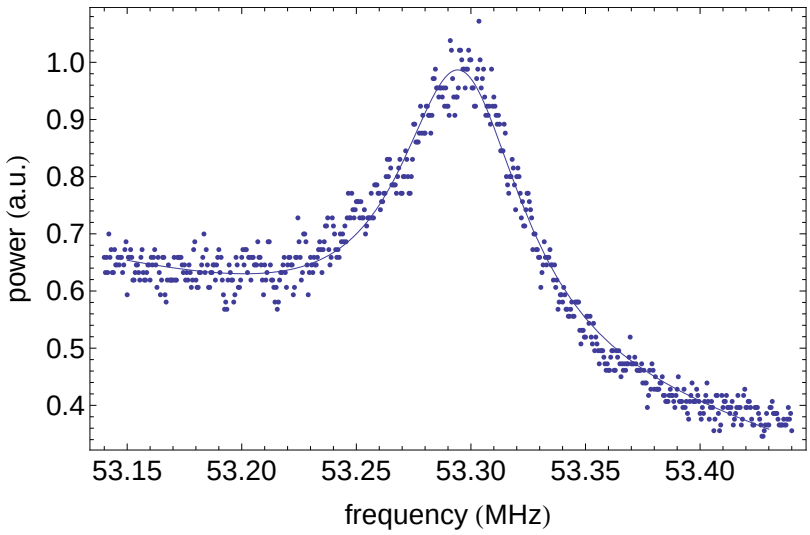

Figure 5.8: The noise resonance of the first stage loading amplifier at $\approx$ 4K viewed through the detection chain. The amplifier is dissipating 100 μW and the Q fits to greater than 800

addition, the first amplifier is located at the 100 mK mixing chamber stage of a dilution refrigerator. Since our dilution refrigerator can only dissipate a maximum of 330 μW, the amplifiers must produce only a fraction of this power.

Fortunately, all of these requirements can be met with the Fujitsu FHX13LG HEMT (high electron mobility transistor). For each trap, the detection chain consists of 2 stages of amplification (see figure 5.4 and figure 5.5 for schematics). Each amplifier is built on a carefully laid out homemade amp board. These layouts can be seen in figures 5.9 through 5.12.

The first stage amplifier is starved down to run below 100 μW and can be run as low as 10 μW. The signal must then travel through several sections of lossy but thermally isolating stainless steel microcoax, on its way to room temperature. In order to elevate above the noise floor of the first room temperature amplifier, a second stage of amplification is needed. We locate the second stage amplifier at the still, where

the temperature is higher (≈0.6-0.7 K) and the cooling power is high enough to accomodate more power dissipation (we run the second stage amplifiers at 250 μW). The loss between the first and second stage amplifiers is typically <2 dB.

Even with the amplifiers running at such low power, great care is taken to heat sink them. To this end, one of the source leads of each FET is soldered directly to a silver post that is bolted to the dilution refrigerator stage on which each amp is located. Since the FETs cannot withstand the high temperatures of our usual lead-tin solder (the maximum storage temperature of the FHX13LG is 175° C), we solder this lead to the post using a low-temperature indium solder (52% Indium/48% Tin), which has a eutectic point of 118° C. Even with this heat sinking, the temperature of the amplifiers tends to remain higher than the temperature of the mixing chamber (see chapter 7) while they are on (and also for quite some time after they turn off).

When there is an electron in the trap, the induced image current (equation 5.4) passes through the equivalent resistance of the resonator, and the electron loses energy at the rate of I^2R, which damps the axial motion. The damping rate arising from this resistive loss is given by equation 5.8.

$$\gamma_z = \left(\frac{e\kappa}{2z_0}\right)^2 \frac{R}{m} \tag{5.8}$$

and is ≈1 Hz in our trap.

The response of the electrons to the Johnson noise of the resonator circuit can be represented as an LC circuit in parallel with the resonator, as shown in figure 5.13 [88], where

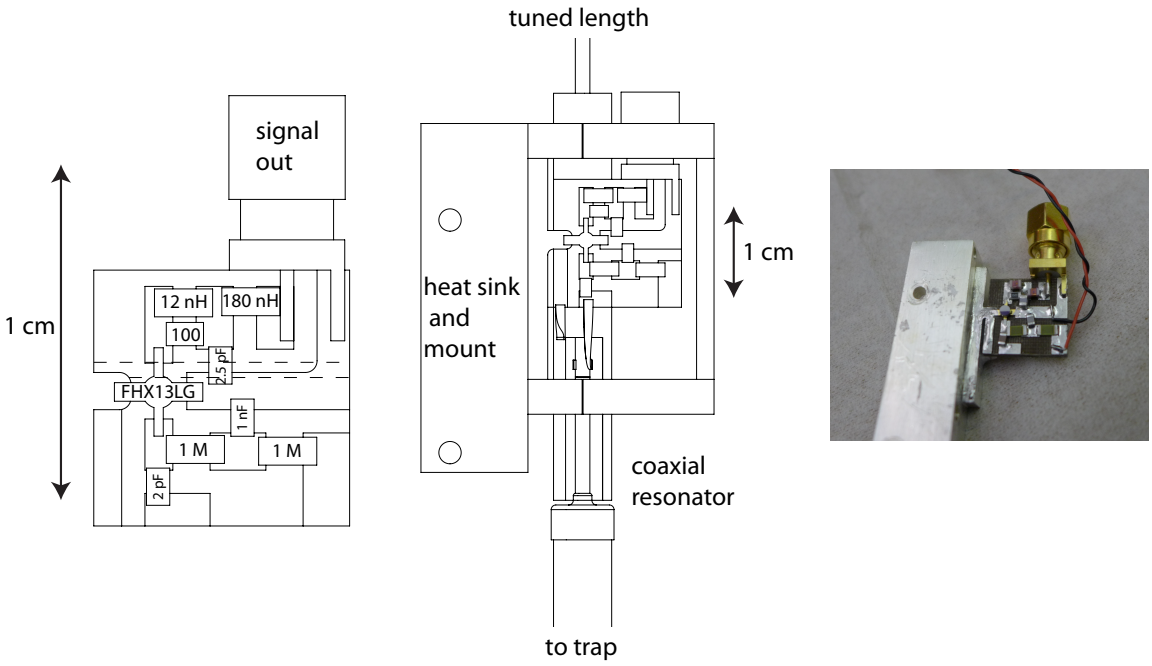

Figure 5.9: The first stage precision amplifier: amp board (left) in the amp can with the heat sink and transmission line (center) and photo (right). Numerical values without units are resistances in ohms.

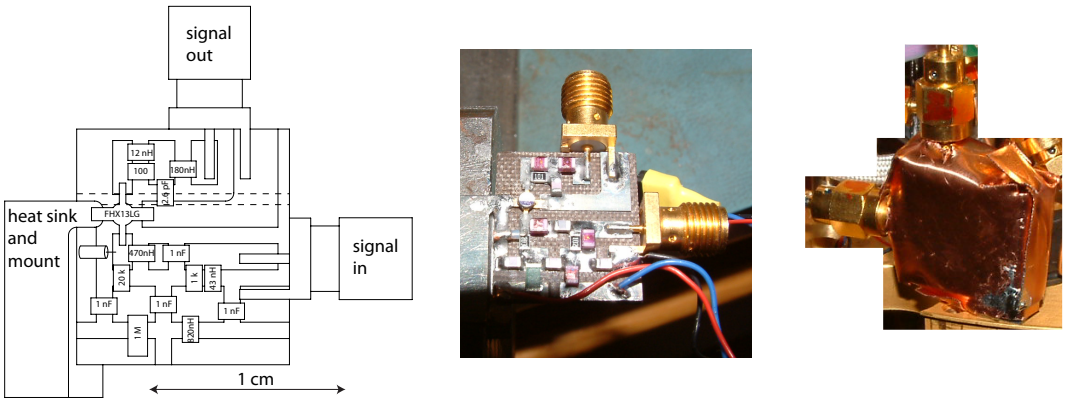

Figure 5.10: The second stage precision amplifier: amp board and mount (left) photo of the unshielded amplifier and mount (center) and photo of the shielded amplifier bolted to the still (right). Numerical values without units are resistances in ohms.

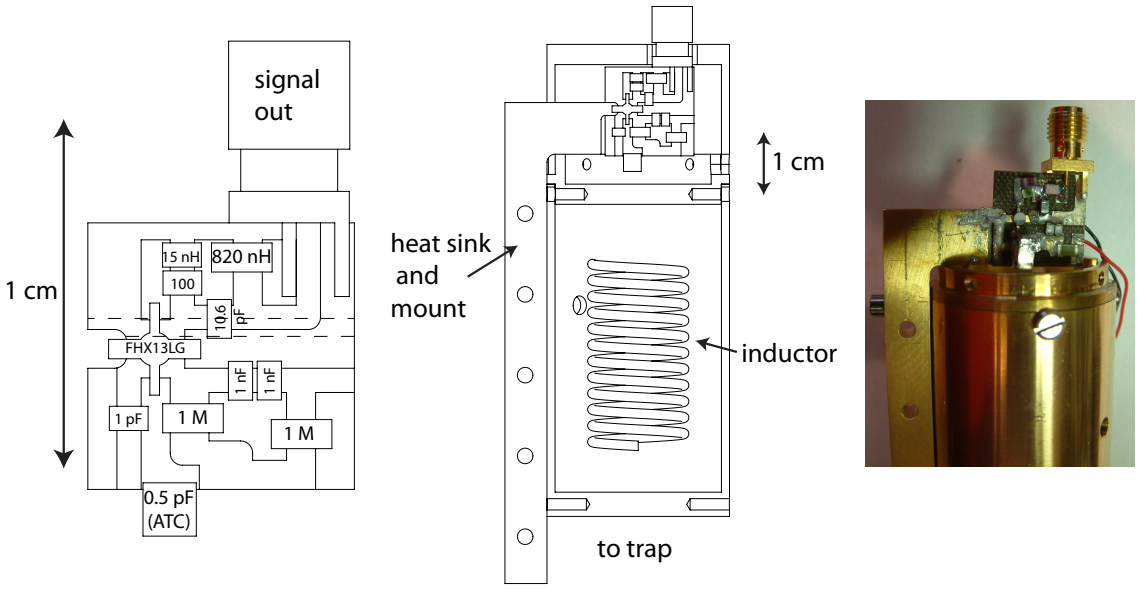

Figure 5.11: The first stage loading amplifier: amp board (left) in the amp can with the heat sink and inductor (center) and photo (right). Numerical values without units are resistances in ohms.

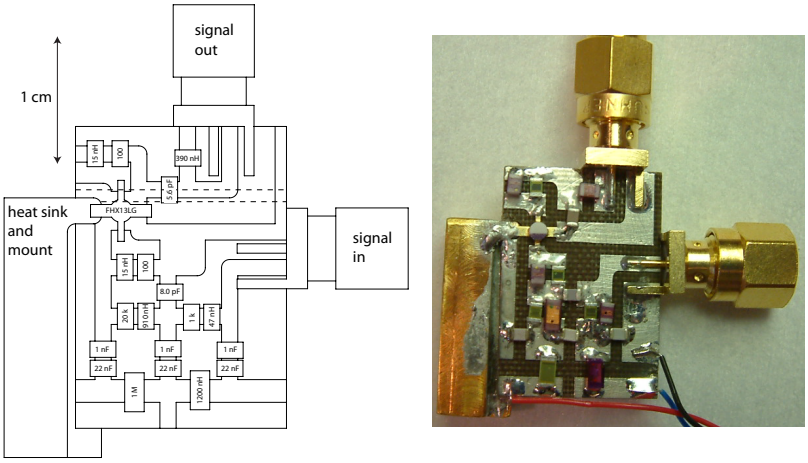

Figure 5.12: The second stage loading amplifier: amp board and mount (left) and photo of the unshielded amplifier and mount (right). Numerical values without units are resistances in ohms.

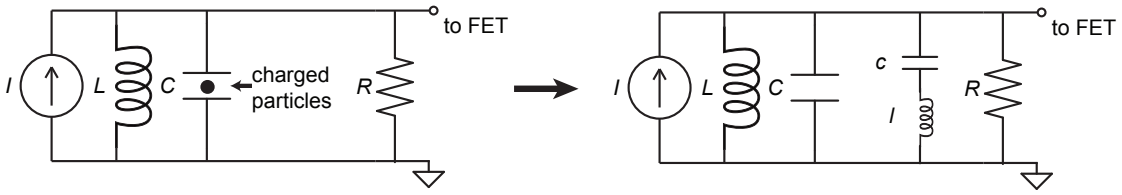

Figure 5.13: When there are trapped charged particles between the electrodes (left), they can be modeled as the equivalent circuit shown (right)

$$l = \frac{m}{N}\left(\frac{2z_0}{\kappa e}\right) = \frac{R}{N\gamma_z} \tag{5.9}$$

and

$$c = \frac{N}{\omega_z^2 l} \tag{5.10}$$

Here, N is the number of charged particles and the rest of the terms have been defined above. When $\omega \approx \omega_r$ (where ω_r is the resonant frequency of the tuned circuit for the amplifier), the power spectrum can be shown to be represented by equation 5.11 [89]:

$$P \propto \frac{\omega_r^4(\omega_z^2 - \omega^2)^2}{[(\omega_z^2 - \omega^2)(\omega_r^2 - \omega^2) - \omega^2\Gamma N\gamma_z]^2 + \omega^2\Gamma^2[(\omega_z^2 - \omega^2) + \Gamma N\gamma_z]^2} \tag{5.11}$$

For this work, the most useful limit of this expression is when there are small numbers of particles in the trap (so that $N\gamma_z << \Gamma$). In this limit, the power spectrum is an inverted Lorentzian dip in the amplifier noise resonance. The dip has a full width at half maximum is given by $N\gamma_z$. These dips are an easy way to see electrons in the trap, and an example of dip is shown in figure 5.14.

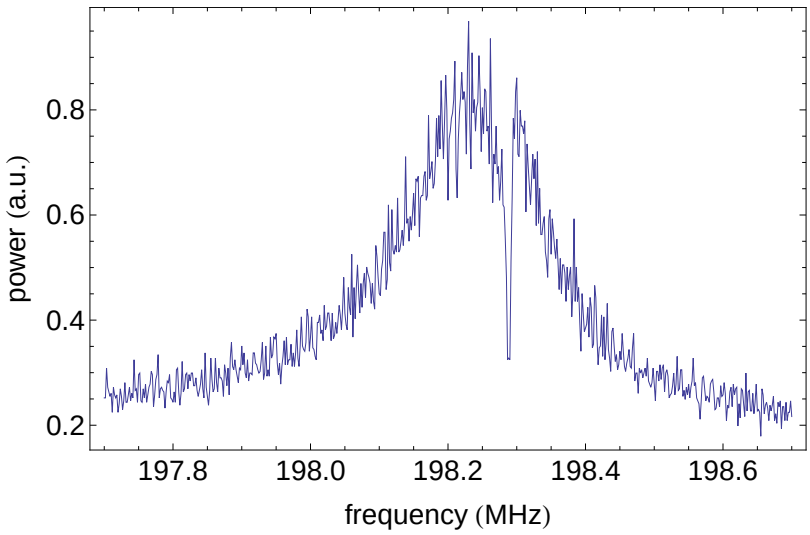

Figure 5.14: A dip in the amplifier noise resonance power spectrum. Here there are about 10,000 electrons in the precision trap.

5.4 Driving the Axial Motion and Anharmonicity

Though monitoring the dip in the amplifier noise resonance is a useful way to detect electrons in the trap, as the number decreases, so does the width of the dip (eventually approaching the single particle axial damping width). To see such a narrow dip requires a low resolution bandwidth on the spectrum analyzer used to monitor the noise coming from the amplifier, which generally means longer sweeping times and averaging times. If there is drift in the axial frequency, it can "wash out" the dip, as the spectrum analyzer averages the dip as it moves over several different axial frequencies.

By exciting the electron above its thermal amplitude, we can measure the axial frequency more quickly by increasing the signal to noise. By applying a drive, measuring the response at each frequency, and then stepping the frequency, we can trace out an axial resonance. The easiest and most direct way to do this would be to use a

at $\nu_z + \delta$. By simply applying the drive to one electrode, however, it would be difficult to avoid direct feedthrough of the drive to the amplifier, which is also tuned to be resonant at ν_z. It is possible to apply the drive to two electrodes, carefully choosing the phase and attenuation of each drive such that the drives cancel at the amplifier but not at the electron. This is, in fact, what we do with the self-excited oscillator (see section 5.5).

Another way to avoid direct feedthrough is to modulate the trapping potential [7]. By applying a low frequency ν_1 ($\approx$1-2 orders of magnitude lower than ν_z), we can modulate the trapping potential [11], which produces sidebands at $\nu_z \pm \nu_1$. By applying a drive at $\nu_z \pm \nu_1$, we can drive the electron's axial motion and measure a response at ν_z. This schematic for applying this drive can be seen in figure 5.15. Notice that ν_1 is at 4.995 MHz and we are driving the $\nu_z - \nu_1$ sideband. Instead of applying the low frequency drive to the ring electrode or to both endcaps (since it is the potential between the ring and endcaps that is largely setting the trapping potential), we apply the drive only to the bottom endcap. This anti-symmetric application of the drive still produces the desired modulated trapping potential.

The axial response from applying these drives is measured by a phase-sensitive technique and the schematic of the detection chain is also shown in figure 5.15. We mix the $\approx$200 MHz signal down (first with a signal at $\nu_z - 5MHz$ and then with another at 4.995 MHz) to 5 kHz so that it can be read by a signal analyzer and a data acquisition card on the computer. By measuring the amplitude of the response, we can use a global phase to separate out the in phase and out of phase components. Example responses are shown in figure 5.16.

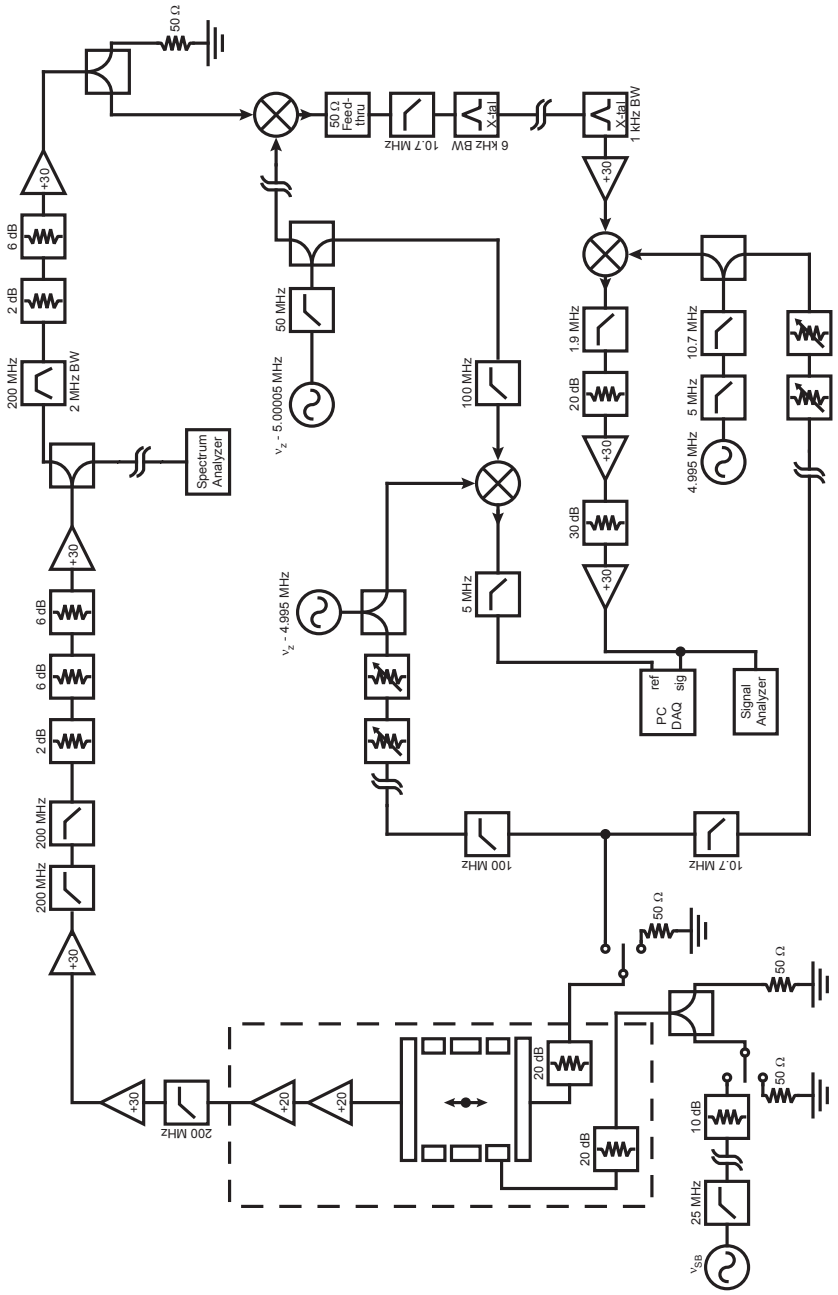

Figure 5.15: The schematic for the direct drive and detection set up.

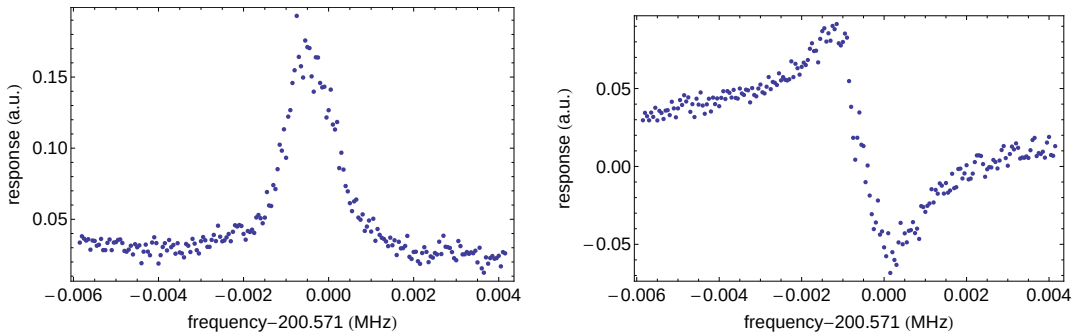

Figure 5.16: In phase response of a small driven cloud of eletrons (left) and the out of phase response for the same small cloud of electrons (right).

These driven responses are instrumental in the push going from first observing large clouds of electrons to observing smaller numbers. In addition to speeding up detection by increasing signal to noise, the driven response can be used to tune the anharmonicity of the trap. For a trap that is not well tuned, the driven response will display an anharmonic resonance. An example of this is shown in figure 5.17. In the figure, the drive frequency is first swept up and then swept down. The classic anharmonic oscillator will display hysteresis in the sweep direction, as the response is not purely a function of frequency.

Anharmonicity generally arises from trap imperfections that are not sufficiently cancelled because of a slight mistuning of the compensation voltage. Though the optimal voltage can be calculated for the desired trap geometry, machining tolerances and other imperfections generally make the actual compensation voltage slightly different. By loading a small cloud of electrons, applying a drive sweeping up and then down as in figure 5.17, the anharmonicity can be measured. The direction of the anharmonic response can be used to tune the compensation voltage until the trap is harmonic. For the precision trap and the response in figure 5.17, the compensation

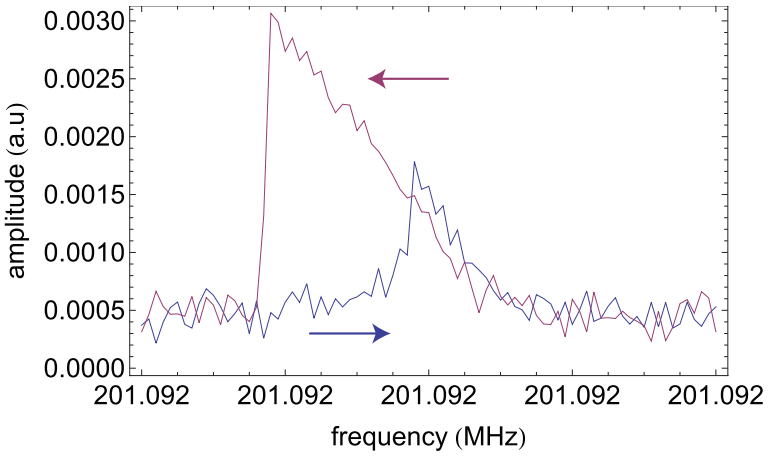

Figure 5.17: An example of an anharmonic driven response from a cloud of electrons. The arrows indicate the direction of the sweep. In this case, the compensation voltage is set too low.

voltage is set too low. The leading anharmonicity term comes from C_4 in equation 2.9. In a typical orthogonalized trap, C_4 can be tuned to be a few parts in 10^{-5} [56], and no significant asymmetry between drive sweeps is observed. This process can then be iterated for smaller and smaller numbers of electrons until the anharmonicity is reduced to below the single particle damping width.

5.5 Self-Excited Oscillator

Instead of using an external frequency synthesizer to excite the electron's axial motion, it is possible to use the signal derived from the electron itself, making a self-excited oscillator (SEO) [90]. To set up a stable self-excitation, we begin by considering the axial equation of motion. As equation 5.12 shows, we will consider the case with a driving force and also allow for anharmonicity (hence, ω_z is a function of the amplitude, A).

$$\ddot{z} + \gamma_z \dot{z} + \omega_z (A)^2 z = F_d(t)/m, \tag{5.12}$$

For analysis, it's convenient to write the driving force in terms of the damping, as in equation 5.13, so that equation 5.12 is rewritten into equation 5.14. For a stable oscillation, equation 5.14 makes it clear that achieving $G = 1$ is the ideal case where the drive cancels the damping.

$$F_d(t)/m = G\gamma_z \dot{z} \tag{5.13}$$

$$\ddot{z} + (1 - G)\gamma_z \dot{z} + \omega_z (A)^2 z = 0, \tag{5.14}$$

This assumes that the axial oscillation and the drive applied to the particle are in phase. If we allow a phase shift (ϕ) between them (this global phase is set by the cable length that closes the feedback loop), then the condition of cancelling the damping and achieving stable oscillation becomes that of equation 5.15.

$$G \cos\phi = 1 \tag{5.15}$$

In practice, we tune the global phase carefully so that $\phi \approx 0$. If the condition of equation 5.15 is not satisfied, the particle's amplitude will be excited or damp exponentially, and the motion will not be stable. Since there is noise in the feedback loop (from the amplifiers), any change in the noise or amplifier gain will cause this exponential run away. In order to counteract these fluctuations, we need a way to adjust the gain in nearly real time so that the amplitude remains stable.

We acomplish this by using a digital signal processor (DSP). The DSP performs a discrete fourier transform of the 5 kHz mixed down signal to determine the amplitude of the oscillation (only considering the highest bin height). The DSP then compares the measured amplitude to the desired amplitude and adjusts the gain by adjusting attenuation on a voltage variable attenuator. See figure 5.18 for a schematic of the SEO drive and detection setup. The signal from the electron is applied to the bottom endcap and the bottom compensation electrode. By tuning the phase with a variable cable length and the relative attenuation with fixed and variable attenuators, we are able to cancel the drive that reaches the amplifier by $\approx$30 dB.

As we will see in chapter 7, the large signal to noise and quick read out time of the self-excited oscillator make it ideal for monitoring the axial frequency and looking for small changes. See figure 5.19 for an example of the self-excited signal from a single electron. This will be our primary handle for measuing cyclotron excitations and anomaly transitions.

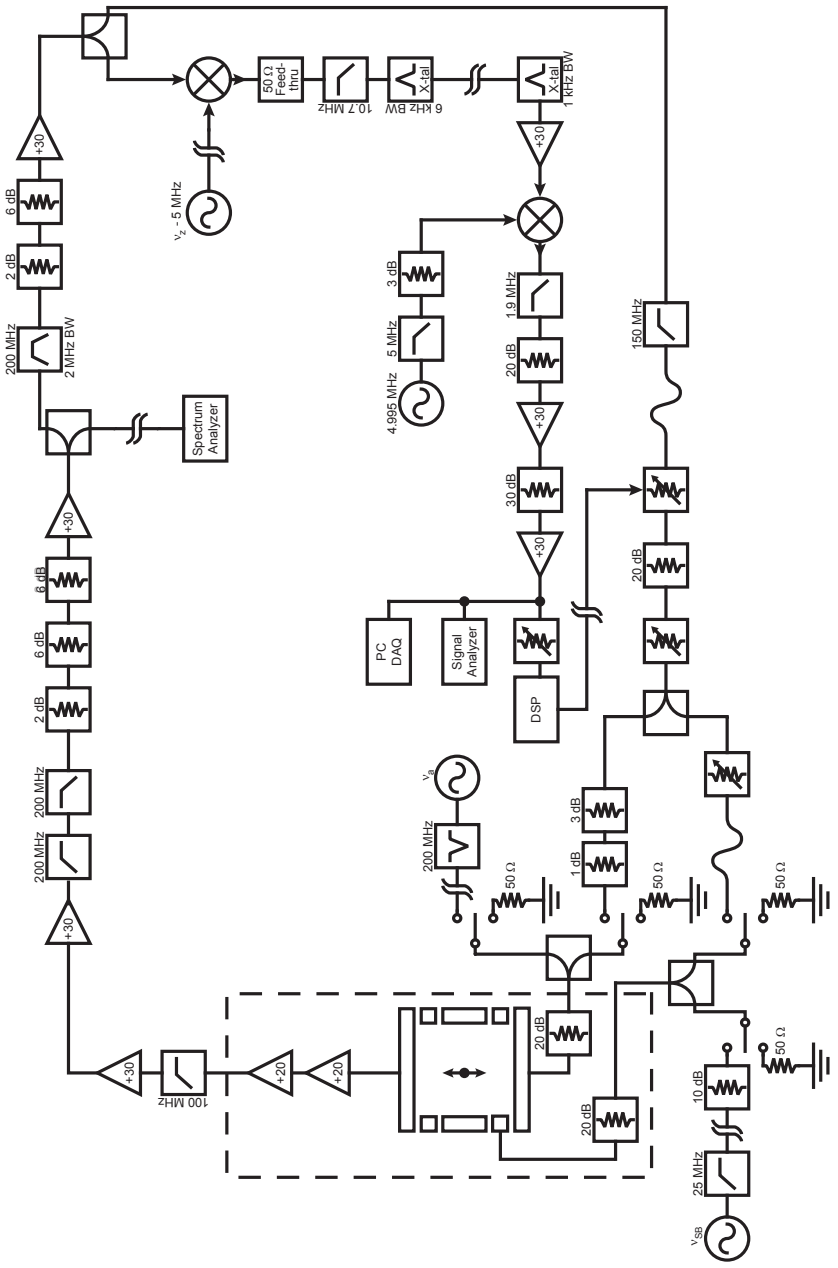

Figure 5.18: a schematic of the Self-excited oscillator drive and detection setup.

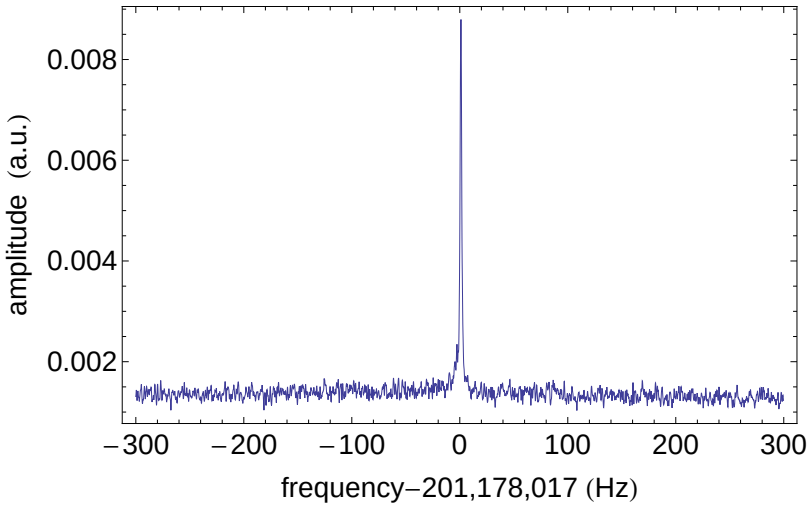

Figure 5.19: Example of the self-excited signal from a single electron.

Chapter 6

Microwaves and Microwave Resonances

The crux of the g-factor measurement is determining the cyclotron and spin (or anomaly) frequencies [2, 13]. For our high magnetic field strength (≈5.2 T), these transitions are at 145.5 GHz in the microwave (D band) regime (see table 2.2). This chapter will focus on the microwave aspect of the experiment, which will include the electron's resonances, their detection, and the microwave generation and transmission necessary to excite them. The Penning trap itself also acts as a microwave cavity, and its modes affect the g-factor measurement by increasing the cyclotron lifetime and shifting the cyclotron frequency. These effects will also be discussed.

6.1 Spin and Cyclotron Resonances

The primary measurements that determine the electron g-factor are of the cyclotron and anomaly frequencies. For an electron in a magnetic field, the spin can only take on 2 values—up or down. For each spin state, there is a ladder of cyclotron states available to the electron. If the cyclotron frequency were purely harmonic, then this would lead to the energy diagram in figure 6.1, with the left ladder for spin down and the right ladder for spin up. The ladders do not align since the electron g-factor deviates slightly from 2 (so that $\nu_s = g/2\ \nu_c$ for a free electron in a magnetic field), so the spin and cyclotron frequencies are different by about a part per thousand. Including special relativity makes the cyclotron states slightly anharmonic, as there is a state dependent relativistic shift, as seen in figure 6.2.

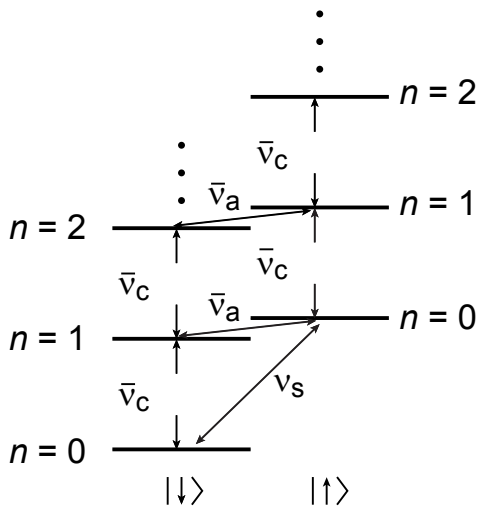

Figure 6.1: The energy levels of an electron in a Penning trap, neglecting special relativity. Bars denote trap modified frequencies.

This slight shift can be thought of as a relativistic mass increase for each increasing

cyclotron state. Here, the change in cyclotron frequency is given by equation 6.1 and δ is defined in equation 6.2 [11]. Because this relativistic shift is state dependent, one benefit of being able to detect single cyclotron jumps (see chapter 7) is that we can choose the cyclotron and anomaly transitions we wish to use for spectroscopy and, thus, remove all uncertainty due to the relativistic shift. The states and transitions we use are shown in red in figure 6.2.

$$\Delta\nu_c = -\delta\,(n + 1 + m_s) \tag{6.1}$$

$$\frac{\delta}{\nu_c} = \frac{h\nu_c}{mc^2} \tag{6.2}$$

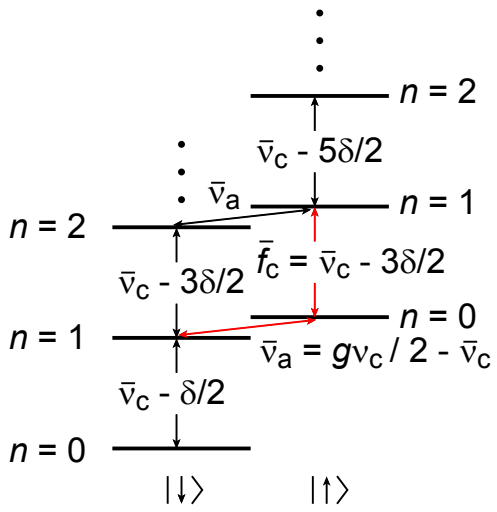

Figure 6.2: The energy levels of an electron in a Penning trap, including special relativistic shifts. Bars denote trap modified frequencies and δ is defined in equation 6.2. The red arrows indicate the cyclotron and anomaly transitions measured in [2] and in chapter 7.

6.2 Magnetic Bottle and Detection

As can be seen from figure 6.2, we measure cyclotron transitions between the ground and first excited state for a spin up electron. Though the detection of single microwave photons has been demonstrated in select systems [91, 92], detecting a single ≈150 GHz photon inside of a precision Penning trap would be impractical. Instead, we detect the cyclotron (and spin) state of the electron by coupling the motion to the axial frequency by adding a magnetic distortion to the trap. The distortion (called the magnetic bottle) is given by:

$$\Delta B_z = B_2 \left((z^2 - \rho^2/2)\hat{z} - (\rho z)\hat{\rho} \right) \tag{6.3}$$

and is generated by a pair of nickel rings placed outside of the trapping electrodes (figure 2.4). In the high magnetic field of the superconducting solenoid, the magnetism of the nickel rings saturates at $\mu_0 M/(4\pi) = 0.0485T$ [11], giving $B_2 = 655$ T/m^2 for our geometry.

For a particle in the magnetic bottle, there is a contribution to the Hamiltonian in the form of $-\boldsymbol{\mu} \cdot \boldsymbol{\Delta B}$. For a particle centered in the trap ($\rho = 0$), the extra term is given by equation 6.4.

$$\Delta H(\rho = 0) = -\mu B_2 z^2 \tag{6.4}$$

which makes the axial potential:

$$H_z = \frac{m\omega_{z0}^2 z^2}{2} - \mu B_2 z^2 = (\frac{1}{2} m\omega_{z0}^2 - \mu B_2) z^2 \tag{6.5}$$

This equation shows the utility of the magnetic bottle. The axial frequency now depends not only on the electrostatic trapping potential, but also on the total magnetic moment of the electron. Since the frequency depends on the total magnetic moment, we will see contributions from the spin state, the cyclotron state and the magnetron state. For a well-cooled particle, however, the contribution of the magnetron motion to the overall magnetic moment is neglible. Then, the axial potential becomes :

$$H_z = \left(\frac{1}{2}m\omega_{z0}^2 - \mu_B B_2(\frac{1}{2} + n + \frac{g}{2}m_s)\right) z^2 \tag{6.6}$$

since g/2 $\approx$ 2, the effect of a spin transition or a one-quantum cyclotron excitation is quite similar and shifts the axial frequency by:

$$\frac{\Delta\omega_z}{\omega_z} = \frac{2\mu_B B_2(\frac{1}{2} + n + \frac{g}{2}m_s)}{m\omega_{z0}^2} \tag{6.7}$$

This small change in frequency signals whether or not a cyclotron excitation or spin flip has occured.

The measurement is a quantum non-demolition (QND) measurement since the Hamiltonian from equation 6.6 commutes with the cyclotron and spin Hamiltonians. Monitoring the axial frequency to determine the cyclotron (or spin) state does not alter the cyclotron (or spin) state, though spontaneous emission can still cause the state to decay. Figure 6.3 shows a cyclotron excitation from the aparatus used in [2]. Transitions in our new magnetic bottle will be shown in chapter 7.

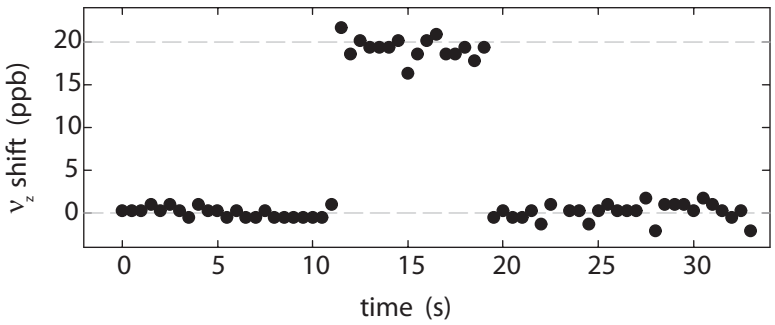

Figure 6.3: The axial shift from a cyclotron excitation from the aparatus used in [2].

6.3 Consequences of the Magnetic Bottle: Broadened Lineshapes

Though the magnetic bottle allows us to monitor the spin and cyclotron states by observing shifts in the axial frequency, the bottle has some undesirable consequences, as well. These effects are primarily due to coupling the thermal axial motion in the magnetic bottle gradient to the cyclotron and spin frequencies. With the trap electrodes at 100 mK, the electron is in its cyclotron ground state (see section 2.4). Due to the long lifetime of the spin state ($\approx$ 5 years—see table 2.2), the spin also remains in a known state over the course of a measurement. The axial motion (whose frequency is only $\approx$200 MHz) is in thermal equilibrium with the detection electronics and has an average quantum number of k $>$ 10.

The magnetic bottle adds a quadratic axial magnetic field dependence, so any field dependent frequency (cyclotron, spin or anomaly) is rewritten to be:

$$\omega(z) = \omega_0 \left(1 + \frac{B_2}{B} z^2\right) \tag{6.8}$$

where ω_0 represents any of the field dependent frequencies and B_2 is the magnetic bottle strength introduced above. We can then define a linewidth parameter [93, 11]:

$$\Delta\omega \equiv \omega_0 \frac{B_2}{B}\langle z^2\rangle = \omega_0 \frac{B_2}{B}\frac{k_B T_z}{m\omega_z^2} \tag{6.9}$$

where in the second equation, the equipartion theorem relates the average axial position squared to the axial temperature. This linewidth parameter and the timescale for thermalization (γ_z) determine the general lineshape (fully worked out in [11, 81, 93]). For our purposes, it is useful to consider the lineshape in two limits: where $\Delta\omega \ll \gamma_z$ (the case where the axial motion is strongly coupled to the detection electronics temperature bath) or $\Delta\omega \gg \gamma_z$ (the case where the axial motion is decoupled from the detection electronics temperature bath).

In the case of strong axial coupling ($\Delta\omega \ll \gamma_z$), the axial position relaxes to the thermal average in the time it takes to resolve the frequency of interest. The lineshape arising from this limit will be a lorentzian that is offset from the central value (ω_0) by the linewidth parameter ($\Delta\omega$). The average thermal position also broadens the lorentzian, so it has a modified linewidth of $\gamma_0 + 2\Delta\omega^2/\gamma_z$, where γ_0 is the natural linewidth. For our frequencies and axial damping rates, the anomaly lineshape should be well approximated by this limit.

In the case of weak axial coupling ($\Delta\omega \gg \gamma_z$), the axial motion is decoupled from the detection electronics during the time required to determine the frequency of interest. For each excitation, the axial motion is in a particular quantum state, and the lineshape would be given by a lorentzian shifted from the central frequency, as in equation 6.8. Between excitation attempts, however, the axial motion has time

to rethermalize, and the lineshape that is built up from multiple attempts is the convolution of the natural lineshape of each attempt and the distribution of axial states (which follows a Boltzmann distribution). This leads to a lineshape that has a sharp edge at ω_0 that decays exponentially away with a width of $\Delta\omega$. The cyclotron lineshape should be well approximated by this limit.

These lineshapes illustrate the unfortunate consequence of adding a magnetic bottle to detect the cyclotron and spin state: broadened lineshapes, which make determining the cyclotron and anomaly frequencies more difficult. Since uncertainty in the lineshapes was the primary source of uncertainty in the 2008 g-factor measurement [2], it would be best to remove the thermal lineshape entirely. As a first step in this direction, we have reduced the magnetic bottle size in the new apparatus by a factor of 2.3 (see chapter 7).

6.4 The Cylindrical Penning Trap as a Microwave Cavity

The cylindrical Penning trap was designed as an alternative to the hyperbolic trap due to the ease of calculating its electromagnetic properties [53]. The precision Penning trap has cylindrical symmetry and has a set of microwave resonances (its cavity modes), which can affect the electron's resonances [94, 95]. Inside the cavity, the electrode walls are gold plated silver, which, especially at cryogenic temperatures, is an exceptionally good conductor [96]. Though there are small gaps between electrodes, $\lambda/4$ chokes (see figure 2.4) are included to reflect microwave power that

would otherwise leave the cavity. For these reasons, the trap approximates an ideal cylindrical cavity.

The boundary conditions for an ideal conductor are that $E_{\|}$ and $B_{\perp}$ are equal to zero at any boundary and the other components are continuous across the boundary. Applying these to the cylinder leads to the standard transverse-electric (TE) and transverse-magnetic (TM) modes that are well-known (derived, for example in [97]). The electric and magnetic fields are shown in equations 6.10(a-d) for the TE and TM modes, using ρ, ϕ and z as the usual cylindrical coordinates:

For TE_{mnp}:

$$\begin{aligned}\mathbf{E} =& E_0 \frac{{}^{(E)}\omega_{mnp}}{c} \left(\frac{\rho_0}{x'_{mn}}\right)^2 \sin(\tfrac{p\pi}{2}(\tfrac{z}{z_0}+1)) \\ & \left[\mp\hat{\boldsymbol{\rho}}\ \frac{m}{\rho}\ J_m(x'_{mn}\tfrac{\rho}{\rho_0})\cos({}^{(E)}\omega_{mnp}t \mp m\phi)\right. \\ & \left. -\hat{\boldsymbol{\phi}}\ \frac{x'_{mn}}{\rho_0}\ J'_m(x'_{mn}\tfrac{\rho}{\rho_0})\sin({}^{(E)}\omega_{mnp}t \mp m\phi)\right] \end{aligned} \tag{6.10a}$$

$$\begin{aligned}\mathbf{B} =& \frac{E_0}{c}\left[\hat{\mathbf{z}}\ J_m(x'_{mn}\tfrac{\rho}{\rho_0})\sin(\tfrac{p\pi}{2}(\tfrac{z}{z_0}+1))\cos({}^{(E)}\omega_{mnp}t \mp m\phi)\right. \\ & + \frac{p\pi}{2z_0}\left(\frac{\rho_0}{x'_{mn}}\right)^2 \cos(\tfrac{p\pi}{2}(\tfrac{z}{z_0}+1)) \\ & \left[\ \hat{\boldsymbol{\rho}}\ \frac{x'_{mn}}{\rho_0}\ J'_m(x'_{mn}\tfrac{\rho}{\rho_0})\cos({}^{(E)}\omega_{mnp}t \mp m\phi)\right. \\ & \left.\left. \pm\hat{\boldsymbol{\phi}}\ \frac{m}{\rho}\ J_m(x'_{mn}\tfrac{\rho}{\rho_0})\sin({}^{(E)}\omega_{mnp}t \mp m\phi)\right]\right] \end{aligned} \tag{6.10b}$$

For TM_{mnp}:

$$\begin{aligned}\mathbf{E} =& E_0 \Bigg[\hat{\mathbf{z}}\ J_m(x_{mn}\tfrac{\rho}{\rho_0})\cos(\tfrac{p\pi}{2}(\tfrac{z}{z_0}+1))\cos({}^{(M)}\omega_{mnp}t \mp m\phi) \\ &- \frac{p\pi}{2z_0}\left(\frac{\rho_0}{x_{mn}}\right)^2 \sin(\tfrac{p\pi}{2}(\tfrac{z}{z_0}+1)) \\ &\quad\Bigg[\ \hat{\boldsymbol{\rho}}\ \frac{x_{mn}}{\rho_0}\ J'_m(x_{mn}\tfrac{\rho}{\rho_0})\cos({}^{(M)}\omega_{mnp}t \mp m\phi) \\ &\quad \pm\hat{\boldsymbol{\phi}}\ \frac{m}{\rho}\ J_m(x_{mn}\tfrac{\rho}{\rho_0})\sin({}^{(M)}\omega_{mnp}t \mp m\phi)\Bigg]\Bigg] \end{aligned} \tag{6.10c}$$

$$\begin{aligned}\mathbf{B} =& \frac{E_0}{c}\frac{{}^{(M)}\omega_{mnp}}{c}\left(\frac{\rho_0}{x_{mn}}\right)^2 \cos(\tfrac{p\pi}{2}(\tfrac{z}{z_0}+1)) \\ &\quad\Bigg[\pm\hat{\boldsymbol{\rho}}\ \frac{m}{\rho}\ J_m(x_{mn}\tfrac{\rho}{\rho_0})\cos({}^{(M)}\omega_{mnp}t \mp m\phi) \\ &\quad +\hat{\boldsymbol{\phi}}\ \frac{x_{mn}}{\rho_0}\ J'_m(x_{mn}\tfrac{\rho}{\rho_0})\sin({}^{(M)}\omega_{mnp}t \mp m\phi)\Bigg]. \end{aligned} \tag{6.10d}$$

The indices m, n and p indicate the number of nodes or anti-nodes in each direction– m (=0, 1, ...) is the number of nodes along the ϕ direction over π radians, n (=1, 2, ...) is the number anti-nodes in E_ϕ going out radially, and p (denoted as TE1, TE2,... or TM0, TM1, ...) is the number of anti-nodes along the z-direction. J_m are the familiar Bessel functions of order m, while x_{mn} is the nth zero of the mth order Bessel function. Primes indicate deritives, so that J'_m is the first derivative of the mth order Bessel function and x'_{mn} are the zeroes of this function. The frequencies of these modes are given by equations 6.11(a-b).

$${}^{(E)}\omega_{mnp} = c\sqrt{\left(\frac{x'_{mn}}{\rho_0}\right)^2 + \left(\frac{p\pi}{2z_0}\right)^2} \tag{6.11a}$$

$${}^{(M)}\omega_{mnp} = c\sqrt{\left(\frac{x_{mn}}{\rho_0}\right)^2 + \left(\frac{p\pi}{2z_0}\right)^2}. \tag{6.11b}$$

Several modes are of special interest to the g-factor measurement. Perhaps the

most important are those that couple to the cyclotron motion of the particle in the x-y plane—modes that have a non-zero value of the transverse electric field. For both TE and TM modes, the transverse components of the electric field are go as:

$$\sin(\tfrac{p\pi}{2}(\tfrac{z}{z_0}+1)) = \begin{cases} (-1)^{p/2}\sin(\tfrac{p\pi z}{2z_0}) & \text{for even } p, \\ (-1)^{(p-1)/2}\cos(\tfrac{p\pi z}{2z_0}) & \text{for odd } p, \end{cases} \tag{6.12}$$

For a particle centered in the trap ($\rho \to 0$ and $z \to 0$), the electric field for modes with even p go to zero, so we will consider modes with odd p to couple to the cyclotron. Additionally, the transverse electric field is either proportional to $\frac{m}{\rho}\ J_m(x'^{(\prime)}_{mn}\frac{\rho}{\rho_0})$ or $\frac{x'^{(\prime)}_{mn}}{\rho_0}J'_m(x'^{(\prime)}_{mn}\frac{\rho}{\rho_0})$. Equations 6.13(a-b) show that, for a particle well centered in the trap ($\rho \to 0$ and $z \to 0$), only the fields with m=1 remain.

$$\frac{m}{\rho}\ J_m(x'^{(\prime)}_{mn}\tfrac{\rho}{\rho_0}) \sim \begin{cases} \dfrac{1}{(m-1)!}\left(\dfrac{x'^{(\prime)}_{mn}}{2\rho_0}\right)^m \rho^{m-1} & \text{for } m > 0 \\ 0 & \text{for } m = 0 \end{cases} \tag{6.13a}$$

$$\frac{x'^{(\prime)}_{mn}}{\rho_0}J'_m(x'^{(\prime)}_{mn}\tfrac{\rho}{\rho_0}) \sim \begin{cases} \dfrac{1}{(m-1)!}\left(\dfrac{x'^{(\prime)}_{mn}}{2\rho_0}\right)^m \rho^{m-1} & \text{for } m > 0 \\ -\dfrac{x'^{(\prime)2}_{0n}}{2\rho_0^2}\rho & \text{for } m = 0. \end{cases} \tag{6.13b}$$

Combining these considerations, we see that the cyclotron coupling modes of interest are the $TE_{1n(odd)}$ and $TM_{1n(odd)}$ modes. If the cyclotron frequency approaches one of these modes, the coupled oscillators shift each other's frequencies so that the cyclotron frequency is modified from its free space value [13]. A better understanding of the cavity modes was one of the primary improvements of the 2008 g-factor measurement [2] over the 2006 measurement [12]. For g-factor data, the cyclotron

frequency should be far away from these modes to minimize the cavity shift and its uncertainty.

Avoiding these modes also drastically increases the cyclotron lifetime. Spontaneous emission is inhibited [98] by decreasing the density of states into which the cyclotron can radiate. Previously, the lifetime of the cyclotron has been increased by more than 100 over its free space lifetime. For our purposes, this increase in lifetime is crucial to the measurement, as it gives us enough time to average our self-excited oscillator to read out the cyclotron state (see chapters 5 and 7).

Aside from the modes that couple to the cyclotron frequency, there is another set of modes that could be of interest to the g-factor experiment. Modes with electric fields that vary as $z\hat{\rho}$ or $\rho\hat{z}$ couple the axial and cyclotron motions, and could be used for cavity assisted axial sideband cooling (see chapter 8). At the trap center, the $\mathrm{TE}_{1n(even)}$ and $\mathrm{TM}_{1n(even)}$ display this gradient.

An ideal geometry for a Penning trap designed for a g-factor measurement would contain a region of frequency space where 1.) no cyclotron coupling modes occur and 2.) several cooling modes are present. The 2008 measurement was performed in a cylindrical trap that fulfilled the first requirement, but did not have any conveniently located cooling modes. Our current trap design (a more complete description of which can be found in [58]) satisfies both conditions. Figure 6.4 shows the locations of the various modes for different trap geometries. The dotted line in the figure is our current trap geometry, which contains a frequency window with no coupling modes but with 3 available cooling modes.

The modes of figure 6.4 are calculated for a perfectly conducting closed cylinder.

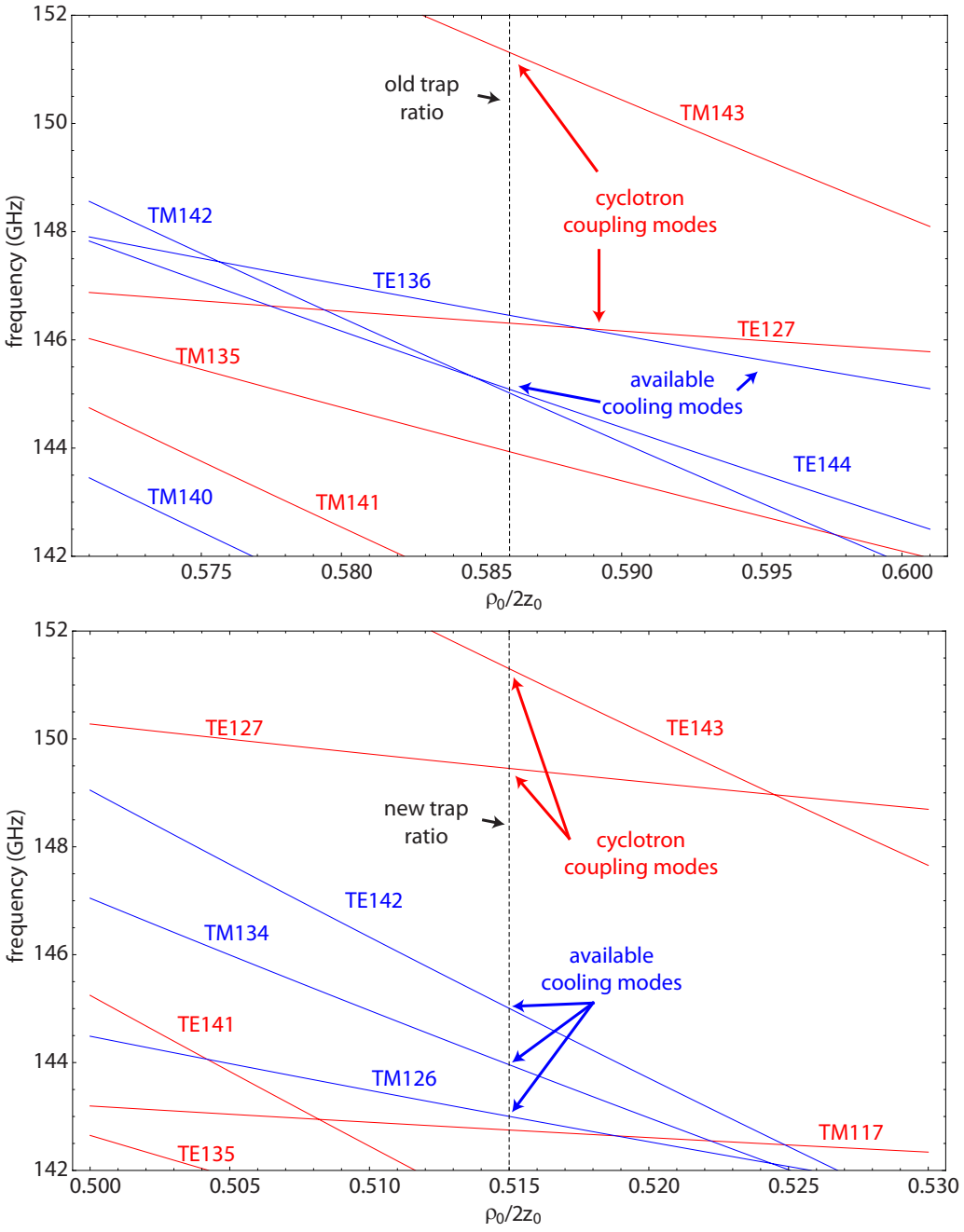

Figure 6.4: The calculated locations of the various modes as a function of the cylindrical trap geometry. Red modes couple to the cyclotron motion and blue modes enhance the coupling between the axial and cyclotron motion. The dashed line shows the trap geometry for the old trap (top) and the new trap (bottom).

The finite conductivity of the electrodes, the holes and slits, and the other imperfections of our real trap cause the mode frequencies to be shifted slightly and cause each mode to have a finite Q factor. In order to perform a g-factor measurement at the precision of the 2008 measurement, the frequencies and Q's of the real trap modes must be identified. The methods below have been discussed carefully in [99, 100, 13, 2], so only a brief summary is presented below.

To map a large region of interest, one can use a parametric mode map [99, 100]. In this method, an RF drive is applied to a cloud of electrons at twice the axial frequency. For a certain range of parameters (above a threshold drive strength) the drive parametrically excites the center of mass motion of the electron cloud. In a manner that is not completely understood, the amplitude of CM motion is, at times, proportional to cyclotron damping rate. This proportionality can be used to measure the cavity modes, since the lifetime of the cyclotron state depends on the proximity of the cyclotron frequency to a cavity mode. Thus, by sweeping the magnetic field while monitoring the CM drive amplitude, the modes of the cavity can be mapped out over a large region (typically 10 GHz out of 145 GHz) in several hours. The mode frequencies are typically close enough to the calculated values that they can be individually identified. By repeating this type of mode map after a room temperature thermal cycle, it has been shown that the mode Q's and locations are remarkably resilient [13].

The mapping of nearby modes can also be done with a single electron. In this method, the cyclotron lifetime is measured with a single electron by building up statistics over many decay events. See chapter 7 for more details on an individual

lifetime measurement. By measuring cyclotron lifetimes at several magnetic field values, the locations and Q-factors of the modes can determined well enough to correct for the frequency shift so that it is no longer the dominant source of error in the g-factor measurement [13, 2]

6.5 Microwaves into the Apparatus

In order to drive spin flips or cyclotron excitations, we must generate microwaves and couple them into the trap. Our microwave drive begins from an Agilent E8251A Performance Signal Generator. Its upgraded internal oscillator (option UNJ), which improves the frequency stability and the phase noise of the source, also serves as the timebase for the entire experiment. Because the g-factor is unitless and because we measure it as a ratio of frequencies, the absolute value of the second is irrelevant to the measurement. However, since the anomaly and cyclotron frequencies are resolved at different times, the stability of the timebase is crucial on the measurement timsecale. The signal generator's frequency stability was sufficient for the 0.28 ppt of the 2008 electron g-factor measurement [2] and should be sufficient for a positron measurement of similar accuracy. For an improved measurement, however, we have acquired a Stanford Research Systems FS725 rubidium frequency standard, whose aging rate is more than an order of magnitude better than the signal generator's.

We begin by generating $\bar{\nu}_c/10$ from the signal generator, as it can only output frequencies up to 20 GHz. To get to the $\approx$150 GHz cyclotron frequency, we then send the signal through an SMA cable into a 10x multiplier (see figure 6.7), which is custom made by ELVA-1 Millimeter Wave Division and uses an impact ionization

avalanche transit-time (IMPATT) diode to multiply the frequency by ten. This high power diode can put out as much as 2 mW, though for individual spin and cyclotron excitations, the actual power required is much lower. Therefore, the circuit also contains 2 voltage controlled attenuators that can reduce the drive strength of the 150 GHz signal by up to $\approx$ 200 dB.

The microwave access to the experiment is through a port on the top of the IVC (see figure 6.7), which means we need to position the multiplier directly above the dilution refrigerator when in use. In order to still be able to remove the experiment (by pulling it vertically out of the Dewar), the multiplier is mounted in a custom made box on a post that allows it to swing in and out of position. When aligned, the post positions the microwave horn from the multiplier over the microwave flange at the hat.

To get into the IVC, the microwaves travel through a custom made teflon KF25 kwik flange into one of the clear shot ports on the dilution refrigerator. We have found that the teflon flange seals much better with a little vacumm grease, as the teflon tends to compress somewhat as it gets clamped. Beneath the teflon flange, several sections of gold-plated copper waveguide direct the microwaves from room temperature to 4 K. Though a single section of waveguide could transmit the microwaves with less loss, it would also present an unacceptable heatload on the 4 K section of the apparatus. Instead, several sections of waveguide with horns are carefully joined together with G10 in order to minimize the space between microwave horns, but to maximize the length of the thermal path through the thin G10 sections. As can be seen in figure 6.5, the microwave horns are kept 1/16" apart, while the length of thin (0.038" wall

thickness) G10 is greater than 1". There are 5 total sections of waveguide, the last of which mates directly into a custom flange on the 4K stage of the dilution refrigerator.

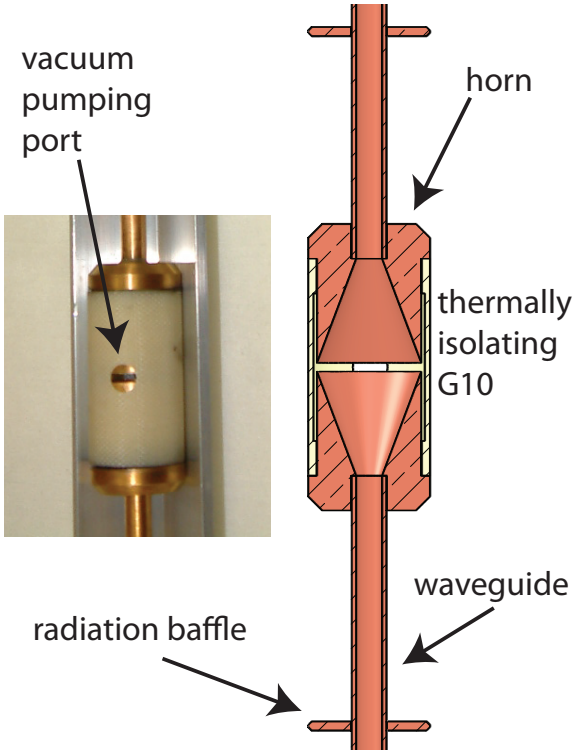

Figure 6.5: A photo (left) and a drawing showing the cross section (right) of a section of thermally isolating waveguide. Note that the hole in the G10 is to allow the waveguide to pump out more effectively as the IVC is evacuated.

After passing through the sections of waveguide, two teflon lenses help to focus the microwaves into a horn on the mixing chamber stage. These lenses have been modified from standard 50 mm diameter, 10 cm focal length teflon lenses from Thorlabs. Due to the tight space and the size of the clear shot ports (less than 1"), the lenses are carefully turned down to 1" diameter so that they can mount into standard 1" optics mounts (see figure 6.6). The lenses also act to block higher frequency room temperature radiation from getting to the experiment and heating the mixing chamber. We found that one lens mounted at the 1K pot and one mounted at the

ICP worked well to maximize the power arriving at the mixing chamber.

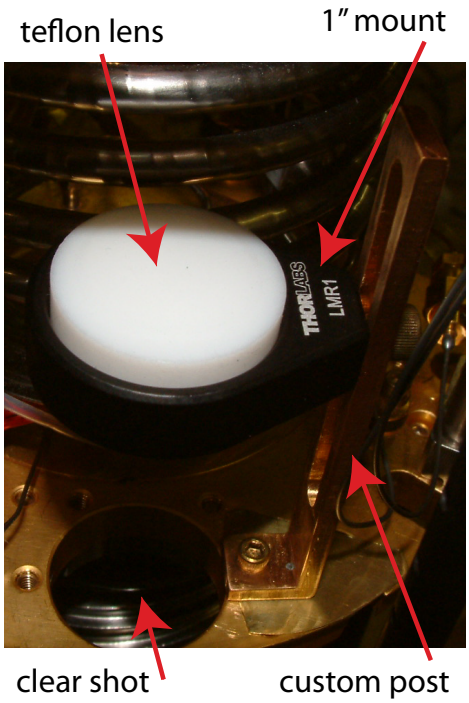

Figure 6.6: A turned down teflon lens mounted in a standard mount on a custom post on the ICP stage of the dilution refrigerator. Note that there is another lens mounted at the 1 K pot stage.

Once the microwaves have made it to the mixing chamber (with approximately 40 dB of attenuation, which reduces the room temperature radiative load), they pass through a silver waveguide and then through a sapphire window that makes an indium seal with the trap can. One more section of silver waveguide takes the microwaves to a small slit in the Penning trap, between the top endcap and the top compensation electrode. The amount of power that couples into the cavity, is, in general, a more complicated problem, and depends on the frequency of the microwaves relative to a cavity mode.

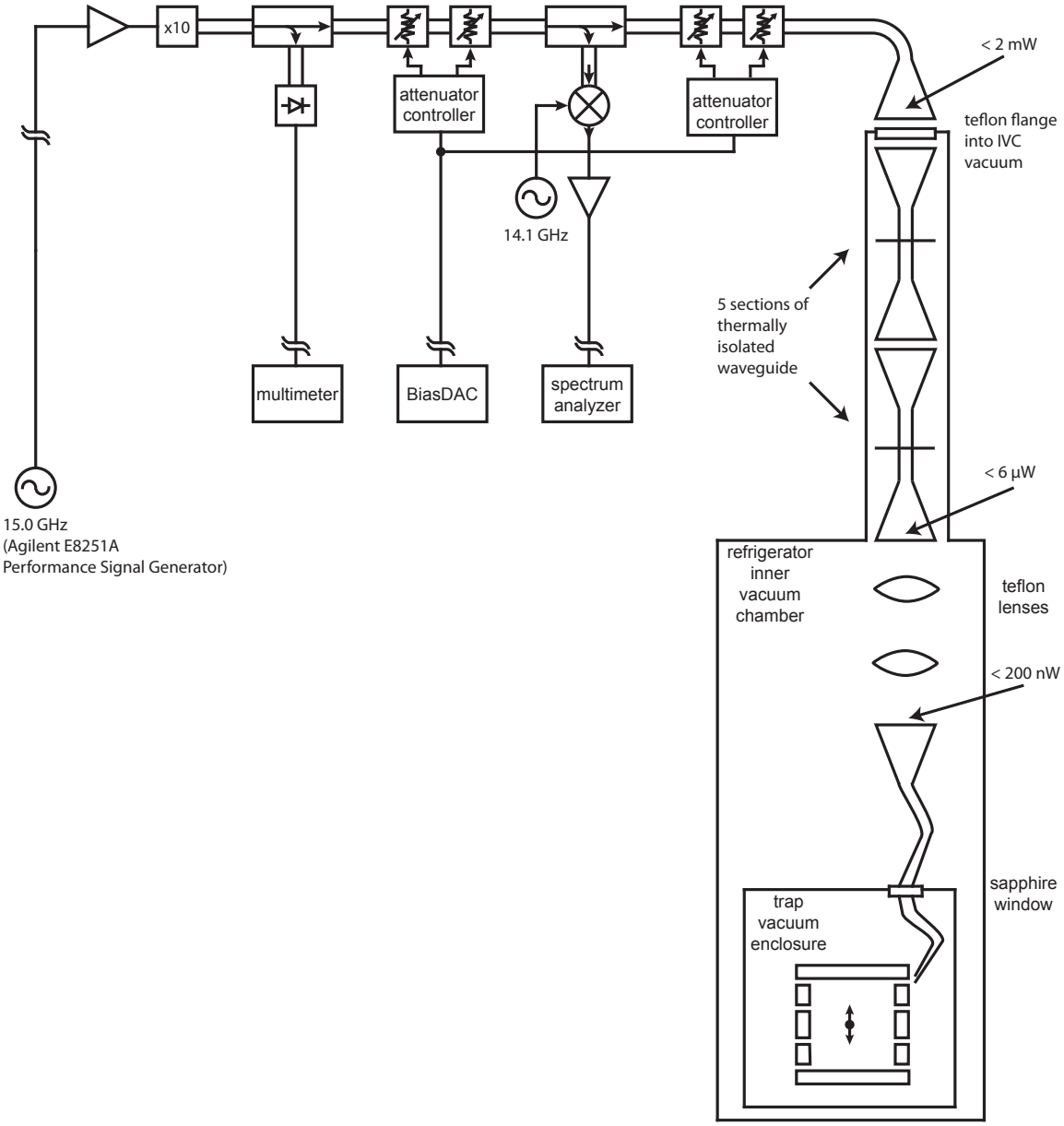

Figure 6.7: A schematic showing the path of the microwaves from the signal generator to the trap. In the microwave path, single lines represent cables and double lines represent waveguides. The figure also shows the microwave power available at various points throughout the system.

Chapter 7

Quantum Jump Spectroscopy of a Single Electron

The ultimate goal of our experiment is to improve the g-factor measurement for both the electron and the positron. To improve the precision of the measurement, we must improve upon what limited the precision of the previous measurement. For the 2008 g-factor measurement [2], the lineshape error was the primary source of error for the measurement, as is shown in table 7.1.

To reduce this error, we have commissioned a new apparatus designed to improve the magnetic field noise (chapter 3). We have also sought to decrease the error by narrowing the width of the cyclotron and anomaly resonances, by decreasing the size of the magnetic bottle in the new trap (see section 6.2). This chapter presents measurements taken using this magnetic bottle. These include measuring the cyclotron resonance for a cloud of electrons, a single electron, and with quantum jump spectroscopy of a single electron. The measurements confirm the reduced bottle size and

Table 7.1: Summary of uncertainties from the 2008 g-factor measurement. Note that the lineshape uncertainty is the primary source of uncertainty to improve upon for future measurements. Taken from [2].

ν_c / GHz =	147.5	149.2	150.3	151.3
g-value range	0.73	0.29	0.33	0.45
statistical uncertainty	0.39	0.17	0.17	0.24
correlated lineshape model uncertainty	0.24	0.24	0.24	0.24
uncorrelated lineshape model uncertainty	0.56	0	0.15	0.30

provide evidence that we are close to the stability necessary to make measurements with the reduced bottle size. The long cyclotron lifetime at this magnetic field is the first indication that we have inhibited spontaneous emission (see section 6.4) even though the cavity mode structure of the trap remains to be studied.

The cyclotron lineshape, measured with a single electron quantum jumps, illustrates using the size of the magnetic bottle to measure the axial temperature and sets a limit on the magnetic field drift.

7.1 Cyclotron Resonances in Electron Clouds

Before measuring a cyclotron line with a single electron using quantum jump spectroscopy, it is useful to initially find cyclotron resonances using a small cloud of electrons because the resonance of the single electron can be quite narrow.

After loading a small cloud of electrons, we apply a strong microwave drive to the electrons (as in section 6.5) near $\bar{\nu}_c$. The initial frequency of this drive can be chosen based on the magnet current, or more precisely, from NMR (see chapter 4). The strong drive excites the cyclotron motion of the cloud. Collisions within the cloud

of electrons or coupling due to non-quadratic terms in the potential distribute the cyclotron energy into the other motions in the trap, as well. For a strong enough cyclotron drive (we typically begin with 2 mW at the microwave multiplier for a new magnetic field setting), the energy added to the cloud can be detected as an axial response from the electrons. This bolometric detection technique [88] provides a response (≈1-5× the axial width) that can be measured on a spectrum analyzer with a wide (≈10-20× the axial width) frequency window. Figure 7.1 shows an example of the axial response of a small cloud of electrons for a single cyclotron drive frequency. Depending on the amount of heating from the microwave drive, the axial response of the cloud can be shifted a variable amount relative to the unheated cloud (as measured by a dip or a driven axial scan—discussed in chapter 5), which necessitates a wide spectrum analyzer frequency window.

In order to measure a cyclotron resonance from the broad response, one can sweep the microwave frequency through the cyclotron frequency. The integrated axial response (integrated over the points in a suitably chosen spectrum analyzer window), as the microwave frequency is swept, gives a lineshape for the cyclotron resonance. Figure 7.2 shows an example of an ≈1 MHz wide resonance for a small cloud of electrons.

Note that for high powers, the cyclotron responses can show quite a bit of hysteresis with respect to the direction of the sweep. This is likely due to the increased spread in magnetic field values that the electrons encounter as they are excited both axially and radially. Waiting $\approx 5{\gamma_z}^{-1}$ between excitation attempts at each microwave frequency helped to reduce hysteresis (by allowing the axial excitations to damp out),

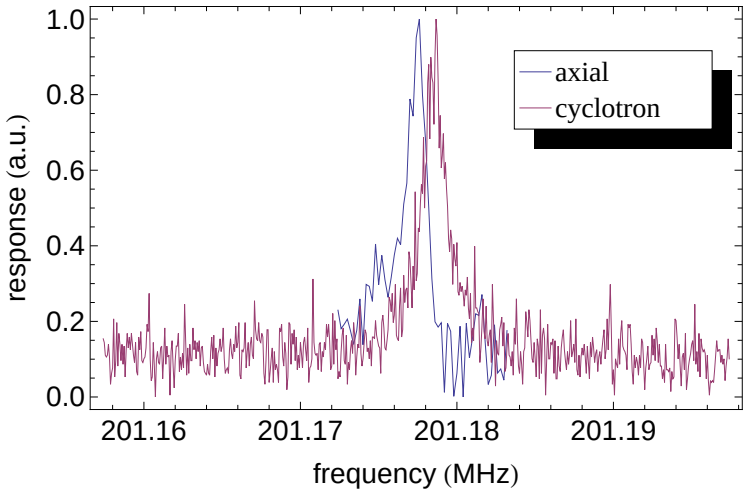

Figure 7.1: The axial response from a strong cyclotron drive applied at a single frequency (red). Here the microwave power is set to its maximum output of 2 mW (but is attenuated ≈40 dB by the time it reaches the mixing chamber). For comparison, a driven axial response (blue) for the same cloud, generated by sweeping an axial drive and measuring the response at each frequency (discussed in chapter 5). The cyclotron drive heats the cloud and shifts the axial response relative to the unheated cloud.

but did not completely eliminate it. The remaining hysteresis is likely due to sideband heating, and could perhaps be further reduced by cooling between each point.

In practice, however, this technique is most useful as a way to get an estimate of the cyclotron frequency for a single electron. Reducing the microwave power in the drive and the number of electrons in the cloud reduces the width of the cyclotron resonance, as can be seen in figure 7.3 as compared to figure 7.2. The width of the narrower resonance is ≈250 MHz and the single electron resonance was found within one linewidth of the cloud's response.

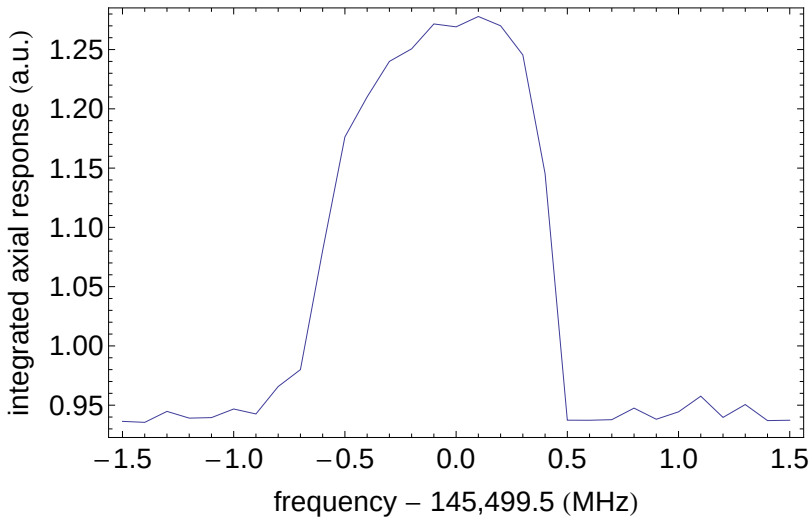

Figure 7.2: An example of a driven cyclotron resonance in a cloud of a few hundred electrons. For this method, the axial response is monitored over a 10 kHz window on the spectrum analyzer and integrated at each point. As the frequency of the microwave drive is swept, the integrated signal shows a resonance. Here the microwave power is attenuated ≈4 dB (attenuators at 0.5 V) from from its maximum output of 2 mW (plus an additional ≈40 dB passing through the dilution refrigerator).

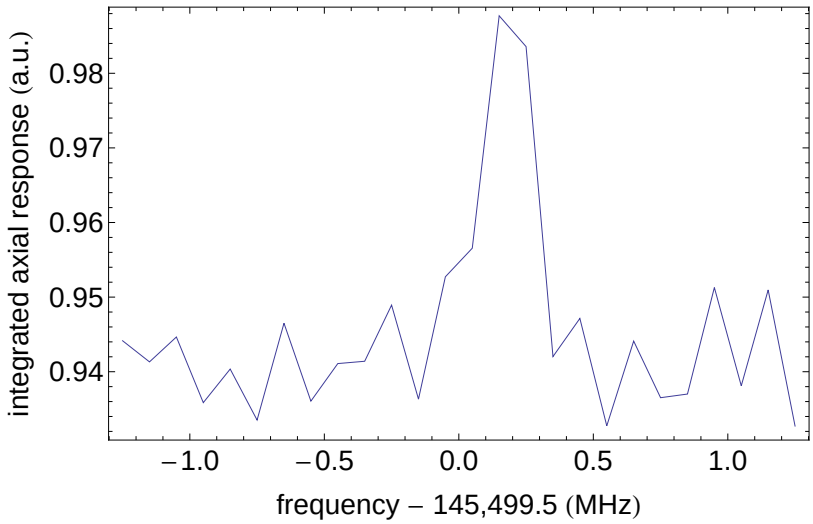

Figure 7.3: An example of a driven cyclotron resonance in a cloud of ≈100 electrons. Here the microwave power is attenuated ≈15 dB (attenuator at 0.8 V) from from it's maximum output of 2 mW.

7.2 Single Electron Quantum Jumps in a Smaller Magnetic Bottle

Once the cyclotron frequency is roughly known from the cloud's cyclotron resonance, we can measure the cyclotron excitations from a single electron. The procedure for driving single electron cyclotron transitions is quite different from the cloud technique described above. For a single electron, we use the self-excited oscillator (see section 5.5) to monitor its axial frequency. We then apply a frequency near $\bar{\nu}_c$ and look for a shift in the axial frequency. For an electron, we always begin in the $|0,\uparrow\rangle$ state, as seen figure 6.2 (prepared by applying resonant cyclotron and anomaly drives).

To initially find a response, a high microwave power is used to broaden the cyclotron line and make the resonance easier to find. With the axial detection amplifiers on and while monitoring the axial frequency with the self-excited oscillator (see chapter 5), we apply a strong cyclotron drive to drive excitations to n $\geq$ 3 (see figure 7.4). These excitations quickly decay down, as the lifetime of the excited states gets shorter and shorter for increased n (equation 2.99 in [11]). These quantum jumps to much higher cyclotron states will lead to a broadened out cyclotron line, as in figure 7.5. This lineshape was built up using the procedure outlined below, except that the self-excited oscillator is left on during the scan, which also helps to broaden out the observed response. The power is then reduced until no excitations above n=1 are observed.

Observing these single quantum jumps confirms that a single electron is trapped (as was indicated byt the width of the response to an axial drive). If there were two

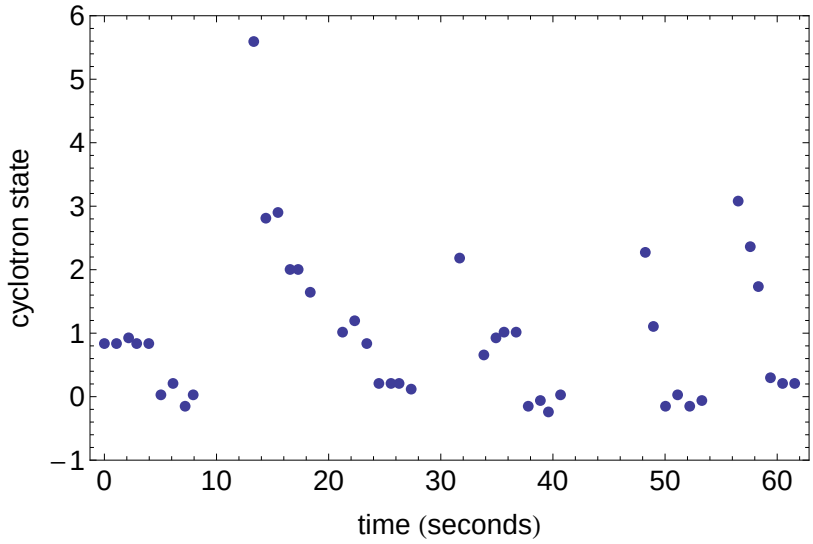

Figure 7.4: Some of the first driven excitations of the cyclotron state in the new, smaller magnetic bottle. These excitations, which are driven with a high microwave power and with the self-excited oscillator left on, are excited into n $\geq$ 3 states, which quickly decay down. Notice that the discrete nature of the decays is immediately discernable.

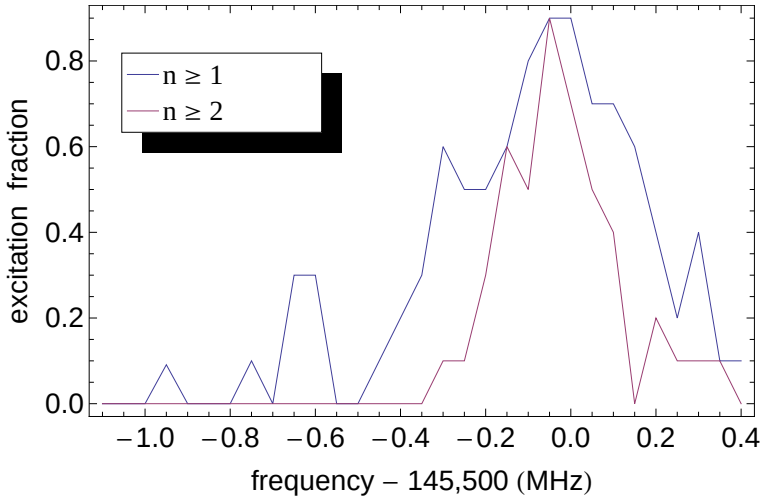

Figure 7.5: A power broadened cyclotron line from a single electron. The higher curve (blue) shows the excitation fraction into n $\geq$ 1, while the lower curve shows the excitation fraction into n $\geq$ 2. Note that the peak excitation fraction is nearly 100% on resonance and that the width of the line is $>$ 0.5 MHz. This makes the feature very easy to find after finding the resonance of the electron cloud.

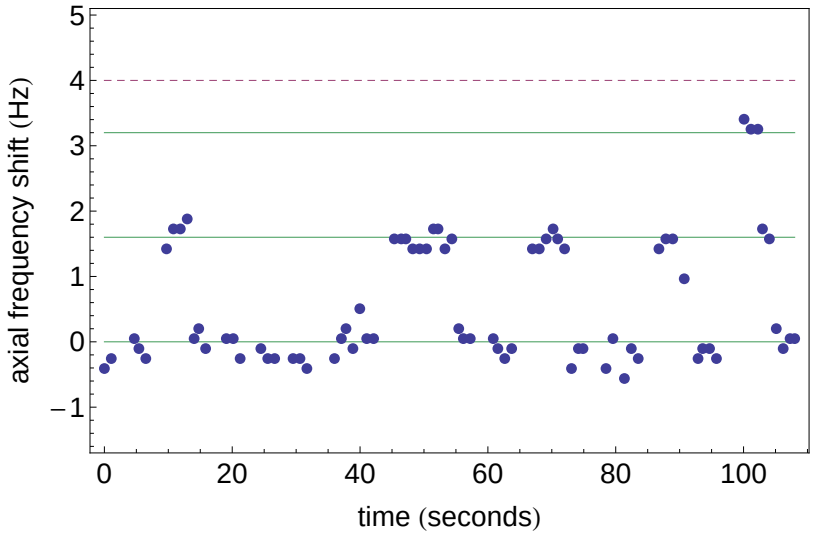

Figure 7.6: Several driven excitations of the cyclotron state in the new, smaller magnetic bottle. The last excitation includes a jump up to n=2, further showing the discrete nature of the jumps, but indicating that the microwave power is still too high. The dashed line shows the shift from the larger magnetic bottle of the 2008 g-factor measurement for comparison.

electrons in the trap, the axial shift would only be half of the expected value (since the axial shift scales as 1/m, as in equation 6.7, reproduced here).

$$\frac{\Delta\omega_z}{\omega_z} = \frac{2\mu_B B_2(\frac{1}{2} + n + \frac{g}{2}m_s)}{m\omega_{z0}^2} \tag{6.7}$$

The calculated magnetic bottle size ($B_2 = 658\ T/m^2$) is in good agreement with the measured magnetic bottle size. By averaging over several cyclotron excitations and decays in the magnetic bottle (the discrete jumps seen in figure 7.6) and extracting a frequency shift, we can use equation 6.7 (reproduced above) to calculate the strength of the bottle. In doing this, we measure a magnetic bottle of $622 \pm 66\ T/m^2$, where the error bars come from the the standard deviation in axial shift sizes. The precision of the measured magnetic bottle strength does not affect the g-factor precision—it must only be known precisely enough to determine the threshold for detecting the

axial shift caused by a cyclotron excitation.

The fact that we can easily observe cyclotron excitations in the first excited state tells us that the lifetime of the state is already long enough to perform a measurement, even before we tune the cyclotron frequency to choose the lifetime. Figure 7.7 shows the distribution of lifetimes of individual cyclotron excitations in the trap. This distribution fits to an exponential, and we can extract a decay time, which is the cyclotron lifetime for this magnetic field at a particular self-excited oscillator amplitude. Previously, it was found that the cyclotron lifetime varies as a function of the electron's amplitude [13, 101]. This is expected, as the increased amplitude modulates the coupling between the cyclotron frequency and a cavity mode (see [101]). In order to measure the zero amplitude lifetime, lifetimes at several amplitudes of the self-excited oscillator can be measured and fit to extract the zero amplitude lifetime [13, 101].

The fit lifetime is 2.71 ± 0.17 seconds. This is more than 28 times the free space value of the cyclotron lifetime. This preliminary lifetime measurement is our first evidence that the cavity mode structure is as designed. Namely, by choosing $\bar{\nu}_c \approx$ 145.5 GHz, we have chosen a cyclotron frequency which is far from any cavity modes, which is consistent with the cavity mode structure from figure 6.4.

7.3 Quantum Jump Spectroscopy

We can now use an automated procedure to build up a lineshape using quantum jump spectroscopy. We apply a microwave drive frequency near $\bar{\nu}_c$ and look for a cyclotron excitation (from $|0,\uparrow\rangle \rightarrow |1,\uparrow\rangle$) as indicated by the axial frequency shift of

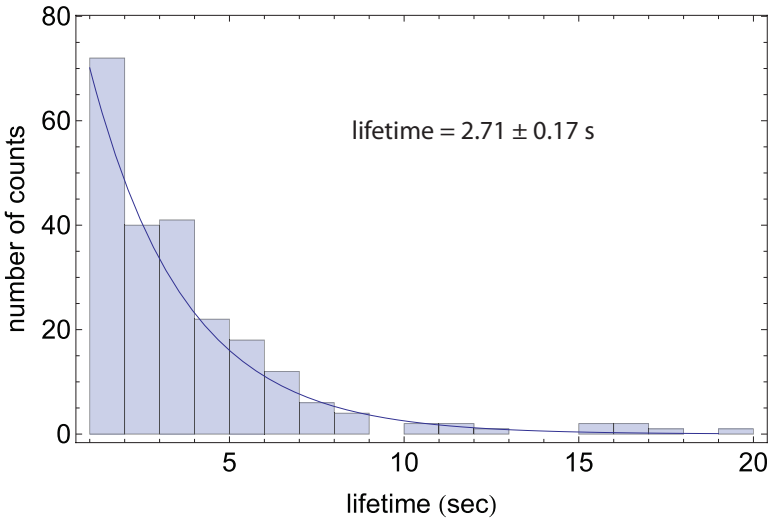

Figure 7.7: A histogram of the lifetime of many individual cyclotron excitations (bins) overlaid with an exponential fit (curve). The fit curve has a lifetime of 2.71 $\pm$ 0.17 seconds. This long cyclotron lifetime (over 28 times the free space value–see table 2.2) is evidence that the cyclotron frequency is very far from a cyclotron coupling mode, as we would expect from the trap design.

equation 6.7. By stepping the drive frequency through a set of discrete frequencies (spaced by roughly 1/10 of the expected linewidth) and recording a histogram of the excitation fraction at each frequency, we can trace out the cyclotron resonance. The procedure for the 2008 g-factor measurement is outlined below:

1. Establish the ground state with the self-excited oscillator by measuring the unshifted axial frequency.

2. Turn the self-excited oscillator off and the magnetron cooling drive on.

3. Wait 0.5 s so that the for the self-excited amplitude to damp out.

4. Turn the amplifiers off. Wait 1.0 s for the amplifiers to cool down.

5. Turn the magnetron cooling drive off. Wait 1.0 s for the axial oscillations damp out.

6. Apply a cyclotron drive near $\bar{\nu}_c$ and a detuned anomaly drive for 2.0 s.

7. Turn the amplifiers and self-excited oscillator back on. Wait 1.0 s for the self-excited oscillator to stabilize.

8. Trigger the computer data-acquisition card (DAQ) to measure the axial frequency.

The DAQ reads continuously and LabVIEW Fourier Transforms the data over a predetermined averaging time. If there is axial frequency shift that is consistent with a cyclotron jump, the program records a successful drive attempt and lets the cyclotron excitation decay before restarting the process at a new microwave drive

frequency. When the scan frequency hits the end of the scan window, it restarts at the beginning of the window. A very similar procedure exists for measuring the anomaly frequency (which will be discussed in chapter 8).

Though this is the procedure for taking g-factor cyclotron data, the preliminary lineshape presented in this chapter was taken using a slightly different procedure:

1. Establish the ground state with the self-excited oscillator.
2. Turn the self-excited oscillator off and the magnetron cooling drive on. Wait 0.5 s.
3. Turn the magnetron cooling drive off. Wait 0.5 s for the axial oscillations damp out.
4. Apply a cyclotron drive near $\bar{\nu}_c$ for 0.5 s.
5. Turn the self-excited oscillator back on. Wait 1.0 s for the self-excited oscillator to stabilize.
6. Trigger the computer data-acquisition card (DAQ) with a 1.0 s averaging time.

The main difference between this procedure and the g-factor cyclotron procedure is that the amps are left on during the excitation attempt. Though this is not ideal (it increases the axial temperature of the particle during the cyclotron excitation), at this early stage, it was found to be necessary to achieve the desired stability of the axial frequency in order to measure quantum jumps with near unit accuracy.

Initial attempts to take a lineshape following the 2008 procedure proved unsuccessful. As the amplifiers were toggled on and off, a downward shift of a few Hz

in the axial frequency was observed upon turning back on the self-excited oscillator. The frequency recovered to the initial axial frequency with a timescale of a few seconds, but the dip in frequency often masked any cyclotron excitations, whose lifetime are also only seconds long. For the final measurement, where the lineshape will be measured with the amplifiers off, this stability will have to be improved to the level achieved for the 2008 measurement.

Still, the cyclotron lines measured below are the first experimental confirmation that we have the stability in the apparatus to measure cyclotron resonances in the new, smaller magnetic bottle with the self-excited oscillator off. Using the procedure outlined above, we can build up such a resonance, which can be seen in figure 7.8. This data is the combination of 3 data sets taken over 22 hours and 50 minutes. The microwave power was chosen such that the excitation fraction is $\approx 25\%$. At this magnetic field, the microwave drive was attenuated ≈ 80 dB (3.1 V on the attenuators) from the microwave multiplier's maximum output of 2 mW.

In order to correct for magnetic field drift over the course of a night, the previous version of the experiment regularly monitored the magnetic field by using the electron itself as a magnetometer [12, 2]. By measuring the frequency of the sharp cyclotron edge over the course of the night, the magnetic field drift could be removed from the final data. See figure 7.9 for an example of this field drift and how the data is adjusted. The data in figure 7.8, taken over the course of nearly 23 hours, has no magnetic field correction.

By comparing these two figures, we can see that the field drift over the course of this measurement is less than for the night of data shown in figure 7.9, which

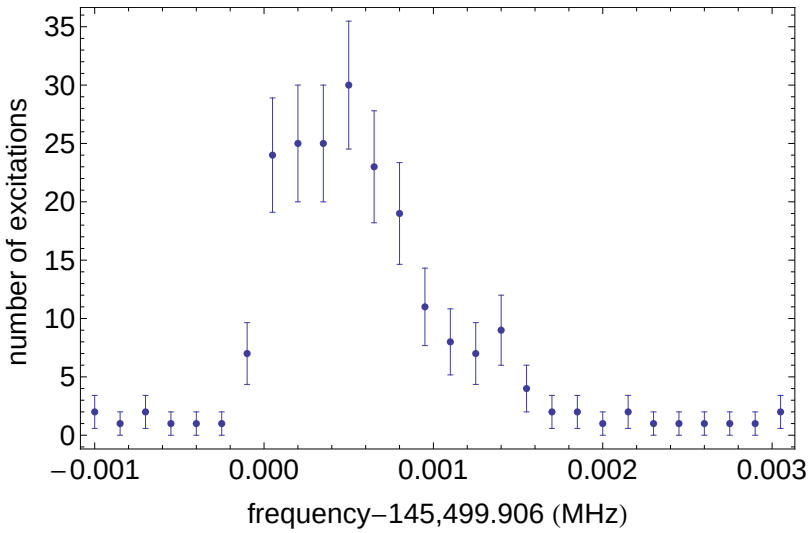

Figure 7.8: A lineshape built up from several attempts at driving single electron, single cyclotron jumps. Note that this data is from several runs performed over the course of nearly a day and combined with no magnetic field correction. The microwave power is attenuated from it's maximum 2 mW by ≈ 80 dB (3.1 V on the attenuators). The zero on the graph is only chosen to approximately line up with the lineshape's edge.

showed a somewhat high field drift of 0.6 ppb/h drift over the course of the night ($\approx$ 14 hours). Thus, our cyclotron lineshape gives us reasonable evidence that the magnetic field drift is lower in the new magnet, since the absolute field drift is lower for our measurement even when measured over a longer time. For example, if we were to naively attribute the entire width of the cyclotron line (just under 1 kHz) to magnetic field drift, this would still only be a magnetic field drift of < 0.3 ppb/h. The actual fiield drift is likely much less than this naive upper bound, and is certainly low enough for a g-factor measurement—at least at the precision of the 2008 measurement.

We can also use the information from the cyclotron lineshape to measure the axial temperature of the electron. From the expected lineshape in the cyclotron limit (see section 6.3), we expect to measure a sharp cyclotron edge followed by a decaying

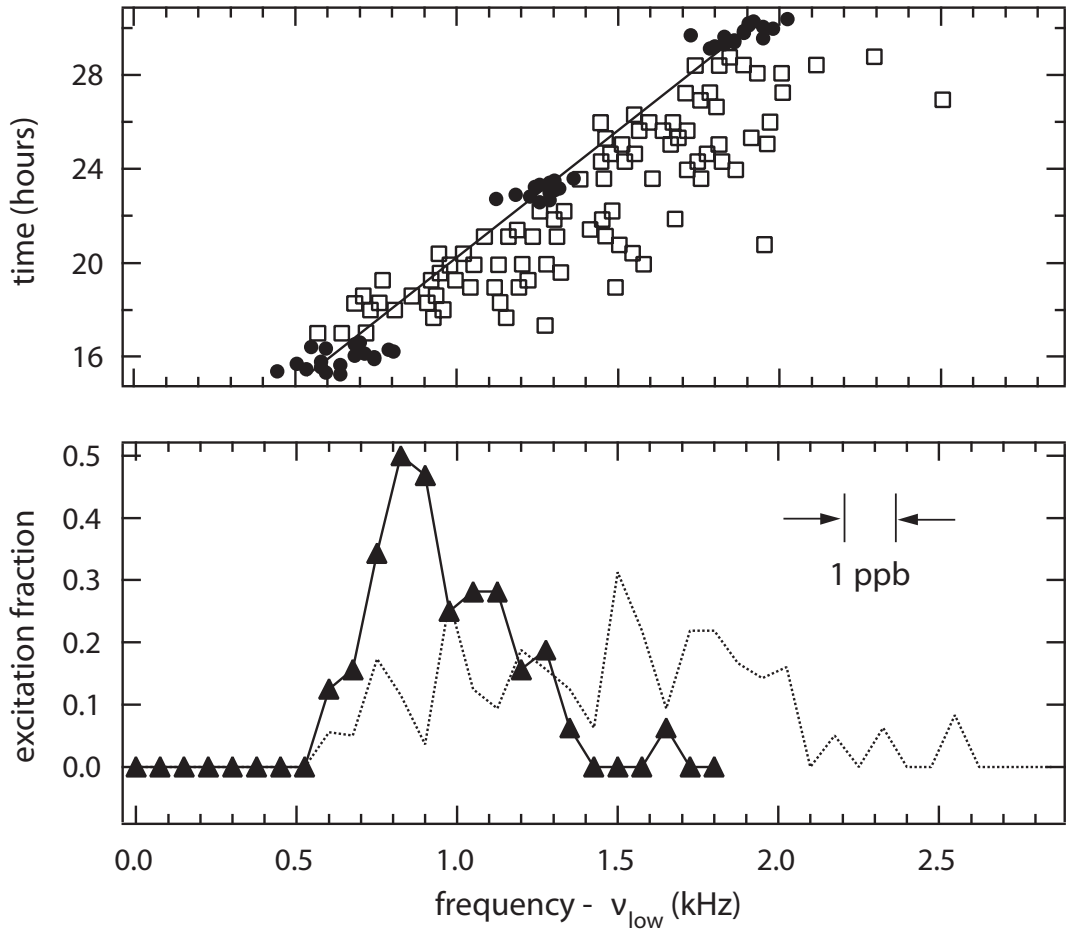

Figure 7.9: The upper plot shows edge tracking points (points) with fit (line) and cycltotron points as measured (squares). The lower plot shows the uncorrected (dotted line) and corrected (triangles) cyclotron lines. Figure taken from [102].

exponential. As is shown in equation 6.9, the width of the exponential decay depends directly on the axial temperature of the electron. The data from figure 7.8 appears to show the expected sharp turn on and decay [11]. If we perform a simple exponential fit to the data, we see that the temperature fits to 5.33 K $\pm$ 0.95 K, though this may overestimate the temperature, as we have not removed any magnetic field drift from the resonance.

Even though the amplifiers are at a higher power, this measurement of the axial temperature with the amps on is in good agreement with the amps on temperature measured in the previous experiment (5.17 ± 0.5 K [103, 81]). Of course, the feature is narrower in its absolute frequency width by the factor of the smaller bottle size, which provides evidence that the smaller bottle will narrow the lines as expected. However, if some other mechanism is broadening out the lines at a lower level (for example, higher frequency magnetic field noise), this could prevent the lines from narrowing up in the amps off cyclotron lineshape. This will have to be investigated. All of the above data was taken with the helium reliquifier on. It remains to be investigated whether or not the vibrations from the reliquifier will broaden or shift the cyclotron resonance, but the shape and width of this initial lineshape are encouraging that any effects might be small.

As a final note on the discussion of stability, it is worth mentioning the instability of the magnet after a cryogen fill. As was discussed in chapter 3, the increased hold times for the cryogens, as well as the addition of the reliquifier, reduce the necessity of stability disrupting fills. In order to see if the stability of the measurement would be disrupted in the new magnet, a cyclotron lineshape was measured before a helium

fill, just after a helium fill and the day after a helium fill. Immediately after the fill, the cyclotron line was found to shift down in frequency ≈ 15 kHz, but recovered within 1 day after the fill. This suggests that the pressure and temperature changes associated with filling the helium reservoir also negatively affect the magnetic field stability in the new magnet, and g-factor data should still be avoided for the day after the helium fill.

7.4 Summary

We have performed quantum jump spectroscopy of a single electron in an entirely new apparatus with a newly designed Penning trap and a smaller magnetic bottle. The observed quantum jumps confirm the size of the magnetic bottle, as well as providing a measurement of the cyclotron lifetime in the trap cavity at this magnetic field. The lifetime demonstrates the inhibition of spontaneous emission consistent with the designed cavity mode structure. By building up a cyclotron lineshape, we are able to measure the axial temperature of the electron and place limits on the magnetic field drift.

Chapter 8

Future Directions and Conclusions

Throughout this thesis, we have described the installation and preliminary measurements in a new, high stability apparatus. The apparatus has several advantages over the one in which the most precise electron g-factor was measured, which we hope will lead toward an improved electron/positron g-factor comparison. Firstly, it has the space for a positron source, which will allow for a positron g-factor measurement. We have installed a positron source and have demonstrated positron loading into a secondary loading trap.

The new apparatus also has fewer but larger cryogen spaces, which drastically reduce stability disrupting fills. In addition, we have installed a complete helium recovery system so that the Dewar and dilution refrigerator can run with minimal losses during the course of a measurement. We have demonstrated that we can run loss free for > 1 month, which is long enough to take g-value and systematic data at a given magnetic field.

Our magnet and dilution refrigerator are designed to provide better mechanical

stability between the trap and the magnet. In addition, the magnet is equipped with a more comprehensive set of shim coils. We have demonstrated the low-temperature ^{3}He NMR necessary to measure and shim the field more precisely than was demonstrated in the 2008 g-factor measurement. Though some rotational variations to the ^{3}He probe remain, it remains to be determined if these are large enough to broaden the electron's resonances.

We have also installed a new cylindrical trap in which to take the g-factor data. The trap has a mode structure which should allow us to take advantage of axial sideband cooling modes while avoiding cyclotron coupling modes. Additionally, it has a smaller (by 2.3 times) magnetic bottle, which should allow for narrower cyclotron and anomaly lines.

Within this new apparatus, we have demonstrated the ability to load and detect a single electron. We have used the self-excited oscillator to demonstrate that we have the axial stability to measure single quantum cyclotron excitations in the smaller magnetic bottle (with the detection amplifiers on). From this quantum jump spectroscopy, we have measured and confirmed the size of the magnetic bottle, placed limits on the stability of our superconducting solenoid and measured a cyclotron lifetime at one magnetic field. This lifetime measurement demonstrated spontaneous emission inhibited by > 28 times its freespace value, which suggests that the cavity mode structure may be as it was designed, though a more detailed measurement must be done to be sure.

This chapter will focus on the future direction of the experiment. It will cover the steps necessary and the procedure for making an improved electron g-factor mea-

surement. It will also cover the positron g-factor, including the proposed scheme for transferring positrons between the loading trap and the precision trap. Finally, it will discuss the possibility of axial sideband cooling, a technique which could improve the g-factor even further for both the electron and the positron by reducing the axial quantum number.

8.1 An Electron g-Factor Measurement

There are several steps to take before making an improved electron g-factor measurement. These will include measuring the modes of the cavity, improving the axial stability so that quantum jump spectroscopy can be performed with the amplifiers off, measuring the cyclotron and anomaly lineshapes at several magnetic fields, and then checking for other systematics.

Before choosing the magnetic fields at which to take the g-factor data, we will need to know precisely where the modes of the precision trap are. Ideally, we will take data near the 3 cooling modes shown in figure 6.4. To find these modes (and to make certain that they are far from the cyclotron coupling modes), we can map out the cavity using a parametric mode map (see section 6.4). Initial work has already begun on taking parametric mode maps of the cavity.

Once these mode locations have been roughly determined with the parametric mode map, lifetime data from a single electron or positron will be used to map out the nearby modes more precisely. As discussed in chapter 7, we have already taken an initial cyclotron lifetime measurement with a single electron, but several more lifetimes will have to be measured at various magnetic fields, interspersed with the

g-factor data, in order to map out the nearby cyclotron coupling modes well enough to apply the cavity correction.

As discussed in chapter 1, the experimentalist's g-factor requires several measurements: the cyclotron frequency, the anomaly frequency, the axial frequency, the cavity correction and the special relativitistic correction. In order to measure the cyclotron and anomaly frequency, we will need to perform quantum jump spectroscopy for each of these resonances with the detection amplifiers off. As discussed in chapter 7, the stability of the axial frequency with respect to turning on and off the detection amplifiers will have to be improved. Once the desired stability is achieved, the cyclotron and anomaly lineshapes can be measured in the same manner as in the 2008 measurement. The procedure for measuring the cyclotron lineshape has already been laid out in chapter 7.

To drive the anomaly transition, we need to drive a simultaneous spin flip and cyclotron transition. To get the necessary oscillating transverse magnetic field to flip the spin, we drive the electron axially in the $z\rho\hat{\rho}$ gradient of the magnetic bottle. The anomaly frequency is $\approx$170 MHz, which is in the radio frequency regime, so we apply an oscillating voltage to the bottom endcap using a frequency synthesizer. The necessary magnetic field can also be generated by splitting the trap electrodes (both compensation electrodes, for example) and driving each half with opposite currents [11, 104]. The 2008 g-factor measurement exclusively used technique of driving the electron through the bottle gradient. The procedure for measuring the anomaly frequency is outlined below:

1. Establish the ground state with the self-excited oscillator by measuring the axial

frequency.

2. Turn the self-excited oscillator off and the magnetron cooling drive on. Wait 0.5 s.

3. Turn the amplifiers off. Wait 1.0 s.

4. Turn the magnetron cooling drive off. Wait 1.0 s for the axial oscillations damp out.

5. Apply an anomaly drive near $\bar{\nu}_a$ and a detuned cyclotron drive for 2.0 s.

6. Turn the amplifiers and self-excited oscillator back on. Wait 1.0 s for the self-excited oscillator to stabilize.

7. Trigger the computer data-acquisition card (DAQ).

For the anomaly, we also always begin in the $|0,\uparrow\rangle$ state. We then apply the a drive near the anomaly frequency in attempt to drive a transition into the $|1,\downarrow\rangle$ state. Unfortunately, we cannot resolve the small axial frequency shift from the anomaly transition (which would be <2 mHz in our magnetic bottle). Instead, we must detect the transition from $|1,\downarrow\rangle \rightarrow |0,\downarrow\rangle$ as the cyclotron state spontaneously decays. If this transition is detected, the anomaly transition is considered a success. The state is then prepared back into the $|0,\uparrow\rangle$ state by applying resonant cyclotron and anomaly drives.

In order to declare the attempt a failure, we must observe the absence of the cyclotron decay. To detect this spontaneous process with near unit fidelity, we must

wait several cyclotron lifetimes. As the cyclotron lifetime is several seconds, this process takes quite some time and is the rate limiting step in measuring the g-factor. By stepping through the anomaly frequency and repeating, we can build up a histogram of successful anomaly transitions, and in this manner, sweep out the anomaly lineshape, which can be used to determine the anomaly frequency.

We will also need to know the axial frequency in our expression for the g-factor. To affect the g-factor at less than 0.1 ppt, the axial frequency must be known within 10 Hz. The axial frequency is measured by looking at frequency of the single electron dip with the detection amplifiers on. The actual axial frequency of interest is the frequency when the amplifiers are off (when the anomaly and cyclotron transitions are driven), but the shift from the thermal amplitude is neglible at the 10 Hz level as are the other small axial shifts (from the frequency pull of the amplifier or the anomaly drive power) [13].

Given that the apparatus and trap are completely new, several systematic checks will likely have to be performed before a believable g-factor value can be arrived upon. One check we have already discussed—measuring the g-factor at several magnetic fields. This will confirm the cavity measurements and corrections, and search for any other magnetic field related systematics. For example, we will be able to search for the axial temperature variation at different magnetic fields that was seen in the previous data.

In the previous apparatus and trap, power systematic checks were performed for both the cyclotron and anomaly drives. The results of these systematics are shown in figure 8.1 [13]. For the cyclotron line, a resonance was measured with the usual power,

one with double the anomaly power, and one with half of the cyclotron power. The cyclotron power was halved rather than doubled to avoid power broadening effects. For the anomaly lineshape, a resonance was measured with the usual power, double the anomaly power, and double the cyclotron power. The results are reasonably consistent with zero (though the anomaly measured with double the cyclotron power is $\approx 3\sigma$ away from zero), and are limited by the time it takes to resolve the lines. For the new traps and for a higher precision measurement, these power systematics will have to be repeated with more statistics to confirm that they will not limit the measurement.

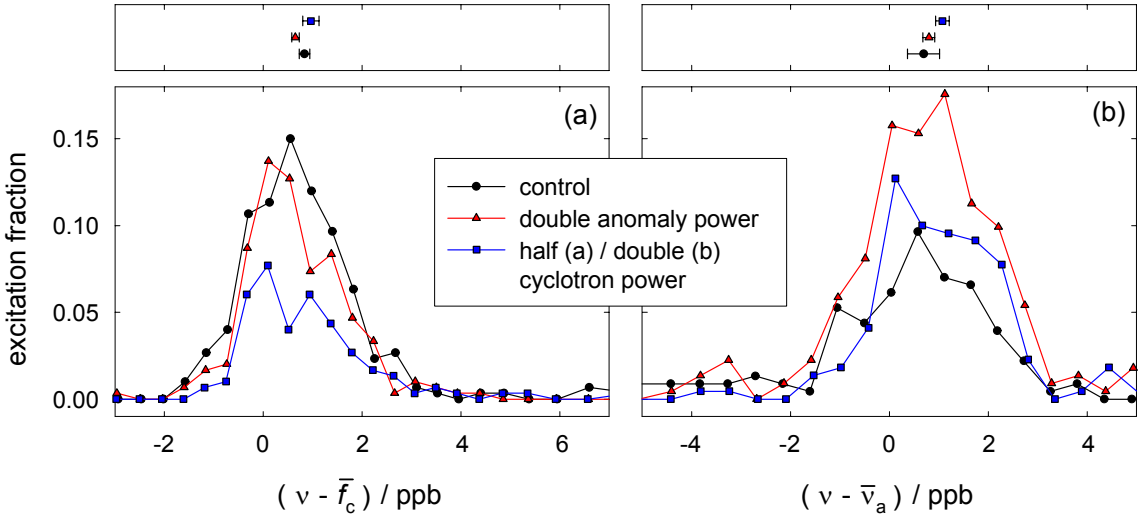

Figure 8.1: The power systematics from the previous g-factor measurement. Figure taken from [13].

8.2 Axial Sideband Cooling

The primary broadening mechanism of the cyclotron and anomaly lineshapes is the coupling of each of these motions to the axial motion via the magnetic bottle.

Throughout this thesis, we have focused on reducing the size of the magnetic bottle as a way to narrow up the lines and hopefully improve the precision with which we can determine these frequencies. There is another way to narrow the lineshapes, however, which is to reduce the temperature of the axial motion.

One possible way to do this would be to run the dilution refrigerator at a lower temperature. With our higher power dilution refrigerator, this is a possibility, which may be worth trying. The measured axial temperatures, however, have always been above the setpoint of the mixing chamber [13, 103, 90], and it is unclear if slightly lowering the mixing chamber temperature would actually significantly reduce the axial temperature for our typical measurement cycle.

A more promising technique might be to attempt cavity-assisted axial sideband cooling [11], in which we would apply a microwave drive at $\nu_c^{'} - \nu_z$. In a manner similar to our magnetron cooling (see chapter 2), this drive will heat the cyclotron motion and cool the axial motion (by driving $|n, k\rangle \rightarrow |n+1, k-1\rangle$). Just as for the magnetron cooling, the cooling limit will be equal quantum numbers (in this case, $n = k$), which means that, in principle, we should be able to cool the axial state to its ground state (since the cyclotron state will continually damp radiatively to its ground state).

Axial sideband cooling was attempted in the previous trap but without success. Even after 15 minutes of cooling, the cyclotron state still remained in an excited state [101], which was attributed to a slow cooling rate. As discussed in chapter 6, the goemetry of the trap was such that it lacked cooling modes that were located away from cyclotron coupling modes. Cooling was attempted at 147.5 GHz, nearly

30 linewidths away from the nearest cooling mode at 146.4 GHz (TE_{136}).

Driving the sideband near a cooling mode can increase the rate for two reasons. First, the power coupling into the trap significantly increases when the frequency is near a cavity mode [101]. In addition, the modes that have the appropriate geometry to couple the axial and cyclotron motions (electric fields that vary as $z\hat{\rho}$ or $\rho\hat{z}$) can also increase the rate by a geometric factor [101] over a simple plane wave. These two factors combined should allow for much enhanced cooling rates in the new trap, which makes axial sideband cooling an exciting possibility.

There are, however, a few challenges remaining associated with axial sideband cooling. In order to actually cool the axial motion, the electron cannot be thermally anchored to the detection electronics. Otherwise it will rethermalize with the damping timescale discussed in chapter 5. Instead, the electron will have to be decoupled from the amlpifier. One way to do this is by adjusting the potential on the endcaps to bring the electron out of resonance with the amplifier, but this poses a few challenges of its own.

Firstly, the axial frequency shift away from the amplifier must be known very precisely (again, to better than 10 Hz) since we need to know the axial frequency for the g-factor determination and to apply the correct frequency for the sideband drive. Further, our current method of determining whether or not a cyclotron excitation has occurred is to detect the small axial shift (1.7 Hz) in the magnetic bottle. In order to see this, we would have to shift the axial frequency back to the "ground state" axial frequency with a precision of much less than axial shift in the bottle. For these reasons, a more appealing option would be to decouple the detection electronics from

the electron without shifting the potential.

8.3 A Positron g-factor Measurement

A positron g-factor measurement will entail all of the same steps as we laid out for the electron g-factor. First, however, we will need a single positron in the precision trap. As discussed in chapter 5, we have demonstrated robust loading of positrons into the loading trap. The next step in the process is to transfer the positrons to the precision trap. As many experiments have demonstrated (for example, [105, 106]), it is possible to transfer particles slowly (compared to axial and magnetron frequencies) between trap electrodes. Though this type of transfer is possible within the loading trap stack, it has thus far failed to be able to transfer positrons into the precision trap.

The difficulty is the very small diameter (0.010") hole in the top endcap electrode of the precision trap. As the particles are slowly transferred in a shallow well, they are magnetron heated [107], which drives them to larger and larger radii. This, plus any misalignments between the axis of the hole and the magnetic field lines, will cause the particles to collide with the electrode rather than passing into the precision trap.

There is good reason to believe that misalignment of the traps is not the culprit. If we fire the FEP, we can monitor its current through a 1 MΩ resistor (see figure 5.5). With an electrometer set up to measure current, we can also measure the current hitting any electrode of our choice. By monitoring the current on the tungsten moderator (at the top of the loading trap), we see that $> 90\%$ of the current from the FEP is hitting the moderator. Since the FEP is behind the small hole in the

bottom endcap, and since the electrons must follow the magnetic field lines, the traps must be well aligned for the electrons to pass through both both the bottom and top endcap and make it to the moderator.

To circumvent magnetron heating during a slow transfer, we can, instead, pulse the particles rapidly through the hole. Rapid transfer has been shown previously to transfer positrons between hyperbolic traps with a similarly small hole in the endcaps [9] and to transfer positrons rapidly past an irregularly shaped ball valve [108, 109]. Our transfer scheme will follow the method developed for the ball valve [109]. In this scheme, we would hold the particles in a raised well, rapidly drop the sides of the well to throw the positrons, then catch the positrons in the precision trap in a similar well. An example of this is shown in figure 8.2 for our electrodes.

For the voltages in figure 8.2, we estimate the transit time of the positrons to be $\approx$30 ns, which means that we will need to change the voltages on the electrodes on the nanosecond timescale. Our typical filtering (see chapter 5) decreases the noise on each electrode by using a lowpass RC filter with a time constant of 0.1 seconds. This means that we cannot pulse the particles by simply changing the bias on the electrodes via our standard biasing line (unless we were willing to give up this filtering). Instead, we have installed separate lines, which are capacitively coupled to the top endcap and the loading bottom endcap. The schematic for the transfer line is shown in figure 8.3.

The original timing of the pulse is generated by a Stanford Research Systems DG535 Digital Delay/Pulse Generator, which feeds into an AVTECH AV-143A saturated switch. The saturated switch amplifies the voltage by 2.5 (with a maximum output of 10 V). The network or resistors and capacitors at room temperature im-

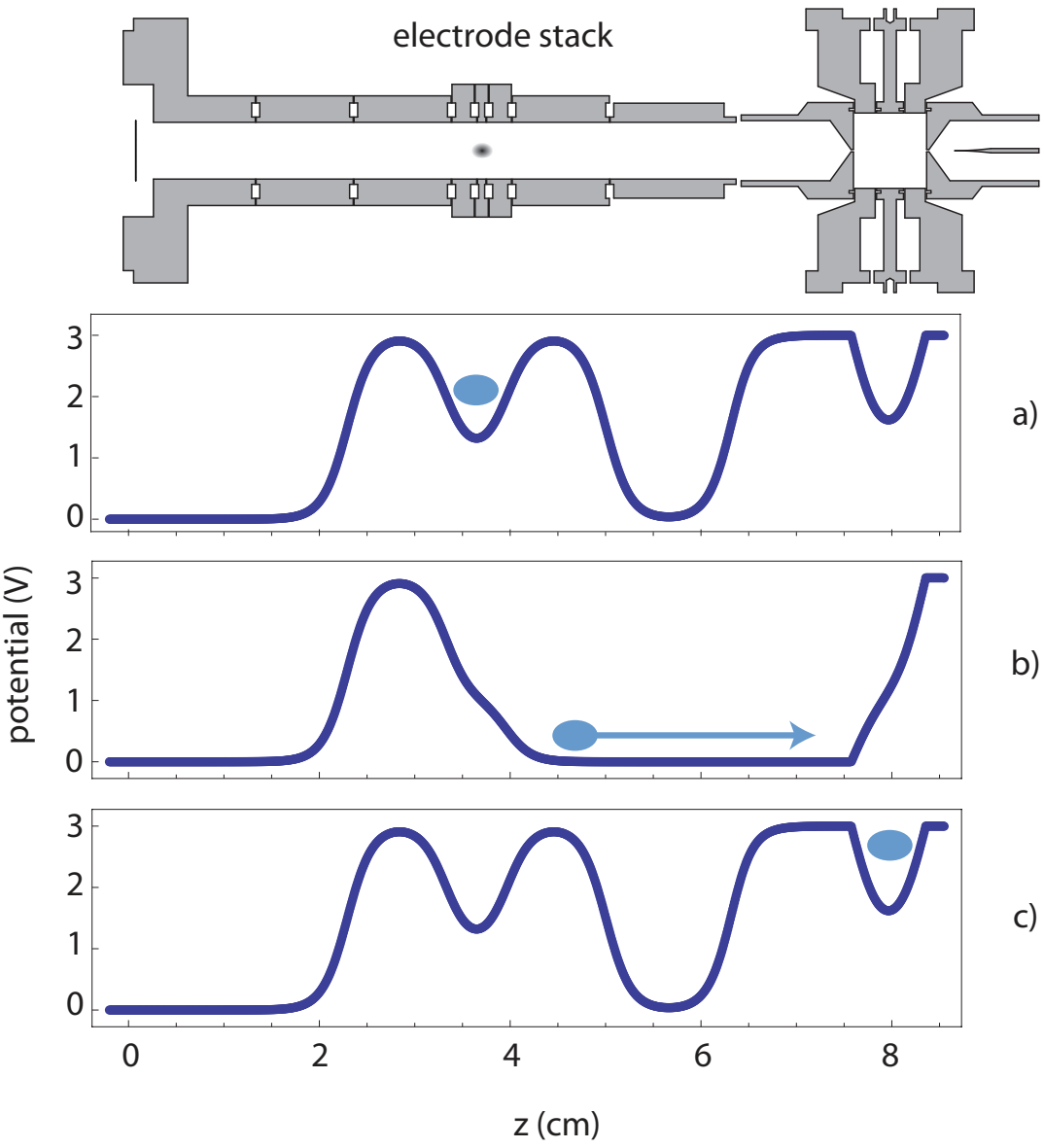

Figure 8.2: The transfer sequence for positrons: a) the positrons are held in a raised well in the loading trap and there is a similar well in the precision trap, b) the sides of the wells are dropped and the positrons accelerate out, and c) the wells are restored to catch the positrons in the precision trap.

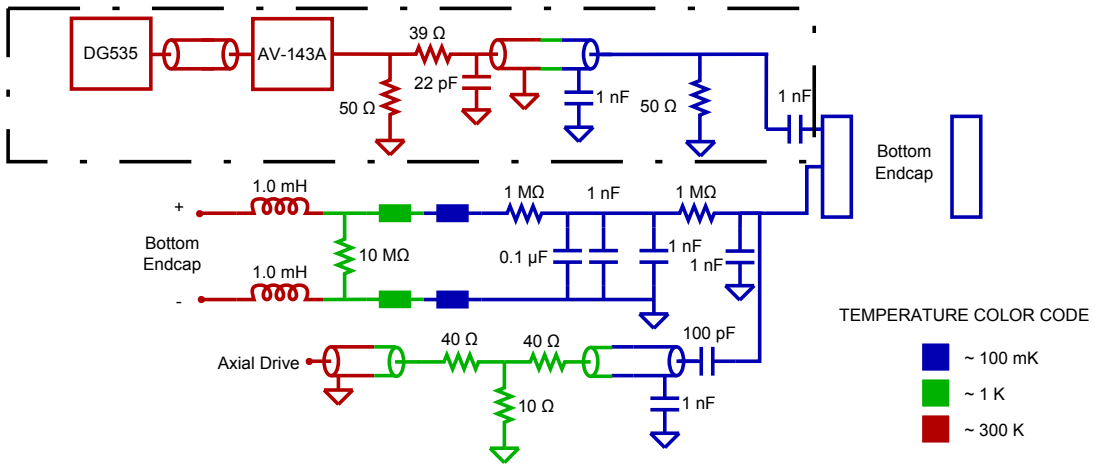

Figure 8.3: The transfer electronics plus the DC biasing and RF drive lines on the loading trap bottom endcap (components highlighted in dashed lines have been added for fast pulsing). The same pulsing electronics have also been added to the top endcap on the precision trap.

proves the impedance matching of the pulsing line, as does the 50 Ω resistor at the pinbase. Due to division with the resistive losses in the microcoax line, the voltage reaching the pin is ≈20% of the voltage going in at the hat. The 2 volts reaching the pin is enough for the transfer scheme in figure 8.2, and the positrons can easily be held in a 2 volt well with minimal losses. The 14 dB of attenuation going down the line should also help to reduce the noise going into the amplifier. Since there is no additional filtering along this line, we carefully shield the connector at the hat when not in use to reduce noise picked up from room temperature.

The transfer scheme should work just as well for electrons, as long as all of the voltages are inverted. Transferring electrons may be a good first step in testing the transfer mechanism, as we know very precisely what the axial frequency of the electrons is in the precision trap, and there may be a slight shift in loading positrons.

For example, in order to center positrons on the detection amplifier noise resonance in the loading trap, the ring voltage must be shifted nearly 150 mV (out of 7.5 V) relative to the voltage for centering the electrons.

It may be possible to load a single positron into the loading trap and then transfer it to the precision trap. However, if there are variations in loading and transfer efficiency, it may be more convenient to load and transfer a small cloud of electrons instead. In that case, we will need a method of going from a small cloud of positrons down to one for a g-factor measurement. There are several possible methods. We can lower the axial well depth to "spill out" some of the particles. In another procedure, positrons could be driven out the of well by applying a strong magnetron cooling drive [9] or a strong axial drive [7]. Either of these are possible candidates.

8.4 Summary

We have built up a new, high stability apparatus in which we have performed quantum jump spectroscopy on a single electron. Preliminary measurements confirm good magnet stability, a smaller magnetic bottle, a narrower cyclotron lineshape (with the detection amplifiers on), and a long cyclotron lifetime consistent with a newly designed trap cavity. We have demonstrated positron loading into the apparatus, and with the newly installed pulsing electronics, the apparatus is poised for an improved electron/positron g-factor comparison.

Bibliography

[1] J. DiSciacca and G. Gabrielse, Phys. Rev. Lett. **108**, 153001 (2012).

[2] D. Hanneke, S. Fogwell, and G. Gabrielse, Physical Review Letters **100**, 120801 (2008).

[3] Arthur Rich and John C. Wesley, Rev. Mod. Phys. **44**, 250 (1972).

[4] P Kusch and HM Foley, Physical Review **72**, 1256 (1947).

[5] W. H. Louisell, R. W. Pidd, and H. R. Crane, Phys. Rev. **94**, 7 (1954).

[6] A. A. Schupp, R. W. Pidd, and H. R. Crane, Phys. Rev. **121**, 1 (1961).

[7] D. Wineland, P. Ekstrom, and H. Dehmelt, Phys. Rev. Lett. **31**, (1973).

[8] RS Vand dyck, PB Schwinberg, and HG Dehmelt, Bulletin of the American Physical Society **24**, 758 (1979).

[9] P. B. Schwinberg, R. S. Van Dyck, and H. G. Dehmelt, Phys. Rev. Lett. **47**, 1679 (1981).

[10] R. S. Van Dyck, Jr., P. B. Schwinberg, and H. G. Dehmelt, Phys. Rev. Lett. **59**, 26 (1987).

[11] L. S. Brown and G. Gabrielse, Rev. Mod. Phys. **58**, 233 (1986).

[12] B. Odom, D. Hanneke, B. D'Urso, and G. Gabrielse, Phys. Rev. Lett. **97**, 030801 (2006).

[13] D. Hanneke, S. Fogwell Hoogerheide, and G. Gabrielse, Phys. Rev. A **83**, 052122 (2011).

[14] Theodor W. Hänsch, Rev. Mod. Phys. **78**, 1297 (2006).

[15] J. DiSciacca, M. Marshall, K. Marable, G. Gabrielse, S. Ettenauer, E. Tardiff, R. Kalra, D. W. Fitzakerley, M. C. George, E. A. Hessels, C. H. Storry, M. Weel, D. Grzonka, W. Oelert, and T. Sefzick, Phys. Rev. Lett. **110**, 130801 (2013).

[16] Julian Schwinger, Phys. Rev. **73**, 416 (1948).

[17] A. Petermann, Helv. Phys. Acta **30**, 407 (1957).

[18] Charles M. Sommerfield, Phys. Rev. **107**, 328 (1957).

[19] Charles M. Sommerfield, Ann. Phys. **5**, 26 (1958).

[20] Tatsumi Aoyama, Masashi Hayakawa, Toichiro Kinoshita, and Makiko Nio, Phys. Rev. Lett. **109**, 111807 (2012).

[21] S. Laporta and E. Remiddi, Phys. Lett. B **379**, 283 (1996).

[22] Tatsumi Aoyama, Masashi Hayakawa, Toichiro Kinoshita, and Makiko Nio, Progress of Theoretical and Experimental Physics **01A**, 107 (2012).

[23] T. Aoyama, M. Hayakawa, T. Kinoshita, and M. Nio, Nuclear Physics B **740**, 138 (2006).

[24] T. Aoyama, M. Hayakawa, T. Kinoshita, and M. Nio, Nuclear Physics B **796**, 184 (2008).

[25] G. Gabrielse, S. Fogwell Hoogerheide, J. C. Dorr, and E. Novitski, in *Precision Spectroscopy in Ion Traps for Fundamental Physics* (Springer, New York, In Preparation), Chap. Testing the Standard Model with Matter and Antimatter.

[26] Andrzej Czarnecki, Bernd Krause, and William J. Marciano, Phys. Rev. Lett. **76**, 3267 (1996).

[27] Peter J. Mohr, Barry N. Taylor, and David B. Newell, Rev. Mod. Phys. **84**, 1527 (2012).

[28] D. L. Farnham, R. S. VanDyck, and P. B. Schwinberg, Phys. Rev. Lett. **75**, 3598 (1995).

[29] G. Werth, J. Alonso, T. Beier, K. Blaum, S. Djekic, H. HÃďffner, N. Hermanspahn, W. Quint, S. Stahl, J. VerdÃž, T. Valenzuela, and M. Vogel, International Journal of Mass Spectrometry **251**, 152 (2006).

[30] Brianna J. Mount, Matthew Redshaw, and Edmund G. Myers, Phys. Rev. A **82**, 042513 (2010).

[31] Andreas Wicht, Joel M. Hensley, Edina Sarajlic, and Steven Chu, Phys. Scr. **102**, 82 (2002).

[32] Rym Bouchendira, Pierre Cladé, Saïda Guellati-Khélifa, François Nez, and François Biraben, Phys. Rev. Lett. **106**, 080801 (2011).

[33] Stanley J. Brodsky and Sidney D. Drell, Phys. Rev. D **22**, 2236 (1980).

[34] D. Bourilkov, Phys. Rev. D **64**, 071701 (2001).

[35] C. S. Wu, E. Ambler, R. W. Hayward, D. D. Hoppes, and R. P. Hudson, Phys. Rev. **105**, 1413 (1957).

[36] J. H. Christenson, J. W. Cronin, V. L. Fitch, and R. Turlay, Phys. Rev. Lett. **13**, 138 (1964).

[37] B. Aubert *et al.*, Phys. Rev. Lett. **93**, 131801 (2004).

[38] R. Aaij *et al.*, Phys. Rev. Lett. **108**, 111602 (2012).

[39] R. Aaij *et al.*, Phys. Rev. Lett. **108**, 201601 (2012).

[40] G. Lüders, Ann. Phys. **2**, 1 (1957).

[41] J. Beringer *et al.*, Phys. Rev. D **86**, 010001 (2012), Particle Data Group.

[42] L. K. Gibbons, A. R. Barker, R. A. Briere, G. Makoff, V. Papadimitriou, J. R. Patterson, B. Schwingenheuer, S. V. Somalwar, Y. W. Wah, B. Winstein, R. Winston, M. Woods, H. Yamamoto, G. J. Bock, R. Coleman, J. Enagonio, Y. B. Hsiung, E. J. Ramberg, K. Stanfield, R. Tschirhart, T. Yamanaka, E. C. Swallow, G. D. Gollin, M. Karlsson, J. K. Okamitsu, P. Debu, B. Peyaud, R. Turlay, and B. Vallage, Phys. Rev. D **55**, 6625 (1997).

[43] E. Abouzaid, M. Arenton, A. R. Barker, M. Barrio, L. Bellantoni, E. Blucher, G. J. Bock, C. Bown, E. Cheu, R. Coleman, M. D. Corcoran, B. Cox, A. R. Erwin, C. O. Escobar, A. Glazov, A. Golossanov, R. A. Gomes, P. Gouffon, J. Graham, J. Hamm, Y. B. Hsiung, D. A. Jensen, R. Kessler, K. Kotera, J. LaDue, A. Ledovskoy, P. L. McBride, E. Monnier, H. Nguyen, R. Niclasen, D. G. Phillips, II, V. Prasad, X. R. Qi, E. J. Ramberg, R. E. Ray, M. Ronquest, A. Roodman, E. Santos, P. Shanahan, P. S. Shawhan, W. Slater, D. Smith, N. Solomey, E. C. Swallow, S. A. Taegar, P. A. Toale, R. Tschirhart, Y. W. Wah, J. Wang, H. B. White, J. Whitmore, M. J. Wilking, B. Winstein, R. Winston, E. T. Worcester, T. Yamanaka, E. D. Zimmerman, and R. F. Zukanovich, Physical Review D **83**, (2011).

[44] D. Colladay and V. Alan Kostelecký, Phys. Rev. D **58**, 116002 (1998).

[45] V. Alan Kostelecký and Neil Russell, Rev. Mod. Phys. **83**, 11 (2011).

[46] Robert Bluhm, V. Alan Kostelecký, and Neil Russell, Phys. Rev. Lett. **79**, 1432 (1997).

[47] Robert Bluhm, V. Alan Kostelecký, and Neil Russell, Phys. Rev. D **57**, 3932 (1998).

[48] H. Dehmelt, R. Mittleman, R. S. Van Dyck, Jr., and P. Schwinberg, Phys. Rev. Lett. **83**, 4694 (1999).

[49] F. M. Penning, Physica (Utrecht) **3**, 873 (1936).

[50] W. Paul, H. Steinwedel, and Test, Zeitschrift für Naturforschung A **8**, 448 (1953).

[51] G. Gabrielse, Phys. Rev. A **27**, 2277 (1983).

[52] G. Gabrielse and H. Dehmelt, Phys. Rev. Lett. **55**, 67 (1985).

[53] G. Gabrielse and F. Colin MacKintosh, Intl. J. Mass Spec. Ion Proc. **57**, 1 (1984).

[54] G. Gabrielse, L. Haarsma, and S. L. Rolston, Intl. J. Mass Spec. Ion Proc. **88**, 319 (1989), ibid. 93, 121 (1989).

[55] J. Goldman and G. Gabrielse, Phys. Rev. A **81**, 052335 (2010).

[56] J. N. Tan and G. Gabrielse, Appl. Phys. Lett. **55**, 2144 (1989).

[57] G. Gabrielse and F. C. Mackintosh, Int. J. Mass Spectrom. **57**, 1 (1984).

[58] S. Fogwell Hoogerheide, Ph.D. thesis, Harvard Univ., 2013.

[59] L. S. Brown and G. Gabrielse, Phys. Rev. A **25**, 2423 (1982).

[60] D. J. Wineland and Wayne M. Itano, Phys. Rev. A **20**, 1521 (1979).

[61] G. Gabrielse and J. N. Tan, J. Appl. Phys. **63**, 5143 (1988).

[62] G. Gabrielse, X. Fei, L. A. Orozco, R. L. Tjoelker, J. Haas, H. Kalinowsky, T. A. Trainor, and W. Kells, Phys. Rev. Lett. **65**, 1317 (1990).

[63] William J. Nuttall, Richard H. Clarke, and Bartek A. Glowacki, Nature **485**, 573 (2012).

[64] T.D. Kelly and G.R. Matos, Historical statistics for mineral and material commodities in the United States (2013 version): U.S. Geological Survey Data Series 140, accessed August 8, 2013, 2013.

[65] E. Novitski, private communication.

[66] JR. L.W. Rupp, The Review of Scientific Instruments **37**, 1039 (1966).

[67] D.A. Hill and C. Hwang, Journal of Scientific Instruments **43**, 581 (1966).

[68] R.J. Higgins and Yung Kwang Chang, The Review of Scientific Instruments **39**, 522 (1968).

[69] R. Prigl, U. Haeberlen, K. Jungmann, G. zu Putlitz, and P. von Walter, Nuclear Instruments and Methods in Physics Research A **374**, 118 (1996).

[70] E. L. Hahn, Phys. Rev. **80**, 580 (1950).

[71] Robert L. Tjoelker, Ph.D. thesis, Harvard University, 1990.

[72] N. Bloembergen, E. M. Purcell, and R. V. Pound, Phys. Rev. **73**, 679 (1948).

[73] Daniel V. Schroeder, *An Introduction to Thermal Physics* (Addison Wesley Longman, New York, 2000).

[74] J.L. Flowers, B.W. Petley, and M.G. Richards, Metrologia **30**, 75 (1993).

[75] Seppo O. Sari and Thomas R. Carver, The Review of Scientific Instruments **41**, 1324 (1970).

[76] Adrian Cho, Science **326**, 778 (2009).

[77] K. Luszczynski, R. E. Norberg, and J. E. Opfer, Phys. Rev. **128**, 186 (1962).

[78] R. Chapman and M. G. Richards, Phys. Rev. Lett. **33**, 18 (1974).

[79] N. R. Newbury, A. S. Barton, G. D. Cates, W. Happer, and H. Middleton, Phys. Rev. A **48**, 4411 (1993).

[80] G. Chiarotti and L. Giulotto, Phys. Rev. **93**, 1241 (1954).

[81] B. D'Urso, Ph.D. thesis, Harvard Univ., 2003.

[82] J. Estrada, T. Roach, J. N. Tan, P. Yesley, and G. Gabrielse, Phys. Rev. Lett. **84**, 859 (2000).

[83] P. B. Schwinberg, R. S. Van Dyck Jr., and H. G. Dehmelt, Phys. Lett. A **81**, 119 (1981).

[84] N. Bowden, Ph.D. thesis, Harvard University, 2003.

[85] J. Estrada, Ph.D. thesis, Harvard University, 2002.

[86] R. S. Van Dyck Jr. , P. B. Schwinberg, and H. G. Dehmelt, in *The Electron*, edited by D. Hestenes and A. Weingartshofer (Kluwer Academic Publishers, Netherlands, 1991), pp. 239–293.

[87] Edward M. Purcell, *Electricity and Magnetism Second Edition* (McGraw-Hill, Boston, 1985).

[88] D. J. Wineland and H. G. Dehmelt, J. Appl. Phys. **46**, 919 (1975).

[89] D. S. Hall, Ph.D. thesis, Harvard University, 1997.

[90] B. D'Urso, R. Van Handel, B. Odom, D., and G. Gabrielse, Phys. Rev. Lett. **94**, (2005).

[91] B. R. Johnson, M. D. Reed, A. A. Houck, D. I. Schuster, Lev S. Bishop, E. Ginossar, J. M. Gambetta, L. DiCarlo, L. Frunzio, S. M. Girvin, and R. J. Schoelkopf, Nature **431**, 162 (2004).

[92] A. Wallraff, D. I. Schuster, A. Blais, R.-S. Huang1 L. Frunzio and, J. Majer, S. Kumar, S. M. Girvin, and R. J. Schoelkopf, Nature Physics **6**, 663 (2010).

[93] L. Brown, Ann. Phys. **159**, 62 (1985).

[94] L. S. Brown, G. Gabrielse, K. Helmerson, and J. N. Tan, Phys. Rev. A **32**, 3204 (1985).

[95] L. S. Brown, G. Gabrielse, K. Helmerson, and J. N. Tan, Phys. Rev. Lett. **55**, 44 (1985).

[96] Jack W. Ekin, *Experimental Techniques for Low-Temperature Measurements* (Oxford University Press, New York, 2006).

[97] J. D. Jackson, *Classical Electrodynamics, 3rd Edition* (John Wiley and Sons, Inc., New York, 1975).

[98] G. Gabrielse and H. G. Dehmelt, Phys. Rev. Lett. **55**, 67 (1985).

[99] J. N. Tan and G. Gabrielse, Phys. Rev. Lett. **67**, 3090 (1991).

[100] J. N. Tan and G. Gabrielse, Phys. Rev. A **48**, 3105 (1993).

[101] D. Hanneke, Ph.D. thesis, Harvard University, 2007.

[102] Brian Carl Odom, Ph.D. thesis, Harvard University, 2004.

[103] B. D'Urso, B. Odom, and G. Gabrielse, Phys. Rev. Lett. **90**, 043001 (2003).

[104] G. GrÃďff, E. Klempt, and G. Werth, Zeitschrift fÃijr Physik **222**, 201 (1969).

[105] D. S. Hall and G. Gabrielse, Phys. Rev. Lett. **77**, 1962 (1996).

[106] G. Gabrielse, J. Estrada, J. N. Tan, P. Yesley, N. S. Bowden, P. Oxley, T. Roach, C. H. Storry, M. Wessels, J. Tan, D. Grzonka, W. Oelert, G. Schepers, T. Sefzick, W. Breunlich, M. Cargnelli, H. Fuhrmann, R. King, R. Ursin, J. Zmeskal, H. Kalinowsky, C. Wesdorp, J. Walz, K. S. E. Eikema, and T. Haensch, Phys. Lett. B **507**, 1 (2001).

[107] N. Guise, Ph.D. thesis, Harvard University, 2010.

[108] G. Gabrielse, N. S. Bowden, P. Oxley, A. Speck, C. H. Storry, J. N. Tan, M. Wessels, D. Grzonka, W. Oelert, G. Schepers, T. Sefzick, J. Walz, H. Pittner, T. W. Hänsch, and E. A. Hessels, Phys. Rev. Lett. **89**, 213401 (2002).

[109] P. Oxley, Ph.D. thesis, Harvard University, 2003.